Compressive Sensing and Its Applications in Automotive Radar Systems

Dissertation
der Mathematisch-Naturwissenschaftlichen Fakultät
der Eberhard Karls Universität Tübingen
zur Erlangung des Grades eines
Doktors der Naturwissenschaften
(Dr. rer. nat.)

vorgelegt von
Zora Slavik, M. Eng.
aus Bömisch Brod, Tschechische Republik

Tübingen
2019

Gedruckt mit Genehmigung der Mathematisch-Naturwissenschaftlichen Fakultät der Eberhard Karls Universität Tübingen.

Tag der mündlichen Qualifikation:	18.08.2020
Dekan:	Prof. Dr. Wolfgang Rosenstiel
1. Berichterstatter:	Prof. Dr. Oliver Bringmann
2. Berichterstatter:	Prof. Dr.-Ing. Thomas Greiner

Abstract

Developments towards autonomous driving promise to lead to safer traffic, where fatal accidents can be avoided after making human drivers obsolete and hence removing the factor of human error. However, to ensure the acceptance of automated driving and make it a reality one day, still a huge amount of challenges need to be solved. With having no human supervisors, automated vehicles have to rely on capable and robust sensor systems to ensure adequate reactions in critical situations, even during adverse conditions. Therefore, the development of sensor systems is required that can be applied for functionalities beyond current advanced driver assistance systems. New requirements need to be met in order to realize safe and reliable automated vehicles that do not harm passersby.

Radar systems belong to the key components among the variety of sensor systems. Other than visual sensors, radar is less vulnerable towards adverse weather and environment conditions. In addition, radar provides complementary environment information such as target distance, angular position or relative velocity, too. The thesis ad hand covers basically two main aspects of research and development in the field of automotive radar systems. One aspect is to increase efficiency and robustness in signal acquisition and processing for radar perception. The other aspect is to accelerate validation and verification of automated cyber-physical systems that feature more complexity along with the level of automation.

After analyzing a variety of possible Compressive Sensing methods for automotive radar systems, a noise modulated pulsed radar system is suggested in the thesis at hand, which outperforms commercial automotive radar systems in its robustness towards noise. Compared to other pulsed radar systems, their drawbacks regarding signal acquisition effort and computation run time are resolved by using noise modulation for implementing a Compressive Sensing signal acquisition and reconstruction method. Using Compressive Sensing, the effort in signal acquisition was reduced by 70 %, while obtaining a radar perception robustness even for signal-to-noise-ratio levels close to or below zero. With a validated radar sensor model the noise radar was emulated and compared to a commercial automotive radar system. Data-driven weather models were developed and applied during simulation to evaluate radar performance in adverse conditions. While water sprinkles increase radome attenuation by 10 dB and splash water even by 20 dB, the actual limitation comes from noise figure and sensitivity of the receiver. The additional signal attenuation that can be handled by the proposed compressive sensing noise radar system proved to be even

up to 60 dB, which ensures a high robustness of the receiver during adverse weather and environment conditions.

Besides robustness, interference is also considered. On the one hand the increased robustness towards interference of the noise radar system is demonstrated. On the other hand, the impact on existing automotive radar systems is evaluated and strategies to mitigate the impact are presented.

The structure of the thesis is the following. After introducing basic principles and methods for automotive radar systems, the theory and metrics of Compressive Sensing is presented. Furthermore some particular aspects are highlighted such as environmental conditions, different radar architectures and interference. The state of the art provides an overview on Compressive Sensing approaches and implementations with focus on radar. In addition, it covers automotive radar and noise radar related aspects. The main part starts with presenting different approaches on making use of Compressive Sensing for automotive radar systems, that are capable of either improving or extending radar signal acquisition and perception. Afterwards the focus is put on a noise radar system that uses Compressive Sensing for an efficient signal acquisition and reconstruction. It was analyzed using different Compressive Sensing metrics and evaluated in a proof-of-concept simulation. With an emulation of the noise radar system the feasibility of the Compressive Sensing signal acquisition and processing was demonstrated in a more realistic scenario. The development and validation of the underlying sensor model is documented as well as the development of the data-driven weather models. After considering interference and co-existence with commercial radar systems, a final chapter with conclusions and an outlook completes the work.

Kurzfassung

Die Entwicklung in Richtung zu autonomem Fahren verspricht, künftig einen sicheren Verkehr ohne tödliche Unfälle zu ermöglichen, indem menschliche Fahrer vollständig ersetzt werden. Dadurch entfällt der Faktor des menschlichen Fehlers, der aus Müdigkeit, Unachtsamkeit oder Alkoholeinfluss resultiert. Um jedoch eine breite Akzeptanz für autonome Fahrzeuge zu erreichen und es somit eines Tages vollständig umzusetzen, sind noch eine Vielzahl von Herausforderungen zu lösen. Da in einem autonomen Fahrzeug kein menschlicher Fahrer mehr in Notfällen eingreifen kann, müssen sich autonome Fahrzeuge auf leistungsfähige und robuste Sensorsysteme verlassen können, um in kritischen Situationen auch unter widrigen Bedingungen angemessen reagieren zu können. Daher ist die Entwicklung von Sensorsystemen erforderlich, die für Funktionalitäten jenseits der aktuellen advanced driver assistance systems eingesetzt werden können. Dies resultiert in neuen Anforderungen, die erfüllt werden müssen, um sichere und zuverlässige autonome Fahrzeuge zu realisieren, die weder Fahrzeuginsassen noch Passanten gefährden. Radarsysteme gehören zu den Schlüsselkomponenten unter der Vielzahl der verfügbaren Sensorsysteme, da sie im Gegensatz zu visuellen Sensoren von widrigen Wetter- und Umgebungsbedingungen kaum beeinträchtigt werden. Darüber hinaus liefern Radarsysteme zusätzliche Umgebungsinformationen wie Abstand, Winkel und relative Geschwindigkeit zwischen Sensor und reflektierenden Zielen. Die vorliegende Dissertation deckt im Wesentlichen zwei Hauptaspekte der Forschung und Entwicklung auf dem Gebiet der Radarsysteme im Automobilbereich ab. Ein Aspekt ist die Steigerung der Effizienz und Robustheit der Signalerfassung und -verarbeitung für die Radarperzeption. Der andere Aspekt ist die Beschleunigung der Validierung und Verifizierung von automated cyber-physical systems, die parallel zum Automatisierungsgrad auch eine höhere Komplexität aufweisen.

Nach der Analyse zahlreicher möglicher Compressive Sensing Methoden, die im Bereich Fahrzeugradarsysteme angewendet werden können, wird ein rauschmoduliertes gepulstes Radarsystem vorgestellt, das kommerzielle Fahrzeugradarsysteme in seiner Robustheit gegenüber Rauschen übertrifft. Die Nachteile anderer gepulster Radarsysteme hinsichtlich des Signalerfassungsaufwands und der Laufzeit werden durch die Verwendung eines Compressive Sensing-Signalerfassungs- und Rekonstruktionsverfahrens in Kombination mit einer Rauschmodulation deutlich verringert. Mit Compressive Sensing konnte der Aufwand für die Signalerfassung um 70 % reduziert werden, während gleichzeitig die Robustheit der Radarwahrnehmung auch für signal-to-noise-ratio-Pegel nahe oder unter Null erreicht wird. Mit einem validierten Radarsensormodell wurde das Rauschradarsystem emuliert und mit einem kommerziellen Fahrzeugradarsystem verglichen. Datengetriebene Wettermodelle wurden entwickelt und während der Simulation angewendet, um die Radarleistung unter widrigen Bedingungen zu bewerten. Während eine Besprühung mit Wasser die Radomdämpfung um 10 dB erhöht und Spritzwasser sogar um 20 dB, ergibt sich die eigentliche Begrenzung aus der Rauschzahl und Empfindlichkeit des Empfängers. Es konnte bewiesen werden, dass das vorgeschlagene Compressive Sensing Rauschradarsystem mit einer zusätzlichen Signaldämpfung von bis zu 60 dB umgehen kann und damit eine hohe Robustheit in ungünstigen Umwelt- und Wetterbedingungen aufweist.

Neben der Robustheit wird auch die Interferenz berücksichtigt. Zum einen wird die erhöhte Störfestigkeit des Störradarsystems nachgewiesen. Auf der anderen Seite werden die Auswirkungen auf bestehende Fahrzeugradarsysteme bewertet und Strategien zur Minderung der Auswirkungen vorgestellt.

Die Struktur der Arbeit ist folgende. Nach der Einführung der Grundlagen und Methoden für Fahrzeugradarsysteme werden die Theorie und Metriken hinter Compressive Sensing gezeigt. Darüber hinaus werden weitere Aspekte wie Umgebungsbedingungen, unterschiedliche Radararchitekturen und Interferenz erläutert. Der Stand der Technik gibt einen Überblick über Compressive Sensing-Ansätze und Implementierungen mit einem Fokus auf Radar. Darüber hinaus werden Aspekte von Fahrzeug- und Rauschradarsystemen behandelt. Der Hauptteil beginnt mit der Vorstellung verschiedener Ansätze zur Nutzung von Compressive Sensing für Fahrzeugradarsysteme, die in der Lage sind, die Erfassung und Wahrnehmung von Radarsignalen zu verbessern oder zu erweitern. Anschließend wird der Fokus auf ein Rauschradarsystem gelegt, das mit Compressive Sensing eine effiziente Signalerfassung und -rekonstruktion ermöglicht. Es wurde mit verschiedenen Compressive Sensing-Metriken analysiert und in einer Proof-of-Concept-Simulation bewertet. Mit einer Emulation des Rauschradarsystems wurde das Potential der Compressive Sensing Signalerfassung und -verarbeitung in einem realistischeren Szenario demonstriert. Die Entwicklung und Validierung des zugrunde liegenden Sensormodells wird ebenso dokumentiert wie die Entwicklung der datengetriebenen Wettermodelle. Nach der Betrachtung von Interferenz und der Koexistenz des Rauschradars mit kommerziellen Radarsystemen schließt ein letztes Kapitel mit Schlussfolgerungen und einem Ausblick die Arbeit ab.

In memory of Prof. Dr. Wolfgang Rosenstiel.

Acknowledgements

First of all, I would like to thank Prof. Oliver Bringmann, Prof. Thomas Greiner and Prof. Wolfgang Rosenstiel for giving me the opportunity to participate in the cooperative doctoral study course *Entwurf und Architektur Eingebetteter Systeme (EAES)* and for their guidance. Especially, I would like to thank Prof. Oliver Bringmann for his advice, comments and time, whenever some of it was necessary. I am thankful to Dr. Sebastian Reiter not only for his practical support, but also for his interest in my research field and for being a curious and supporting sparring partner. And I would like to thank Dr. Kumar Vijay Mishra for many fruitful discussions on Compressive Sensing, radar, weather and philosophy. To Prof. Manfred Strohrmann and Prof. Franz Quint I am thankful for encouraging me to find and follow my path in academia. Also, I am grateful to Prof. Marc Ihle for making me aware of the research field of Compressive Sensing and encouraging me to start a PhD in the first place. Without the other PhD candidates from EAES and the University of Tübingen and without the members of DocNet, it would have been a much less interesting and enjoyable time. I am thankful that I had the chance to go some of the way with all of you. For interesting discussions about radar and simulation topics, I would like to thank Martin Holder and everybody else, who was working within the ENABLE-S3 project. To Andreas Haderer, the great developer of the INRAS Radarbook, I would like to express my thanks for his support and for bringing such a useful development platform to the market. Without Tobias Knipping I would not have been able to get my hands on my corner reflectors in such a short time. Thank you for that. In addition, I would like to thank Dominic Huber for practical help with my measurements. I also would like to express my thanks to the team assistances, especially Larissa Lampl and Sonja Göttl. I would like to thank Susanne Slavik and Marion Morath for all the laughs and tears we shared during the past years. Thank you for the non-technical and philosophical topics, we could discuss. In addition, I would like to thank Dr. Saadia Knipping and Dr. Marion Rütten for motivating, coaching and trusting in me. Finally, I would really like to thank all the people, who did not forget about me, while I was writing.

Contents

1 Introduction **1**
- 1.1 Motivation . . . 1
- 1.2 Objectives . . . 3
- 1.3 Outline . . . 6

2 Basics and Background **9**
- 2.1 Radar and Automotive Radar . . . 9
  - 2.1.1 Automotive radar scenario . . . 11
  - 2.1.2 Basic radar architectures . . . 15
- 2.2 Compressive Sensing . . . 20
  - 2.2.1 Signal acquistion using compressive sensing . . . 22
  - 2.2.2 Signal reconstruction . . . 24
- 2.3 Weather Conditions in Automotive Context . . . 26
  - 2.3.1 Definitions and Recommendations on Weather Conditions . . 27
  - 2.3.2 Adverse environment conditions in automotive scenarios . . . 28

3 State of the Art **33**
- 3.1 Applications of Compressive Sensing . . . 33
- 3.2 Radar . . . 36
  - 3.2.1 Pulsed Radar . . . 37
  - 3.2.2 Noise Radar . . . 38
  - 3.2.3 Compressive Sensing in Noise Radar Systems . . . 41
- 3.3 Automotive Radar . . . 43
  - 3.3.1 Automotive Noise Radar Application . . . 44
  - 3.3.2 Multi-range Radar . . . 45
  - 3.3.3 Interference in automotive radar . . . 47
  - 3.3.4 Summary and research interest . . . 49

4 Compressive Sensing based Noise Radar **51**
- 4.1 Compressive Sensing for Automotive Radar . . . 54
  - 4.1.1 Pulsed Radar - RMPI and SAR . . . 55
  - 4.1.2 Phased Array . . . 60

4.2 CS Noise Radar 69
  4.2.1 Signal Model 72
  4.2.2 Signal acquisition and reconstruction 75
  4.2.3 Compressive Sensing Analysis 79
4.3 Proof-of-Concept 83
  4.3.1 Simulation Model 84
  4.3.2 Simulation Results 86
  4.3.3 Evaluation and Discussion 91

5 Demonstrator and Experimental Results 95
5.1 LFMCW Radar 96
  5.1.1 Radarbook Parametrization 97
  5.1.2 Measurement of weather effects 101
  5.1.3 Radar sensor model 108
5.2 Noise Radar 115
  5.2.1 Emulation with radar sensor model 116
  5.2.2 Performance testing and impact of weather effects 116
  5.2.3 Interference in automotive radar 119

6 Conclusion and Outlook 123

Abbreviations 127

References 133

MIMO-77GHz RF-Frontend 148

Background to related methods 161
1 Mathematics 161
  1.1 Fourier Transformation 161
  1.2 Information and signal theory 161
2 CS Algorithms 162
  2.1 OMP 162
  2.2 CAMP 163
  2.3 ROMP 165
  2.4 BPDN 167
3 AgSim Co-Simulation 168

1 Introduction

Autonomous driving has been a vision for a long time, but only recently research and industry are close to making this vision a reality. Apart from the promised increased comfort of autonomous driving, it is believed that removing the human driver and therefore human error from the steering wheel will significantly decrease severe and fatal traffic accidents. Contrary to human drivers, autonomous vehicles are not prone to various distractions, fatigue and intoxication or emotional reactions that can result in speeding or hazardous maneuvers, for example. In combination with vehicle-to-x communication, autonomous driving will even help to optimize traffic flows and therefore disburden cities from traffic jams, noise and emissions.

Besides several ethical questions, a critical item is the perception of the environment and recognition of other traffic participants, an aspect that is also critical for recent advanced driver assistance systems. Perception strategies need to be adjusted to the new levels of criticality including different sensor types, sensor data interpretation but also acquisition methods. Dealing with signal distortions and interferences with an increased amount of sensor systems and sensor types along with an increased criticality of sensor data interpretation opens a new wide area of research and development perspectives and objectives.

1.1 Motivation

The developments towards automated driving poses numerous challenges to the development of sensor systems that are crucial to navigate the vehicles to their destination and ensure safety for both, passengers and passersby. Apart from visual sensors that are intuitive to human perception, other sensors such as ultrasonic or radar are necessary that are on the one hand providing additional information or act on the other hand as complementary sensor systems in conditions with reduced visibility. There are two driving motivations for research and development in automotive radar that will be addressed.

One aspect in the overall motivation is to find more efficient but also robust methods for radar sensor signal acquisition and processing. Currently, radar systems and other actively transmitting sensors are still rather restricted to the upscale automotive market and therefore the amount of radar equipped vehicles on the street is still manageable. But as different advanced driver assistance systems and therefore also radar sensors are becoming more common for the overall automotive market, challenges such as interference within the sensors are becoming urgent issues that need to be solved by interference-proof and robust sensor systems.

That includes not only the receiver side but also the transmitter side as modifying the waveforms is required for some more robust radar sensor system architectures that rely on completely different concepts than recent common automotive radar systems. On the one hand, implementing experimental radar architectures on silicon blows up the costs for developing according advanced driver assistance systems.

On the other hand, there are challenges regarding the validation and verification of ready-to-drive passenger vehicles that come along with the huge amount of sensor systems. The required testing effort to not only prove the reliable and robust functionality of new radar and sensor concepts in stand-alone operation but also as an integrated part of vehicle and infrastructure perception systems, calls for different testing and qualification approaches. Shifting as much developing and testing effort as possible into the virtual domain is an important part of solving the testing challenges ahead.

Therefore, a virtual representation of sensor systems and their components, depending on the particular testing objectives, supports the objective of experimental, fast, and innovative, but efficient and cost sensitive development and testing. In addition, a virtual test bench for automotive sensors requires realistic environment scenarios that take all critical circumstances into account at the same time. To validate the robustness of radar in adverse weather and environment conditions, representative stimuli generators need to be included within the environment simulation platform that is used for testing.

Radar architectures with an increased robustness towards noise as well as interference can be found in pulse-based concepts, especially while using noise-inspired transmit waveforms. Noise modulation reduces not only the required transmit power level compared to unmodulated pulses but also adds a unique fingerprint to each pulse. If generated in a pseudo-random and reproducible way, methods comprised under the term Compressive Sensing allow an efficient signal acquisition and therefore omit the downsides of correlator-based receiver concepts applied for systems using pulsed transmit waveforms. Compressive Sensing methods are favorable, because they allow a significant reduction of filter banks. Otherwise, the required amount of filter banks in the correlation stage limits both, range and resolution of a sensor system when it comes to practical implementation and realization.

1.2 Objectives

Passenger mobility is in progress of basically being developed from scratch. Vehicles are evolving from relying on mechanical parts and systems towards automated cyber-physical systems that are capable of dealing with complex perception and perception based reaction sequences, which requires more and more computational power. Beyond the capability of processing more sensor systems in parallel, the increase of computational power paves the way for signal processing methods that were not practical before due to hardware and runtime limitations. Exploring and diving into the vast amount of new possibilities in automated driving and its sensing methods in particular was driving the research in the thesis at hand.

Without computational power, the effort of signal processing remains mainly on the hardware side in addition to signal acquisition. In that approach sensor signals are pre-processed or even interpreted by circuitry. After pre-processing, analog signals need to be made available for digital signal processing or high-level interpretation, respectively by sampling. Sampling poses requirements on the hardware, that scale with the maximum frequency, which is included in an analog signal that should be acquired. These requirements are for example rise and fall time of an analog-to-digital-converter, dynamic and sensitivity, resolution and available sampling frequency. Especially the latter has the tendency to result in expensive and challenging hardware designs, as soon as frequency is increased. Hence, the aim is to avoid high frequencies at the sampling interface to mitigate the necessity for expensive hardware designs for digitized signal acquisition. As a result of the availability of high computational power in future highly automated or even autonomous cars, it becomes feasible to shift hardware complexity of signal acquisition to digital signal processing. Hence, signal acquisition methods that are highly efficient and have low effort from hardware perspective, but result in computationally expensive signal processing and reconstruction such as Compressive Sensing methods, become attractive. Therefore, Compressive Sensing methods established an emerging research field during the past ten years for an increasing amount of applications.

The vast amount of possible and successful applications for Compressive Sensing methods can found in image processing, where the matrix structure of digitized pictures is favorable for Compressive Sensing implementations. The reason is, that Compressive Sensing relies on numerical optimization. But there are also successful examples for Compressive Sensing applications that use continues signals such as implementations for airborne and surveillance radar systems or for medical imaging processing such as magnetic resonance imaging. Only in the field of automotive radar research on Compressive Sensing is rare so far. That is not only because the automotive sector is very sensitive towards increasing prices, but also because of the long development and support cycles. Although there are currently many innovations going on, it needs to be considered, that previously developed integrated circuit for sensor circuitry might remain easily for twenty years or even more on the roads. On the one hand, that has the beneficial effect, that chip prices drop significantly, once a technology is established, but on the other hand, that results in a low willingness to adapt new technologies that come along with their own circuitry in the first place. In addition, new technologies may not disturb the old ones. Nevertheless, this thesis shows how Compressive Sensing can lead to a revolution in automotive sensor concepts, which will make it ready to tackle future challenges of autonomous driving. Besides exploring the state-of-the-art under several aspects connected to radar and Compressive Sensing, an overview is mapped out to show the numerous possible approaches on the one side and the resulting decision for the focused Compressive Sensing based solution for automotive radar in the thesis at hand.

Within the thesis at hand, the author analyzed the potentials of Compressive Sensing for automotive radar systems. Driven by practical considerations and requirements such as hardware availability and potential near-future acceptance by original equipment manufacturers, the author focused on a noise modulated pulsed radar using compressive sensing at the receiver stage for efficient signal acquisition. Although there are other promising and meaningful potential applications for compressive sensing in automotive radar as will be shown later on, the proposed noise radar in combination with compressive sensing at the receiver stage comes with the best prerequisites to meet the demands on robustness towards interference and a minimum effort on necessary hardware adaptations at the same time.

Automotive radar systems that are currently on the market, rely on frequency modulated continuous wave principles. Specifically, several linear chirps are applied as transmit waveform, i.e. signals with linearly increasing frequency during a specified chirp duration. The chirps are repeated several times in order to improve velocity resolution. High sampling frequencies at the receiver side are avoided by comparing the receive frequency with the current transmit frequency on hardware, so that only the frequency difference needs to be sampled. Although the frequency modulated continuous wave approach comes with a simple and low-cost hardware, it also comes with the clear downside of being very vulnerable towards interference. As frequency modulated continuous wave radar systems cannot overcome the limitation regarding interference considering the sensor density inherent to autonomous driving, the proposed alternative radar implementation uses a pulsed radar architecture instead.

The proposed noise radar approach is based on a correlation receiver such as used in typical pulsed radar systems. Correlation receivers consist of a filter bank including a filter for each range gate, i.e. possible target range. Without sacrificing range resolution, a significant number of filters would be required for automotive long ranges of 200 m with a low efficiency regarding signal acquisition. While the correlation receiver for a pulsed radar system addresses the problem of developing an interference-proof radar system, enhanced additionally by a noise modulated pulse, Compressive Sensing allows for a significantly more efficient signal acquisition and hence allowing for practical implementation in automotive radar systems. A correlation receiver differs from a frequency modulated continuous wave receiver at the mixer inputs. While the receive signal is mixed with the transmit signal in case of a frequency modulated continuous wave receiver, the correlation receiver applies its correlation filter outputs to the receive signal, which results in a necessary hardware adaptation. For a fair performance comparison between a conventional frequency modulated continuous wave and the proposed compressive sensing noise radar system, both systems need to be operated in the same environment and under same conditions, which means that both systems need to exist in the same domain, either real or virtual.

The background of the latter is that for efficient and meaningful prototyping of experimental new approaches it is beneficial to use virtual testing instead of going directly for chip development. Virtual implementations, if designed with an abstraction level that fits to relevant and critical evaluation goals, offer a smart way to not only test experimental designs but also to accelerate the realization of relevant test cases to the point of making cumbersome hardware implementations obsolete for a simple proof-of-concept. Therefore, a radar sensor model was developed by the author that mimics physical characteristics of the radar development board, according to the most critical point regarding compressive sensing, which is the exact characteristic of the receive signal. The radar sensor model was validated against point-wise real measurements with the radar development board operated in Linear FMCW mode. Virtually, the radar sensor model was applied first as Linear FMCW radar and then as Compressive Sensing noise radar, with and without interference and therefore considering critical and relevant test scenarios.

Another critical aspect are adverse weather conditions that need to be considered in order to obtain valid simulation results and conclusions. Within automotive radar applications, weather conditions introduce new and different challenges than in applications such as airborne systems. The novelty is the aspect that in automotive radar systems spatial effects in the ultimate vicinity of the radar sensor are critical in contrast to applications covering several tenth or hundreds of kilometers. Various weather conditions, especially rain, increase the signal attenuation and therefore lower the signal-to-noise-ratio, which impairs the robustness of a successful radar perception. Therefore, a set of relevant weather conditions and measurement setups was defined and implemented for testing and validation. Real-world measurements were obtained from the automotive Linear FMCW radar, which was used as a blueprint for the radar sensor simulation. The measurements were used as input for data-driven models of a set of weather condition induced effects that were afterwards included during radar simulation.

For future testing purposes, the virtual radar sensor was connected to an environ-

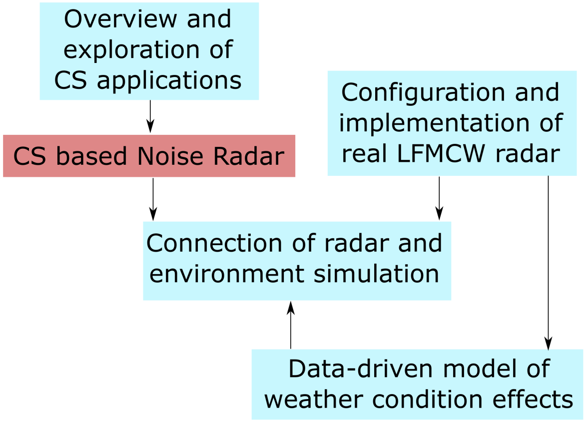

Figure 1.1 – Overview objectives and interdependencies

ment simulation, whereas the weather and environment conditions remain part of the sensor simulation. The environment simulation only defines the environment conditions and does not generate radar stimulation nor manipulates the radar receive signal. The purpose of tethering the radar sensor with the environment simulation is to define and implement the interfaces for future operation.

As an overview, the main objectives of the thesis and their interdependencies are depicted in Figure 1.1, whereas the overall goal is highlighted in red. It becomes evident that several stand-alone objectives come together in this work that illuminate different aspects of research in radar. Namely the aspects are Compressive Sensing and signal acquisition including signal processing, but also virtual and semi-virtual validation and testing in the context of autonomous driving. Besides the original objectives, this work therefore also shows, how complex the implications of autonomous driving are. Of course, several subordinate objectives are realized aiming at the demonstration of the Compressive Sensing based noise radar. This is reflected in the outline of this work.

1.3 Outline

The different objectives stated in the introduction within this first chapter, shape the structure of the thesis. In the second chapter, basic principles are explained and background information is given on the two main topics regarding theory, i.e. automotive radar and Compressive Sensing. The background for automotive radar comprises principles of pulsed and continuous wave radar signal acquisition and processing as well as particular background information on automotive scenarios that are essential to understand challenges and chances in automotive applications including design parametrization. In addition, interference principles are tackled, thus emphasizing the problem statement and point out the motivation for considering this issue. The principles of Compressive Sensing are explained along with metrics that are applicable to evaluate the measurement process as well as the signal reconstruction.

The third chapter contains the state-of-the-art giving an insight to the various covered aspects, either belonging to radar or to Compressive Sensing. It maps out the state-of-the-art on radar technologies on both, commercial and research approaches and not limited to automotive radar, where useful. Radar state-of-the-art additionally involves particular radar problem statements and different solution statements. Besides showing the theoretical state-of-the-art of Compressive Sensing, examples for either hardware implementation concepts and successfully implemented hardware demonstrators are listed. The focus is not limited to but remains on radar technologies in general that make use of Compressive Sensing and especially noise radar systems.

The fourth chapter includes the main part of this work. At the beginning of the chapter, different approaches in employing Compressive Sensing to automotive radar applications are explored followed by the reasoning focus on one application, namely noise radar. The study gives a summary on how to make use of Compressive Sensing for radar systems, especially in the context of automotive radar. Hereby, some highlights are presented with according simulations. The core is a concept of noise radar sensor for automotive applications that uses Compressive Sensing methods for an efficient signal acquisition that is derived from a correlation receiver concept. The methods and principles of the suggested noise radar concept and its implementation design for transmit and receive direction as well as the subsequent signal processing, are explained here. It is shown, how successful reconstructions can be obtained and the previously defined metrics are applied to the selected approach.

This chapter is followed by the a description of the implemented demonstrator. It tackles hardware and software configuration and implementation for a real world demonstrator but also a corresponding emulation for performance analysis. It is presented, how the measurements were performed to generate data-driven weather and environment models. Hence, the chapter does not only include the radar emulation but also adds weather and environment models to the overall radar simulation environment that are obtained according to the presented measurements. The simulation models are evaluated and validated against real world measurements making the derived concepts plausible. Finally, the conclusion and outlook chapter summarizes the findings and results and presents an outlook on follow-up research.

2 Basics and Background

Basics and background information on three major relevant topics are introduced in this chapter, following the objectives from section 1.2. Some background information is required on radar and in particular on radar in automotive applications. Besides regulation in the sensitive field of frequency allocation, basic signal acquisition and processing are explained.

The basic concept and elementary principles of Compressive Sensing (CS) are introduced along with its metrics for evaluation, that are stated and explained here. These metrics will be used later on to explain the CS noise radar methodology but also to show its feasibility. The metrics are important tools in CS architecture development to encourage implementation and testing new designs while having build up already a certain confidence that a method is applicable and therefore worth trying even on expensive wafers, if required.

The last topic on background, i.e. weather and environment conditions, is viewed under the aspect of radar, especially automotive radar. Particular challenges that occur typically in automotive scenarios and impact frequencies at high automotive frequency bands, are stated as well.

2.1 Radar and Automotive Radar

The history of radar, which is an acronym for radar detection and ranging, starts with Heinrich Hertz, when he discovered electromagnetic waves. During World War II, several countries developed independently from each other radar systems to locate ships and aircrafts. Among them was the UK, who spread the word that their soldiers had a superior sight because of an increased consumption of carrots, in order to veil the real reason for their high detection rate of enemy aircrafts.

Basically, the principle of radar is comparable to sonar used by animals such as bats to find their prey. They send out pulses of ultrasonic wave which can be thought of as a modulated pulse trains. After transmission, they listen to the backscatter and analyze the delays, frequency shifts and amplitude levels. Ultrasonic waves used by bats around 41 kHz belong to the sound spectrum. Sound waves are not electromagnetic waves and do not show the wave-particle-duality of electromagnetic radiation (EMR). But radar uses electromagnetic waves at different frequencies within the radio frequency (RF) spectrum according to the target application and the

Table 2.1 – ITU Recommendation ITU-R V.431-8

Name	ITU	Frequency	Metric subdivision
extremely low frequency (ELF)	1	3 - 30 Hz	Decamegametric waves
super low frequency (SLF)	2	30 - 300 Hz	Megametric waves
ultra low frequency (ULF)	3	0.3 - 3 kHz	Hectokilometric waves
very low frequency (VLF)	4	3 - 30 kHz	Myriametric waves
low frequency (LF)	5	30 - 300 kHz	Kilometric waves
medium frequency (MF)	6	0.3 - 3 MHz	Hectometric waves
high frequency (HF)	7	3 - 30 MHz	Decametric waves
very high frequency (VHF)	8	30 - 300 MHz	Metric waves
ultra high frequency (UHF)	9	0.3 - 3 GHz	Decimetric waves
super high frequency (SHF)	10	3 - 30 GHz	Centimetric waves
extremely high frequency (EHF)	11	30 - 300 GHz	Millimetric waves
	12	0.3 - 3 THz	Decimillimetric waves
	13	3 - 30 THz	Centimillimetric waves
	14	30 - 300 THz	Micrometric waves

principle remains the same. Active illumination of the scene with radar signals results in a reflected backscatter that contains information about surrounding radar targets including location and velocity. RF refers to the spectral range from 3 Hz up to 3 THz according to International Telecommunication Union (ITU) Radio Regulations. As an orientation, the spectrum of visible light covers 400 to 789 THz.

The ITU assignment of frequency bands within the RF spectrum as listed in Table 2.1 [67] corresponds to the power of ten of the respective frequency dimension, e.g. 9 for the lower Gigahertz dimension according to 10^9. An ITU defined band with the number N covers $[0.3 \cdot 10^N; 3 \cdot 10^N]$. From radar perspective the subset of microwaves within the RF spectrum, which starts from 300 MHz, is most interesting. In the literature, often a notation using letters is found, which unfortunately is not standardized and therefore not recommended by the ITU.

Nevertheless, the ITU derived from publications a rule of thumb for matching letters to radar frequency bands and the Institute of Electrical and Electronics Engineers (IEEE) Standards Association published the definitions in [35]. The only difference between the ITU recommendation and the IEEE standard lies in the assignment of letters to frequency bands above 40 GHz, which is left void by the ITU, so far. In Table 2.2 the different letter designations are shown, whereas bands above Ka are not defined by ITU. The notation mm for mmWaves can either refer to 110 to 300 GHz or 30 to 300 GHz. Another orientation for using letters is the North Atlantic Treaty Organization (NATO) designation referred to in [25].

Classification of frequency bands and radar frequency bands in particular is a relevant aspect that clarifies in an unambiguous way characteristics and specifications

Table 2.2 – Radar letter designations

IEEE/ITU		NATO (new)		NATO (old)	
L	1 - 2 GHz	D	1 – 2 GHz	S	1.55 – 3.9 GHz
S	2 - 4 GHz	E	2 – 3 GHz		
		F	3 – 4 GHz		
C	4 - 8 GHz	G	4 – 6 GHz	C	3.9 – 6.2 GHz
		H	6 – 8 GHz	X	6.2 – 10.9 GHz
X	8 - 12 GHz	I	8 – 10 GHz		
Ku	12 - 18 GHz	J	10 – 20 GHz	Ku	10.9 – 20 GHz
K	18 - 27 GHz	K	20 – 40 GHz	Ka	20 – 36 GHz
Ka	27 - 40 GHz				
V	40 - 75 GHz	L	40 – 60 GHz	Q	36 – 46 GHz
				V	46 – 56 GHz
W	75 - 110 GHz	M	60 – 100 GHz	W	56 – 100 GHz
G	110 - 300 GHz				

of implemented technologies. Due to frequency specific characteristics and sometimes even more important regulations on frequency allocation, different applications are reasonable for different frequencies. Therefore, it is sensitive in practical situations to refer rather to a radar application than the frequency band. Although some organizations invest a lot of effort into standardizing frequency allocation all over the world, national authorities still have the last word and therefore frequency allocations can differ not only in ultimate frequencies but also duty cycles or transmit power level.

Automotive applications can be implemented in Germany at different center frequencies, whereas the applications are roughly specified. The applications comprise communication for Intelligent Transport Systems (ITS) and detection with short range radar (SRR) in ultra-wide band (UWB) as well as narrow band mode, mid range radar (MRR) and long range radar (LRR). Regulations for ITS and radar applications are listed in Table 2.3 according to [1], [2], [3] and [4]. It should be noted that these frequency allocations are not dedicated to automotive applications only, i.e. the general frequency allocation does not come along with an exclusive right of usage. Therefore, interference from other participating applications should be expected and it is up to the user to implement safety measures for interference.

2.1.1 Automotive radar scenario

In contrast to other common applications [43], e.g. airborne radar systems, automotive radar is allocated at a significantly higher frequency band, whereas the most important frequency allocation lies within 76 GHz to 81 GHz. While the comparable high frequency is beneficiary for realizing a small antenna form factor that is easy to

Table 2.3 – Frequency allocation for automotive applications in Germany. ASPD: average spectral power density; P_p: Peak power

Application	Frequency in [GHz]	max. ASPD in [dBm/MHz] (EIRP)	max. P_p in [dBm] (EIRP)
ITS	5.855 - 5.905 GHz	23	33
SRR	24.05 - 24.25 GHz	20	20
SRR, UWB	21.65 - 22.00 GHz	-61.3	0 per 50 MHz
	22.00 - 26.65 GHz	-41.3	0 per 50 MHz
ITS	63.00 - 64.00 GHz	n/a	40
ITS, radar	76.00 - 77.00 GHz	50	55
ITS, pulsed radar	76.00 - 77.00 GHz	23.5	55
object detection	76.00 - 77.00 GHz	3	30
MRR, LRR	77.00 - 81.00 GHz	-3	55

integrate in vehicles, the region of interest can still be illuminated by the automotive radar. On top, the higher free space attenuation that comes with the higher frequency, naturally limits the range of the radar and therefore tones down the overall interference level. Ranges above approximately 70 m up to 200 m are regarded as long ranges, while range distances between 20 m and 70 m are assumed as mid ranges and the ultimate vicinity of a vehicle below 20 m or even 10 m is defined as short range. Although the manufacturers do not have harmonized range definitions, the numbers classify roughly the terms short, medium and long. In automotive scenarios with several vehicles, the ego-vehicle is the platform of the system under test (SuT). Other traffic participants are classified according to their functionality within a specific scenario, e.g. parking vehicle, crossing pedestrian or other. Consequently, automotive scenarios are very dynamic as the usually moving ego-vehicle passes all the static or dynamic objects. The scenario dynamic is partially limited by speed limits or different sceneries, such as urban or rural areas along with typical occurrences of traffic participants and their behavior. Table 2.4 gives an overview of typical parameters in automotive scenarios, that influence the selection of feasible radar parameters. More insights on genereting automitive scenarios specifically for validation and verification were contributed by the author in [39].

In automotive radar perception configurations, the separate transmit and receive antennas are usually mounted on the same platform making it a co-located radar system. The transmit signal propagates two times through the channel. The channel refers to the signal propagation medium and it is modeled here as a free-space propagation channel with additional white Gaussian noise (AWGN). The received signal power P_r is determined using Frii's transmission equation. In the original classical formulation [84], it is defined with the effective apertures of the transmit and receive antennas, A_t, A_r, the distance in range r and the wavelength $\lambda = \frac{c}{f}$ with

Table 2.4 – Parameter variations in different automotive scenarios

Parameter	Urban	Intersection	Rural	Highway
range	1 … 100 m	0.5 … 50 m	10 … 200 m	10 … 300 m
azimuth	2 … 20 m	0.5 … 5 m	1 … 5 m	1 … 10 m
typ. peak velo.	70 km h^{-1}	40 km h^{-1}	110 km h^{-1}	1 20 … 300 km h^{-1}
typ. min velo.	$\leqslant$10 km h^{-1}	$\leqslant$10 km h^{-1}	10 … 30 km h^{-1}	60 … 80 km h^{-1}
density static obj.	high	medium	medium	low
density dyn. obj.	high	high	medium	low
typ. other traffic:				
heavy traffic	rare	frequent	frequent	usual
bicycles	usual	usual	frequent	never
pedestrians	usual	usual	rare	never

c being the propagation speed in a medium. In vacuum the propagation speed c equals the speed of light c_0.

$$\frac{P_r}{P_t} = \frac{A_r A_t}{r^2 \lambda^2} \tag{2.1}$$

The effective antenna aperture is the area of an antenna, which is sensitive to electromagnetic waves. It corresponds to

$$A_e = \frac{\lambda^2}{4\pi} G \tag{2.2}$$

including the antenna gain G [56]. Inserting in (2.1) leads to a more convenient formulation in (2.3).

$$\frac{P_r}{P_t} = \frac{G_t G_r \lambda^2}{(4\pi r)^2} \tag{2.3}$$

In (2.3) only one-way propagation is assumed. For two-way propagation and a reflecting target, the radar cross section (RCS) σ of a target needs to be included with its target gain G_σ (2.4).

$$G_\sigma = \frac{4\pi\sigma}{\lambda^2} \tag{2.4}$$

During signal propagation through a medium, a signal gets attenuated, whereas the level of attenuation depends on the signal frequency or wavelength, respectively. In (2.5) the free space attenuation is stated for line-of-sight (LOS) propagation [56].

$$a_{FS} = \frac{4\pi r}{\lambda^2} \tag{2.5}$$

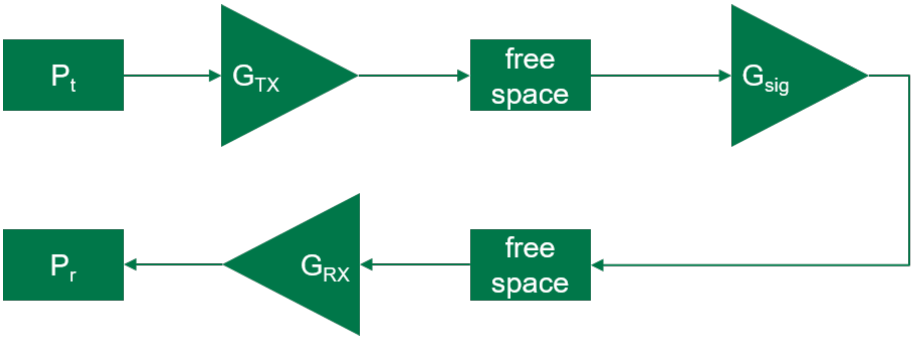

Figure 2.1 – Friis formula for two-way radar signal propagation

Increasing the frequency and therefore reducing the wavelength results in a higher free-space attenuation as can be derived from (2.5). As the term *long range* in automotive applications still refers to rather short distances from general radar perspective, see Table 2.4, the free space attenuation at 77 GHz is not an issue here, but on the contrary even beneficial regarding interference. Following the signal path in Figure 2.1 with the transmit power P_t and inserting (2.5) and (2.4), the receive signal power results in (2.6).

$$P_r = P_t \cdot \frac{G_t G_r \lambda^2 \sigma}{(4\pi)^3 r^4} \tag{2.6}$$

The received signal power P_r usually changes in non-static measurement settings, as the gain as well as the target RCS usually do not have an isotropic directivity, but are dependent from the elevation angle ϑ and azimuth angle φ. Nevertheless, in the following the channel and the target attenuation resulting from (2.6) are assumed to be stationary during an ongoing signal acquisition. To determine the minimum required transmit power, the noise power P_N has to be included in (2.6). The noise power P_N in (2.7) depends on the Boltzmann constant k, the ambient temperature T_a and the noise bandwidth B_N, which often corresponds to the system bandwidth. The noise figure N_f factors in the noise of the transmit and receive stages. Together with the ambient temperature, the system temperature is $T_{sys} = T_a \cdot N_f$.

$$P_N = k \cdot T_a \cdot F_n \cdot B_N \tag{2.7}$$

The minimum required signal-to-noise-ratio $\mathrm{SNR}_{Thr} = \frac{P_t}{P_N}$ depends on the signal acquisition method and transmit waveform, e.g. pulsed or continuous transmit signal. With a specified threshold signal-to-noise-ratio (SNR) the minimum receive signal power can be specified according to (2.8).

$$P_{R,min} \geqslant P_N \cdot \mathrm{SNR}_{Thr} \tag{2.8}$$

The assumption of a non-fluctuating environment is also made for the targets [84]. Still, the targets are moving but it is assumed that they do not accelerate during one radar snapshot, meaning the velocity of the moving target remains constant. In radar applications, targets are any reflecting points in the illumination field of the radar. Although that implies that objects usually consist of several targets, for the sake of simplicity of analysis any object in the field-of-view (FoV) is represented with only one point-scattering target. For the overall objective of this work, it is a sufficient level of detail to analyze the overall problem statement. Each of the L targets in the scenario is associated with a attenuation a_l on the transmit signal according to the previous considerations regarding propagation medium, target range r_l and target radar cross section (RCS) σ_l. The round-trip propagation time of the transmit signal to each target is

$$\tau_{r,l} = \frac{2r_l}{c_0} \ . \tag{2.9}$$

The range r_l refers to the distance between a reflecting point and the sensor position. The targets move with the velocity $v_{t,l}$ and the ego-vehicle with the velocity v_e. The resulting relative velocity $v_l = v_e - v_{t,l}$ introduces the Doppler shift $\tau_{D,l} = \frac{-2v_l t}{c_0}$. A common example for the Doppler shift is an approaching and veering away ambulance with its changing horn tone. Neglecting the radial velocity, the overall time shift $\tau_{s,l}$ for each target results in (2.10).

$$\tau_{s,l} = \tau_{r,l} + \tau_{D,l} = \frac{2\left(r_l - v_l t\right)}{c_0} \tag{2.10}$$

In the following section 2.1.2 (2.10) will be needed for the signal models at the receiver side. Any other models tackling signal propagation rely on (2.10) as well.

2.1.2 Basic radar architectures

There are two basic approaches for radar illumination and according signal waveforms, i.e. pulsed and continuous-wave (CW) [36]. In the following, signal acquisition and processing methods are explained for both radar principles, i.e. pulsed and CW approaches.

Pulsed radar systems transmit in the most simple implementation single pulses at the beginning of the time interval T, which is called pulse repetition interval (PRI). The pulse repetition frequency (PRF) is the inverse of the PRI and defines in implementations with uniformly spaced pulses the frequency of the pulse transmission with $\text{PRF} = T^{-1}$ [62]. In practical implementations usually a pulse train instead of a single pulse is transmitted to increase the systems SNR. According to the time-of-flight (ToF) principle, after transmitting a pulse the time until the pulse returns is taken. This time is usually referred to as round-trip time and corresponds to $\tau_{r,l}$ in (2.9). In Figure 2.2 the transmit and receive signals of a simple pulsed radar are

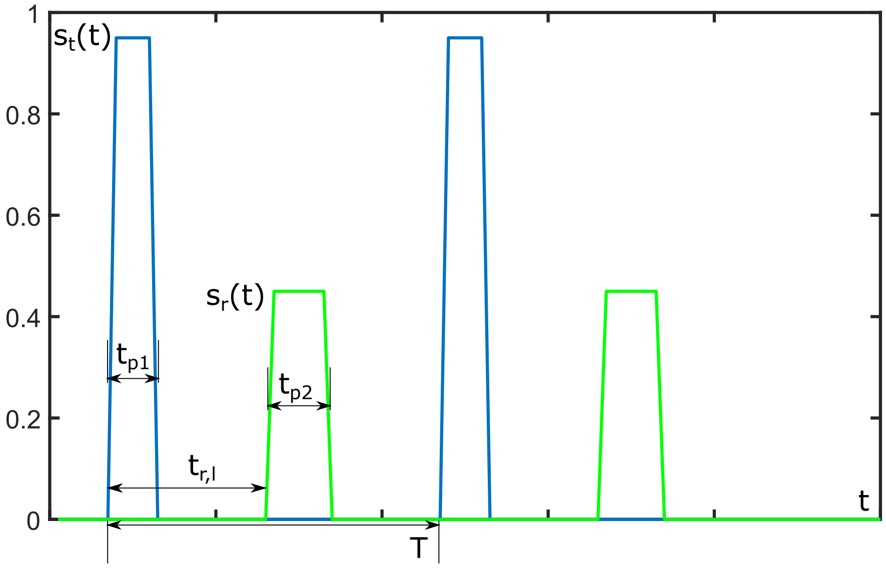

Figure 2.2 – Principle of pulsed radar

depicted in the time domain. In blue the transmit signal $s_t(t)$ has the pulse width t_{p1} and is repeated after the period T. The receive signal $s_r(t)$ is attenuated according to the medium, free-space propagation path and target reflectivity and its resulting RCS. Apart from the signal attenuation, the signal propagation through the medium also results in a widening of the transmitted pulse, therefore the pulse width of the receive signal turns into t_{p2}. According to the Nyquist-Shannon sampling theorem, direct sampling requires a sampling frequency higher than the double maximum frequency that occurs in a signal. A pulse with steep slopes such as depicted for example in Figure 2.2 therefore includes very high frequencies [40] and accordingly necessitates sampling frequencies that hardly can be realized with a reasonable effort. Another alternative approach can be found in the use of the cross-correlation function (CCF) such as in correlation receivers. The principle behind the correlation approach is to compare the receive signal against different conjugate-complex and time-shifted versions of the transmit signal that are part of a filter bank and search for the filter that generates the CCF with the highest peak.

$$r_{xy}(\tau) = \int_0^T s_r(t) \cdot h(t-\tau)\,\mathrm{d}\,t \tag{2.11}$$

In (2.11) the correlation principle is stated, whereas the filter function $h(t-\tau)$ is the conjugate-complex of the transmit signal $s_t(t)$ shifted by τ. A correlation receiver consists of a filter bank with N filter functions $h(t-\tau_n)$ to determine N different time-shifts τ_n. In Figure 2.3 the CCF is plotted for $s_t(t)$ and $s_r(t)$ in Figure 2.2. The flat top results from the widening of the pulse, i.e. $t_{p1} \neq t_{p2}$ and the center of the flat peak corresponds to the round-trip time $t_{r,l}$.

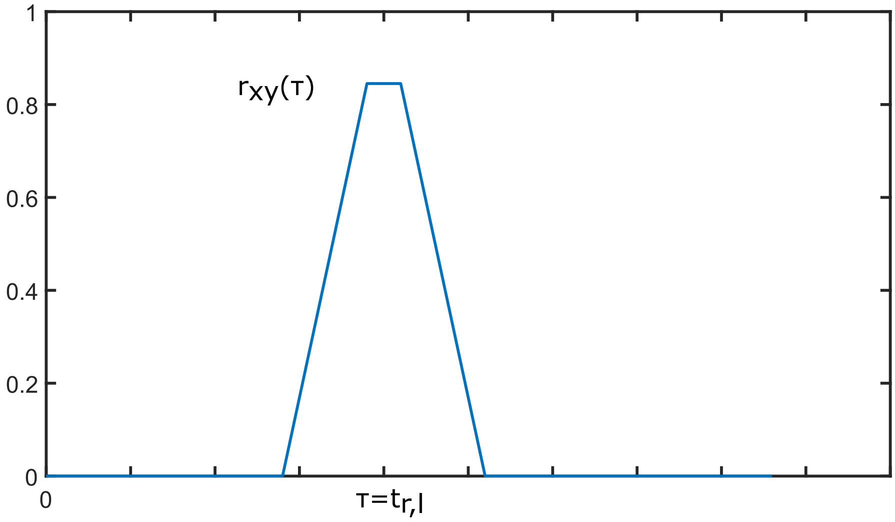

Figure 2.3 – CCF output of pulsed radar

The minimum detectable signal power for a pulse radar can be derived from (2.3) by factoring in the signal power. With the transmitted energy E_t and the pulse width t_p, the transmitted signal power is [84]

$$P_t = \frac{E_t}{t_p} \ . \tag{2.12}$$

Inserting the noise power $N = N_0 \cdot B$ leads to the minimum signal power in (2.13).

$$P_{r,min} = kT_{sys} \cdot \frac{E_t}{t_p \cdot N_0} \tag{2.13}$$

An increased pulse width enables the detection of a lower signal receive power, which allows to detect the backscatter from targets in long distances. Vice versa, increasing the pulse width reduces the range resolution, since it depends directly on the pulse width for unmodulated pulses.

$$\varDelta r = \frac{ct_p}{2} \tag{2.14}$$

FMCW radar systems A widely used alternative principle is the frequency modulated continuous wave (FMCW) radar, which applies continuous transmit waveforms. In automotive radar systems using chirps, the FMCW principle is applied as well [55]. As the term implies, the pulse of the transmit signal is replaced by a continuous wave that is modulated in frequency. Therefore, the direct sampling effort decreases to twice of the frequency range that is covered by the modulation. In Figure 2.4 the transmitted frequency $f_t(t)$ and the received frequency $f_r(t)$ with the same color scheme as before, i.e. blue for transmit and green for receive direction, are depicted. Here, a linear modulation is shown (Linear FMCW (LFMCW)), although other modulation schemes such as triangular are also common. In case of a LFMCW radar, a frequency ramp is transmitted. The gradient of the ramp is the quotient of the covered bandwidth B and the ramp duration, i.e. chirp length, T_c (2.15). This gradient is also called the chirp rate α.

$$\alpha = \frac{B}{T_c} \tag{2.15}$$

Including the start frequency f_1, the frequency modulation within an intervall corresponds to (2.16).

$$f_i(t') = f_1 + \alpha \cdot t' \tag{2.16}$$

Integrating (2.16) finally leads to the phase of the transmit signal (2.17).

$$\begin{aligned} \varphi(t) &= \int_0^t f_i(t') \,\mathrm{d}\, t' \\ &= f_1 t + \frac{1}{2}\alpha t^2 + \varphi_0 \end{aligned} \tag{2.17}$$

A single transmit chirp with $f_1 = 0$ and the phase offset $\varphi_0 = 0$ corresponds to (2.18).

$$\begin{aligned} s_t(t) &= e^{j2\pi\varphi(t)} \\ &= e^{j\pi\alpha t^2} \end{aligned} \tag{2.18}$$

The interested reader might want to see the underlying sources for the mentioned FMCW radar fundamentals in [43; 84]. During signal propagation the transmit frequency $f_T(t)$ changes according to the chirp rate, which is reflected in the frequency difference between the transmit and receive signal at the sampling time. For LFMCW radar systems, the range frequency $f_{r,l}(t)$ is computed with

$$\begin{aligned} f_{r,l}(t) &= \alpha \cdot \tau_{r,l} \\ &= \alpha \cdot \frac{2r_l}{c_0} \ . \end{aligned} \tag{2.19}$$

In addition, the receive frequency contains the Doppler shift f_D, if the illuminated scene contains moving reflecting targets.

$$\begin{aligned} f_D(t) &= \alpha \cdot \tau_{D,l} \\ &= \alpha \cdot \frac{-2v_{r,l}t}{\lambda} \end{aligned} \tag{2.20}$$

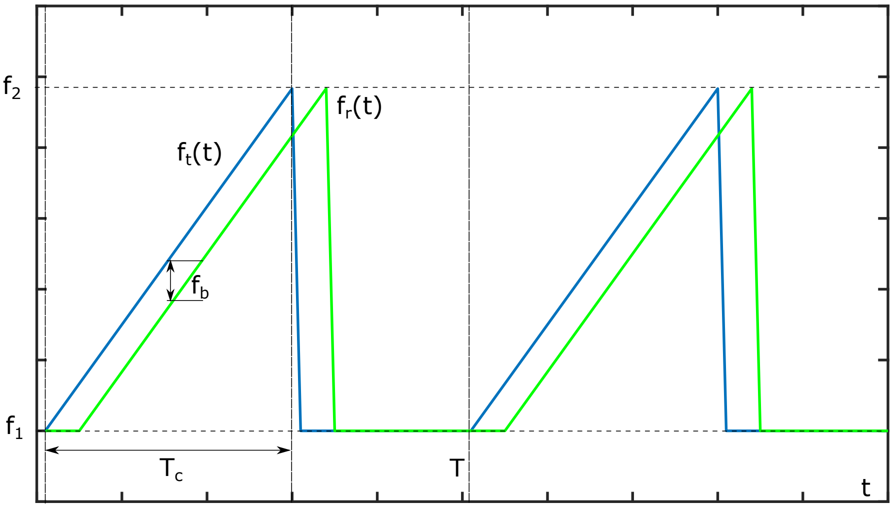

Figure 2.4 – Principle of FMCW radar

Both, the frequency difference caused by signal propagation $f_{r,l}(t)$ and the frequency change due to the Doppler shift $f_D(t)$, sum up to the beat frequency $f_b(t)$ in (2.21).

$$\begin{aligned} f_b(t) &= f_T(t) - f_R(t) - f_D(t) \\ &= \alpha \cdot t - \alpha \cdot \frac{2r_l}{c_0} - \alpha \cdot \frac{-2v_{r,l}t}{\lambda} \\ &= \alpha \left(t - \frac{2r_l}{c_0} + \frac{2v_{r,l}t}{\lambda} \right) \end{aligned} \tag{2.21}$$

Assuming the stationarity of the relative distance and velocity between the radar system mounted on the ego vehicle and a reflecting target l during one sweep, the beat frequency remains constant such as depicted in Figure 2.5. A radar sweep is here defined as a set of up-chirps that are used for resolving two dimensions, either range-velocity or range-azimuth. Usually, the beat signal is computed still on the RF hardware side before the analog-to-digital-converter (ADC) interface. Therefore, only the low-frequent beat signal needs to be sampled, which decreases the sampling effort significantly and leaves the effort of RF processing to the analog RF design stage. The range resolution depends on the modulation bandwidth B (2.22).

$$\varDelta r = \frac{c}{2B} \tag{2.22}$$

More insights on FMCW including measurements were given by the author in [33].

Chirp radar The two concepts, pulsed and continuous radar, are brought together with pulse compression, which is widely used in various radar technologies, e.g. chirp

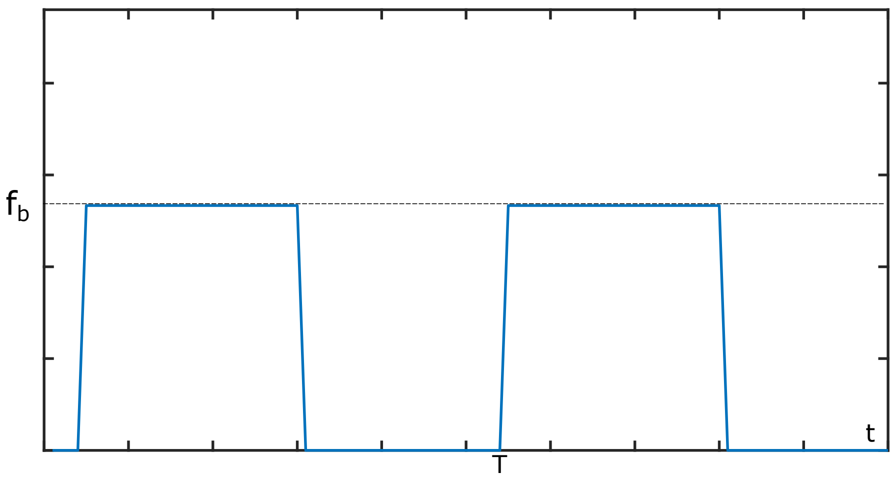

Figure 2.5 – Beat frequency at FMCW receiver

radar systems. Pulse compression means, that a pulse is modulated in frequency according to the desired bandwidth and the pulse is prolonged in the time domain [81]. The pulse compression rate (PCR) corresponds to the bandwidth-time-product (2.23).

$$\mathrm{PCR} = B \cdot T_c \tag{2.23}$$

Instead of the pulse width such as for an unmodulated pulse, the range resolution is determined by the bandwidth of the modulated pulse. For short sweep times, range cell migration can be neglected. Range cell migration occurs, if a target changes its position during one sweep. To sum it up, using chirps avoids on the one hand steep slopes and the necessity of fast ADCs, while on the other hand the range resolution is preserved. In general, pulsed approaches are mainly used for short distances, where correlation receivers lead to a still reasonable effort or ultrasonic sensors, whereas the propagation speed is far less than in electro-magnetic waves. But nevertheless, pulsed radar approaches are frequently discussed in the research domain, since its clear advantage lies in the robustness against noise.

2.2 Compressive Sensing

The significant increase of computational capacities paved the way to solve problems in a new way with algorithms that existed already for a long time but used to be computationally too intensive for real applications. Problems that were solved in hardware are now shifted to software, e.g. software-defined radio (SDR) that benefits from reducing costly RF engineering efforts and allowing low-cost and highly flexible software solutions. Since CS is an umbrella term for methods that profit from the sparsity and compressibility of any arbitrary signal, it covers applications from sub-Nyquist sampling [11] to signal reconstruction of incomplete measurements [31].

Figuratively, CS substitutes the complete sampling of a signal by projecting the signal of interest in another domain resulting in a reduced amount of observations. The original information contained in the signal, which is assumed to be sparse, is then traced back from the observations with the well-known projection functions. The projection is also called measurement or transformation, depending on the methodology that is required for a particular problem statement. Since the projection process is known as well as the set of basis functions, which are the constituting atoms of a signal in the particular representation domain, it is possible to identify the sparse components of a signal that are needed to reconstruct the original signal.

Together with a properly selected projection according to the basis functions, the original signal can than not only be approximated, but even exactly reconstructed. An intuitive example can be found in the Fourier series. While a sinusoid in the time domain requires sampling with the Nyquist frequency, only one sample needs to be taken in the frequency domain to obtain an undistorted sinusoid, i.e. the location of the single spectral component in the frequency domain. Therefore, Nyquist sampling is replaced by the Fourier transformation, i.e. the time signal is projected into the frequency domain. A good example for this is shown in [12] and a profound analysis is given in [11]. Accordingly, the signal acquisition results in a single sample that needs to be captured. The single sample allows not only an approximation but a complete reconstruction of the original signal, which summarizes the general idea behind CS approaches. Therefore, CS allows a significantly more efficient way of capturing the information contained in a signal and prevents taking a huge amount of redundant samples.

Whereas the time-frequency uncertainty states an almost intuitive example, complementary signal representation domains are sometimes less obvious or a transormation to another domain is required in order to find suitable and practical implementations. Accordingly, signals that are not sparse in the original observation domain, are transformed in some other domain, where a sparse representation is possible. The signal model consists in that case of a matrix $\mathit{\Psi}$ containing the basis functions, i.e. atoms of a signal to be acquired, and a sparse vector x that combines the basis functions to the final signal of interest f. Sparsity is defined as a low entropy in at least one signal domain and usually refers to the domain that offers a sparse signal representation. This is fulfilled thanks to the uncertainty principle that prevents a signal to be sparse in all domains at the same time such as the time-frequency uncertainty. In information theory, the uncertainty principle states [40; 70] that

$$B \cdot T \geq \sqrt{\frac{\pi}{2}} \tag{2.24}$$

holds. As a result, increasing the duration T of a signal, e.g. the pulse duration, decreases the bandwidth B and vice versa. Other examples are the trade-offs in simultaneous velocity and position measurements or optical wave-particle characteristics. Nevertheless, practical considerations for implementing a CS based signal acquisition system limits the choice of a projection domain, e.g. if the transformation would be too cumbersome or connected to an actual increase of hardware effort.

2.2.1 Signal acquistion using compressive sensing

Since CS comprises numerical estimation and optimization methods, signals and measurements are described with discrete signal models. This is reflected in the signal and measurement models as well as the metrics that apply to evaluate feasible matrix and reconstruction metrics. A basis matrix Ψ contains n basis vectors $\psi_n \in \mathbb{C}^{n\times 1}$, implying a quadratic matrix $\Psi \in \mathbb{C}^{n\times n}$. The target signal vector f can be decomposed into a linear combination of a subset of the basis vectors ψ_n, while the linear combination is specified by the signal vector x, see (2.25). That is true for the case that no transformation is necessary in order to obtain signal sparsity.

$$f = \Psi x \tag{2.25}$$

Relevant norms to determine the sparsity of x result from the problem statement and signal characteristic. As x defines the linear combination of the basis functions in Ψ, intuitively the ℓ_0-pseudo norm [24] applies.

$$\ell_0 : ||x||_0 := \{i : \; x_i \neq 0\} \tag{2.26}$$

It is not a closed definition, but the ℓ_0-norm reveals the amount of non-zero elements x_i that are contained in x. For small-scale problems representing an intuitive and comprehensive way of defining the signal sparsity, the ℓ_0-norm is a simple and straight forward norm. But for medium- or large-scale problems, that are actually the normal, the application of this norm would result in an expensive brute-force approach during reconstruction. An alternative metric that not only gives a closed definition but also allows to apply more efficient algorithms, expresses the sparsity s with the ℓ_1-norm [24] in (2.27).

$$\ell_1 : ||x||_1 = \sum_i x_i \tag{2.27}$$

It was shown in [26] that for sufficiently sparse vectors x_i, the ℓ_1-norm converges to the ℓ_0 norm and can therefore be used to implement efficient reconstruction algorithms. As a result, minimizing the ℓ_1-norm instead of the ℓ_0-norm is equivalent to the signal sparsity for sufficient sparse signals and states the optimization objective during the reconstruction process. Designing a signal acquisition concept that uses the principles

of CS, requires a profound understanding of the signal that should be captured and, even more important, the desired information that should be reconstructed. These considerations lead to an adequate design of the transformation or projection matrix, respectively. A projection matrix Φ reduces the number of samples that are required in Nyquist sampling for vector $x \in \mathbb{C}^{N \times 1}$ by the sub-sampling rate $\frac{M}{N}$ with the reduced number of samples M.
With M projection or transformation functions φ_m and $M \ll N$, it becomes a rectangular matrix with $\Phi \in \mathbb{C}^{M \times N}$. Together with the basis functions, the measurement matrix $A \in \mathbb{C}^{M \times N}$ is established.

$$A = \Psi \cdot \Phi \tag{2.28}$$

The measurement matrix A needs to be orthonormal in general [13]. Given the basis matrix Ψ, the measurement matrix Φ is required to be orthogonal to the basis matrix [10; 16] to allow a robust signal reconstruction afterwards. It is aimed for, to find the most incoherent matrices Ψ and Φ in order to reduce the number of required measurements [18]. Remembering the uncertainty principle, a signal that has a sparse representation in one domain, cannot be sparse in another orthogonal domain at the same time. The orthogonality or incoherence, respectively, is measured with the mutual coherence $\mu(\Phi, \Psi)$ [75], that describes the maximal similarity between any individual basis function φ_i and measurement function ψ_j.

$$\mu(\Phi, \Psi) = \max_{1 \leqslant i,j \leqslant M,N} = |\langle \varphi_i, \psi_i \rangle| \tag{2.29}$$

Often, the mutual coherence is normalized to the Euklidean norm, i.e. the ℓ_2-norm, of the basis and measurement functions.

$$\mu(\Phi, \Psi) = \max_{1 \leqslant i,j \leqslant M,N} = \frac{|\langle \varphi_i, \psi_i \rangle|}{||\varphi_i||_2 ||\psi_j||_2} \tag{2.30}$$

The theoretical minimum number of measurements that are required for a robust signal reconstruction, is computed with (2.31)[12].

$$M \geqslant \mu^2(\Phi, \Psi) \cdot s \cdot \log(N) \tag{2.31}$$

In acquisition methods according to CS principles, the mutual coherence on the one side and the signal sparsity on the other side are crucial in order to guarantee the uniqueness of a solution of the reconstruction problem statement.

Finally, the CS signal acquisition comprises the spatial products between the signal representation $x \in \mathbb{C}^{N \times 1}$ and the measurement matrix $A \in \mathbb{C}^{M \times N}$ that result in the measurement observations or projections $b \in \mathbb{C}^{M \times 1}$, whereas $M \ll N$. Therefore, although CS methods are applicable to a wide range of application fields including

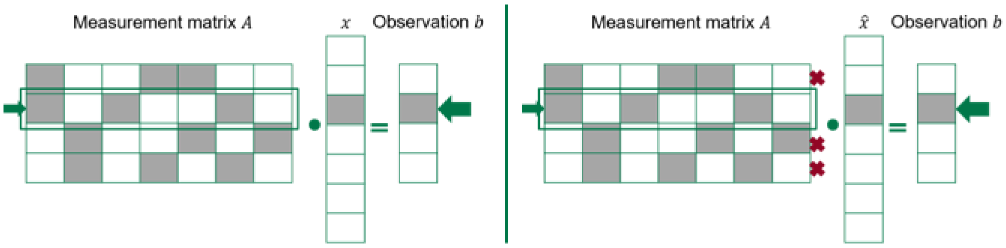

Figure 2.6 – Simplified CS principle of signal acquisition and reconstruction. Left hand side: Measurement of x and projection into observation b. Right hand side: Reconstruction $\hat{x}$ is determined by finding the only measurement vector in A that explains the observation b

.

inherent conventions regarding denotation, the CS application and optimization problem can always be broken down to the following equation (2.32).

$$\begin{aligned} b &= \Psi\Phi \cdot x \\ &= A \cdot x \end{aligned} \tag{2.32}$$

In Figure 2.6 the simplified principle of CS is depicted in a nutshell. The known measurement matrix A results in the known observation b. During reconstruction, the unique linear combination between A and $\hat{x}$ is determined, which explains best the observation b at the receiver.

2.2.2 Signal reconstruction

The observation b resulting from the CS signal acquisition, is simply the linear combination of A and x, whereas only x is unknown. In most cases, where $M \geq N$ and the system of equations can be solved uniquely, the aim is to reduce the number of measurements, which is widely called sub-Nyquist sampling in the literature. An under-determined linear system of equation such as (2.32) comes with an ambiguous solution space. Finding a unique unambiguous solution therefore requires additional information about the reconstruction objective and the expected signal.

At this point, sparsity comes into play. With the boundary condition, that the unambiguous solution of the system of equations is with a high probability the sparsest one in the solution set, the unique solution is identified. The probability to fulfill that additional assumption for solving (2.32), is increased, the lower the mutual coherence $\mu(\Phi, \Psi)$ is. However, the sparsity stipulation also implies that the reconstruction cannot be conducted via least squares estimators, which minimize according to the minimum square error.

Instead, the under-determined linear system of equation in (2.32) is stated as a convex optimization problem in (2.33). It only converges to a convex solution

Table 2.5 – CS Denotations

Denotation	Dimension	Explanation
N	1	Number of measurements (Shannon-Nyquist)
M	1	Number of reduced measurements
f	$N \times 1$	target signal vector
Ψ	$N \times N$	basis matrix
ψ_j	$N \times 1$	basis functions
Φ	$M \times N$	measurement matrix
φ_i	$M \times 1$	measurement functions
x	$N \times 1$	signal representation of f
b	$M \times 1$	projected signal representation, observation
A	$M \times N$	reconstruction matrix
$\hat{x}$	$N \times 1$	reconstructed x
ε	1	residual error

space, if the previous assumptions regarding sparsity and mutual incoherence are right. Basically, (2.33) states the core problem statement of CS, thus solving the convex optimization problem resulting from the signal acquisition design, as basis pursuit (BP) [21; 75].

$$\min ||x||_1 \qquad s.t. \quad Ax = b \tag{2.33}$$

The previously called projection or measurement matrix A turns into the reconstruction matrix, but it is required, that the reconstruction matrix eqals the projection or measurement matrix. Technically, the reconstruction matrix can be re-generated for the reconstruction process with well-known deterministic generation functions, thus avoiding the necessity to preserve huge amounts of storage capabilities. In contrast to (2.33), where only a perfect signal reconstruction is allowed, the reconstruction objective is relaxed in (2.34) by allowing a reconstruction tolerance of ε. Besides factoring in noisy propagation channels or noise from quantization, the relaxed formulation allows also to stop with a feasible approximation of the reconstruction.

$$\min \|\hat{x}\|_1 s.t. \|b - A\hat{x}\|_2 \leq \varepsilon \tag{2.34}$$

The minimization problem stated in (2.34) is a norm approximation method with quadratic constraints. As it takes noise into account, the problem statement is referred to as basis pursuit denoising (BPDN) and for practical reasons one of the most common problem statements within CS [23; 28]. An overview of the used CS denotations is given in Table 2.5. For perfect reconstruction without narrow run-time restrictions, for example interior point algorithms can be used. Computationally much more efficient and for practical applications sufficient are approximation algorithms. Greedy algorithms are therefore widely applied, among them the orthogonal matching pursuit (OMP) that is analyzed in [98] and can be seen as the most basic and common reconstruction algorithm within CS.

In principle, the OMP method computes for each iteration a residual vector r and determines the maximum spatial product obtained with the measurement matrix A. Instead of including all columns of A at once for reconstruction, at each iteration a column is added to the auxiliary matrix A_t that contains the selected subsets of A. The row, that provides the maximum spatial product between A and the current residual, is indexed by λ_t. In each iteration step, the subset matrix A_t is then updated with the λ_t-th row of A.

$$\lambda_t = J\{\max \left\langle A^H, r \right\rangle\} \tag{2.35}$$

Using the updated subset matrix A_t, a new subset estimate for x is computed by using a least squares (LS) estimator.

$$x_t : \quad \min \|b - A_t \cdot x_t\|_2 \tag{2.36}$$

For the following iteration step, the new residual r_+ is computed.

$$r_+ = b - A_t \cdot x_t \ . \tag{2.37}$$

Especially the computation of the subset estimate in (2.36) is subject to various optimization approaches resulting in a variety of OMP derived algorithms that are often tailored to particular applications. Nevertheless, the OMP is able to solve a wide range of problem statements. Therefore, if no fine-tuning is necessary, OMP can almost always be applied. In Appendix 2 BPDN as well as several OMP implementations can be found.

2.3 Weather Conditions in Automotive Context

Although weather usually plays a minor role for radar perception, which is one of the reasons that makes it interesting as an additional sensor for automotive environment perception in the first line, adverse environment conditions cannot be neglected completely. That is especially true for ultimate near-range effects, such as splash water. As an additional source of signal distortion or attenuation, research is required to find out particular impacts of adverse weather conditions that disturb the radar backscatter in a performance limiting way. Furthermore, the impact of adverse weather conditions needs to be contextualized with the capabilities of other sensor systems.

Rain has various effects on the overall radar measurement scenarios, i.e. effects on the propagation channel, the target reflectivity and hence radar cross section, clutter, and the radome of the transmitting and receiving radar itself.

Table 2.6 – International Visibility Code and 77 GHz Attenuation

Weather condition	Precipitation	Intensity [mm/h]	Visibility [m]	Attenuation @ 77 GHz [dB/km]
Light fog	Storm	100	770	27.34
Very light fog	Strong rain	25	1900	10.95
Light mist	Average rain	12.5	2800	6.70
Very light mist	Light rain	2.5	5900	2.12
Clear air	Drizzle	0.25	18100	0.41

2.3.1 Definitions and Recommendations on Weather Conditions

In order to make radar systems comparable to other sensor systems and design an appropriate test system, a joint definition of weather conditions is required. The recommendation [71] provided by the ITU states a widely used definition for terminologies that identify the intensities of rain and visibility. Visibility is the distance, where the contrast drops by 2 % at a wavelength of 550 nm [71]. The visibility is computed according to the Koschmider relation with the attenuation coefficient γ_{550nm} in $1\,\mathrm{m}^{-1}$.

$$V(m) = \frac{3912}{\gamma_{550nm}} \tag{2.38}$$

In Table 2.6, the visibility is listed according to the recommendation and put into context of descriptive terminology for fog and precipitation intensities. The attenuation at a center frequency of 77 GHz is computed according to (2.39), (2.40) and (2.41). Visibility refers to atmospheric attenuation on optical signals for communication, such as infrared or laser that are transmitting signals actively. For optical perception sensors, in particular sensors that do not use an active illumination of the scene such as the widely used cameras, near-field influences and focal length are subject to a drastic limitation in visibility, e.g. because of blurring rain drops on the camera lens [34]. Of course, the passive perception design of cameras is disadvantageous for the robustness regarding object detection in the first place, when compared to active illumination systems.

The damping effects on the signal propagation are correlated to the statistical rain drop RCS and the statistical distribution of the rain drops in a volume. With statistical distribution probabilities, it is possible to link the rain drop size and rain drop distribution to rain intensities that are used to compute specific rain attenuations.

Although the correlation between rain drop size and rain intensity substantiated by [53] is applicable to camera based sensor systems, it is not valid for radiation waves below 10 cm, i.e. radar at 77 GHz. The Marshall-Palmer distribution works for the assumption of Rayleigh distributed rain drops, which is true for systems such as cameras or common weather radars, but it cannot be assumed for rain drop distributions from the perspective of automotive radar. Instead, the Mie-distribution needs to be taken into account [71; 93].

According to the recommendation ITU-R P.838-3 [93], the specific attenuation γ_R[dB/km] is computed depending on different rain rates R[mm/h] as stated in (2.39).

$$\gamma_R = kR^{\alpha} \tag{2.39}$$

The coefficients k and α are computed based on the coefficients $\{k_V, k_H\}, \{\alpha_V, \alpha_H\}$ together with the path elevation angle ϑ and the polarization tilt angle τ according to (2.40), (2.41).

$$k = \left[k_H + k_V + (k_H - k_V)\cos^2 2\tau\right]/2 \tag{2.40}$$

$$\alpha = \left[k_H\alpha_H + k_V\alpha_V + (k_H\alpha_H - k_V\alpha_V)\cos^2\vartheta\cos 2\tau\right]/2k \tag{2.41}$$

In [93] the frequency specific values for k and α are given, so that the according rain attenuation at 77 GHz can be computed. The rain attenuation is displayed in Figure 2.7 depending on the two-way propagation path length in the region of up to 400 m. In common advanced driver assistance systems (ADAS) ranges above 200 m are not considered anymore, therefore this distance was assumed as the maximum region of interest in automotive applications. Furthermore, Figure 2.8 shows the course of the rain attenuation along rain intensities ranging from light rain with $0.1\,\mathrm{mm\,h^{-1}}$ up to very heavy rain with $50\,\mathrm{mm\,h^{-1}}$ for comparison. The graphs in Figure 2.7 and Figure 2.8 show that although the specific rain attenuation cannot be completely ignored, it does not play a major role for radar signals at 77 GHz. Among others, this fact justifies radar as an important brick within a whole sensory system for safety critical implementations such as the aforementioned autonomous vehicles.

2.3.2 Adverse environment conditions in automotive scenarios

In section 2.3.1, the specific rain attenuation was introduced. The model of the specific rain attenuation relies together with the free-space propagation on the far-field assumption. Recalling Frii's equation in (2.42), the received power depends on the gain of the transmit antenna G_T and the receive antenna G_R. It neglects the antenna aperture, which in practice is not isotropic but has different sensitivities depending on the direction of arrival (DoA). In addition, the antenna gains are

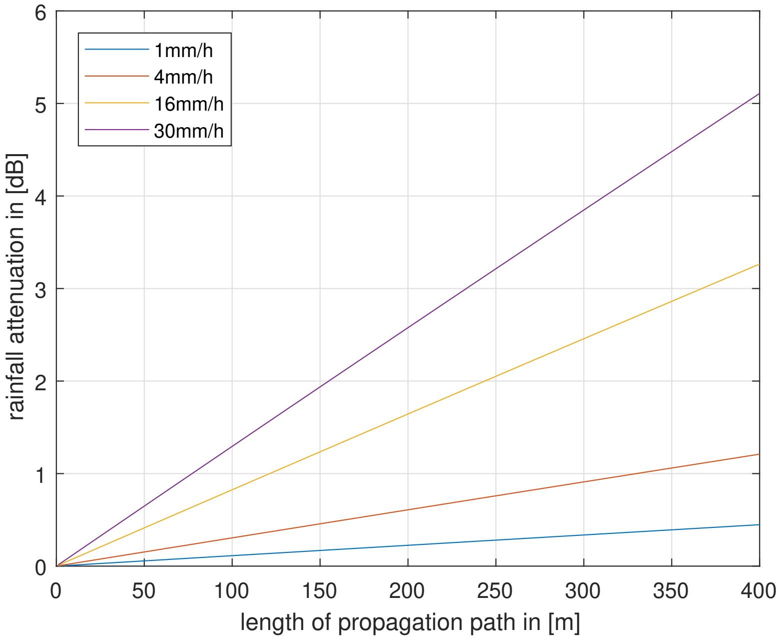

Figure 2.7 – Rain attenuation at 77 GHz depending on the path length at different rain rates

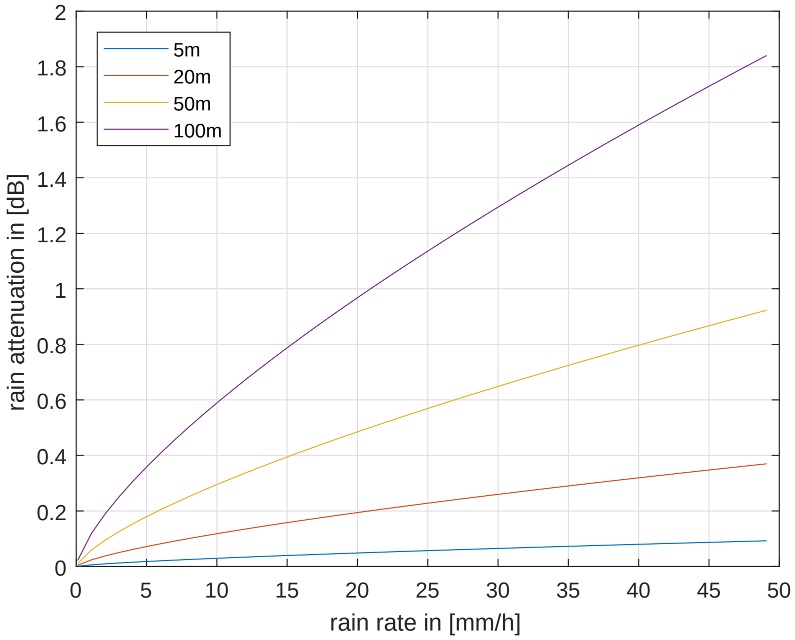

Figure 2.8 – Rain attenuation at 77 GHz depending on rain rates at different distances.

assumed to be constant over frequency. Both simplifying assumptions can be made because of the far-field assumption.

$$P_R = \frac{P_T G_T G_R c^2}{(4\pi r f)^2} \tag{2.42}$$

The far field begins at the minimum distance $r_{ff,min}$ according to (2.43), given the maximum antenna dimension d and the wavelength λ [94]. In case of planar antennas, (2.43) can be used to obtain the maximum coverage in elevation direction depending on the antenna height [57]. Then d refers to the maximum dimension of an object with an reflecting surface of higher complexity.

$$r_{ff,min} \geqslant \frac{2d^2}{\lambda} \tag{2.43}$$

Applications in the closer vicinity below 100 m require maximum dimensions below 20 cm. Therefore, the far field assumption needs to be dropped for most realistic automotive cases. Considering the near-field instead, the spatial directivity of the antenna depending on the radiation intensity $U(\vartheta, \varphi)$ for both, elevation angles ϑ and azimuth angles φ and the total power input to the antenna P_{in} need to be taken into account.

$$G(\vartheta, \varphi) = \frac{4\pi U(\vartheta, \varphi)}{P_{in}} \tag{2.44}$$

In case of using a transmit signal that comprises a wide bandwidth, it needs to be considered that the effective aperture A_e that translates into physical antenna dimensions, actually depends on the transmit frequency.

$$A_e = \frac{Gc^2}{4\pi f^2} \tag{2.45}$$

Since the once implemented physical aperture of the antenna A_{e0} remains the same, the varying antenna gain cannot be neglected anymore in contrast to narrow-band applications.

$$G(f) = \frac{4\pi f^2 A_{e0}}{c} \tag{2.46}$$

As a consequence it is crucial to gain a deeper understanding of near-field effects and impacts. While far-field rain effects can be easily neglected, near-field effects that occur specifically in the automotive context and have a direct impact for example on the radome, need to be determined.

Accordingly, ground clutter and changes on the ground clutter due to different street conditions need to be taken into account. Ground clutter is directly connected to surface characteristics, such as roughness, relative dielectric constant ε_r of the material and incident angle. The roughness of the surface is classified according to the wavelength and differential height Δh on the surface. For $\Delta h < \frac{\lambda}{4}$, the surface is specular to the radar signal and nothing will be reflected back to the radar. As a consequence, co-located radar systems will not receive any backscatter there. Rough surfaces are assumed for $\Delta h > \frac{\lambda}{4}$ and a co-located radar system will receive a strong echo. Ground clutter is described with the cross section per unit area $\sigma^\circ \frac{m^2}{m^2}$ and depends on the roughness related scattering effectiveness γ and grazing angle on the surface Φ [8].

$$\sigma^\circ = \gamma \sin \Phi \tag{2.47}$$

$$\sigma = \sigma^\circ A \tag{2.48}$$

Another typical near-field effect are particles such as dust or mud. Wether particles disturb the radar signal perception, depends on the particle size and density. The particle size contributes to the RCS of a particle, same as any other target. Another parameter, that influences the RCS is the reflectivity r_ε in the transition between two materials or propagation media (2.49). The dielectric constant ε_r of air is approximately $\varepsilon_0 = 1$.

$$\begin{aligned} r_\varepsilon &= \left(\frac{\sqrt[2]{\varepsilon_{r1} - \varepsilon_{r2}}}{\sqrt[2]{\varepsilon_{r1} + \varepsilon_{r2}}} \right)^2 \\ &= \left(\frac{\sqrt[2]{\varepsilon_r - 1}}{\sqrt[2]{\varepsilon_r + 1}} \right)^2 \end{aligned} \tag{2.49}$$

Water has a quite high dielectric constant with $\varepsilon_w = 80$, resulting in a very high reflectivity. Organic materials usually have a reflectivity of $2 \leqslant \varepsilon \leqslant 5$. Accordingly, the reflectivity of organic components lies between $0.33 \leqslant r_\varepsilon \leqslant 0.67$. The minimum thickness of particles to be visible for radar depends on the wavelength λ_c of the center frequency.

$$T_m = \frac{\lambda_c}{2\sqrt{\varepsilon_r}} \tag{2.50}$$

Therefore, particles are completely transparent to the radar, if their thickness is below 0.87 mm or 14 mm. In general, it is fair to assume that in automotive scenarios with its metallic vehicles and pedestrians are much stronger scatterers than particles, so that their influence can be neglected there.

3 State of the Art

The context for analyzing new radar architectures and advanced signal acquisition methods is given by two major fields, namely signal processing and hardware development. Increasing computational power allows to consider the application of CS methodologies in the automotive context. CS methodologies allow efficient sampling. But CS also comes with high computational effort. Having the possibilities of CS methods in mind, a fresh view on the targeted application field with its traditional processing schemes is possible.

Accordingly, the aim is to proceed in solving arising challenges in radar applications that are specific to automotive radar. Many methods that are widely used in other radar applications, could not be transferred to the cost-sensitive automotive market, which additionally used to have limited interest in radar technologies in the first line. However, along with the developments towards autonomous driving, radar becomes an important part of safety-critical ADAS. Given the fact that radar takes over safety relevant functionalities, a wide field of radar methods can be considered now for environment perception, whereas CS increases their efficiency by reducing signal acquisition effort.

All of this is reflected in the structure of the state-of-the-art chapter. First, an overview on CS is given, that partially comprises radar topics. In the second part, the field of radar methodologies and techniques is illuminated with spotlights on radar systems and processing methods that are relevant for the automotive application fields.

3.1 Applications of Compressive Sensing

Although CS became an emerging field in the research community during the last decade, many of the mathematical and signal processing techniques are mostly well-known for a long time. Partially, single components of CS methods even belong to the state-of-the-art in radar signal processing as pointed out in [29]. However, only the development of increasingly powerful digital signal processors (DSPs) paved the way to implement CS techniques for a wider range of applications. It was rather the work of Candès, Romberg and Tao in [13], who showed and proved that the ℓ_1-norm is a feasible approximation of the ℓ_0-pseudo-norm and explained how a stable signal recovery can be obtained from incomplete measurements.

Since then, research emerged in order to analyze where the application of CS is beneficial and helps to solve either problems that could not be solved before or to solve them more efficiently. For CS, a discretized signal structure is essential as its algorithms tackle numerical optimization. Consequently, image processing is a particular popular field of application for CS with its discretized signal structure resulting from the pixels. Hence, even one of the first rare hardware realizations was a single pixel camera [20]. The functionality of the single pixel camera, especially regarding the role of CS, was explained in [12; 76]. Later on, the single pixel camera approach was enhanced by a parallel processing structure [7]. Another work within imaging that addresses a different domain of sparsity than most imaging approaches is [73]. This paper gives another perspective on CS, specifically how to address multi-sensor systems. Instead of the intuitive sparsity domain, Bayes probability is used as sparsity domain. The idea is to reduce data transmission in multi-sensor systems in a way, that only changes in individual sensor outputs are transmitted, which is the actual aimed information. Although that works mainly for industrial plants with huge amounts of distributed observation sensor systems, the use of Bayesianity is also a promising approach for sensor data fusion in sensor-equipped systems that include a high diversity. Therefore, the presented approach is interesting for communication technology in vehicle to vehicle (V2V) and radar systems.

The aforementioned few hardware implementations outside of optical imaging applications are also caused by the lack of discrete signal representation in different applications, whereas the sampling itself and therefore discretization of the signal is subject of the problem to be solved in analog signals. In order to apply CS to sampling or analog signal acquisition in general, the measurement process needs to be well-known for a robust reconstruction basis. The challenge lies therefore in reducing the sampling effort with random measurement signals, that are at the same time deterministic for the reconstruction part. That is, to avoid the necessity for huge storage capacities in order to save all measurement signals. So the duality of deterministic signal generation with random structure, i.e. pseudo-random signals, needs to be resolved, if CS should be used for analog-to-digital (AD) conversion.

Exactly that problem was addressed in [51], where the reconstruction process was committed to silicon. Among other approaches that were discussed, reconstruction algorithms were implemented on field programmable gate arrays (FPGAs) in [51; 74]. One of the pioneer work regarding hardware implementations for CS signal acquisition outside of imaging technologies was contributed by Eldar and her group with their Xampling hardware [59; 60]. Their modulated wave converter (MWC) is a radar receiver based on CS that performs the signal acquisition on RF hardware.

The concept behind the MWC is to reconstruct the original wide-band signal from measurements of several sub-bands instead of capturing the complete broadband spectrum. Several narrowband converters perform the transformation into the frequency domain only for some randomly selected frequencies using CS to reconstruct the rest of it afterwards. Therefore, the Xampling approach can be also viewed in a way, that it extracts several random Fourier coefficients of the backscatter and reconstructs from the set of incomplete coefficients the remaining ones. The role of the RF receiver hardware is to modulate the received pulse in several parallel analog mixing lines with the corresponding coefficient transformation. This works for frequency modulated continuous chirp signals according to the usual practice in radio and especially radar technology.

Most of the other approaches address the signal processing part, so that any changes in the RF hardware part can be avoided. On the one hand, this is because of the additional effort regarding hardware design, which is also quite expensive and therefore it is hard to find convincing arguments for experimental hardware development with a newly arised methodology. On the other hand, at least in traditional radar applications, radar equipment is already designed in a very smart way comprising RF design experience from several decades, so that there needs to be a very good reason to just overthrow it. In addition, CS can enhance radar performance significantly on the signal processing side as well, so it is even more beneficial to check, how CS could be applied. A set-screw is the sampling method itself, while the hardware does not need to be changed. In [5] a non-uniform sampling approach was tested on the laboratory radar system (LabRadOr) of the Fraunhofer Institute. Using LabRadOr, measurements with a stepped frequency radar system were configured and performed. Similar to [59], the receive signal was transformed in the Fourier domain using random frequency allocations within the spectrum. But in contrast to [59] this was implemented in the time domain, i.e. instead of several random carriers the distance in between two sampling points was varied randomly, which results in randomly changing sampling frequencies. In the signal processing chain a constant false alarm rate (CFAR) detector was applied in combination with the CS ℓ_1-norm.

The non-uniform sampling approach is taken one step further in [46]. The CS based UWB radar sensor is supplied with randomly spaced transmit pulse trains. The time-spacing between two pulses corresponds to different round trip times of individual transmit pulses. Therefore, this approach is already close to correlation receivers, as the spacing in between the pulses covers different range gates. That is also, were the sparsity lies. Similar to the multi-sensor approach from the proposed imaging method in [73], a group wise sparsity was assumed. For the CS conforming representation of the UWB signal, the number of groups equals the estimated number of targets, whereas the total amount of targets is assumed to be sparse. In order to make sure to meet the hardware constraints, low-density parity check (LPDC) measurement matrices were used to check for non-negative integers, constant row sums other than zero and an unambiguous structure. The work in [46] extends the functionality of the chip that was developed in [14], whereas equidistant radar pulse trains were generated. In [14] the goal was to develop a chip without addressing CS or any other signal processing approach. Later on, this chip was enhanced in [19] with an electro-static discharge (ESD) protection and a serial interface.

A fully integrated CS signal acquisition system was designed and implemented in [102]. Using a bandwidth of 2 GHz and ±1-Bernoulli sequences for measurement, successful reconstructions were performed for a sub-sampling ratio of 12.5 %. The channel was assumed to be an AWGN channel, but neither the SNR nor the maximum range were mentioned in this work.

CS hardware for signal acquisition was brought to another level by [54], who developed a mechanical CS reflector antenna. The measurement matrix is here implemented mechanically by the antenna itself. Instead of focusing the signal in the center, it is scattered at the receiving antenna according to the designed surface of the antenna. Therefore, the surface pattern spreads the signal spatially, i.e. implementing a spatial diverse observation.

3.2 Radar

Radar has already a long history of implementation and diverse applications, at least outside of the automotive field. Therefore, there is a rich pool of methods in general radar application fields that can be used for developing new automotive radar-based functionalities. Because nowadays typical automotive radar systems do not use pure FMCW signals in the sense that they transmit continuous signals, but instead frequency modulated (FM) pulses, so-called chirps, the focus of the state-of-the-art description remains on pulsed radar. Section 3.2.1 covers already systems using chirps. In addition, the field of noise radar and CS in noise radar is elaborated. It should be noted that there is no completely unambiguous way of disentangling CS, pulsed, noise, and automotive radar, since the terms are not separate categories that exclude each other. Instead, CS comprises methodologies for signal acquisition and reconstruction, pulsed and noise radar architectures that are applicable as automotive radar architectures and finally pulsed radar systems comprising noise modulated pulses. Nevertheless, the breakdown of the state-of-the-art into these specific sections points out the main and most important ideas or solutions in its respective subdivision and pitches the concepts that are fruitful to the other sub-divisions as well.

3.2.1 Pulsed Radar

Pulsed radar, especially when unmodulated pulses are used, are problematic when it comes to direct sampling. In addition, a high transmit power is necessary to make sure to obtain a feasible receive power after pulse propagation within the respective propagation medium, e.g. free space. In practical implementations, short pulses with steep slopes are applied for short distances in controlled environments such as industrial plants and production lines.

A typical application for production lines is the level measurement, e.g. in tanks. A radar system for such a level measurement was developed in [100] using a very short pulse duration of less than 1.5 ns for a maximum range distance of up to 7 m with an accuracy of ±5 mm. The carrier frequency is allocated in the 5.8 GHz industrial-scientific-medical (ISM) band. Using time-stretching, the propagation speed of the backscattered signal is converted from speed of light to speed of sound before entering the detection path. Hence, the direct sampling problem is solved by time-stretching, enabling a direct sampling of the backscatter, while keeping the sampling effort low.

Another approach to avoid cumbersome direct sampling with high frequencies that is often used besides time-stretching is the digital-to-time converter (DTC). In [41] the vernier DTC is applied, that was implemented by using frequency comparison. Two slightly detuned oscillators, deviated from the same oscillating source, are used on the transmitter side. Applying edge detection, the lag between the transmitted oscillations is determined by evaluating the number of periods that both of the oscillators take until their edges overlap. Based on the detected time lag, which is the difference in the number of periods for both oscillations, the signal's round-trip time is computed.

Furthermore, UWB radar systems can be viewed as pulsed radar systems, since due to the time-bandwidth product a wide bandwidth results in a narrow pulse in the time domain. Therefore, acquisition challenges are partially the same as in a more conservative interpretation of the terminology pulsed radar. Accordingly, a method to handle signal acquisition for pulsed and UWB radar waveforms by avoiding direct sampling was presented and analyzed in [27] for an UWB radar system. During signal propagation of a transmit signal and until the arrival of an echo at the receiver, several capacitors are loaded by parallel current sources. As soon as an echo arrives, the actual charging status of individual capacitors is preserved while the other parallel capacitors continue to be charged. Hence, each echo is represented by a different state of charging thus allowing the detection of multiple targets. The number of targets is limited by the actual number of capacitors, limiting its application to a clear target environment. An additional drawback of this solution lies in the sensitivity towards noise that comes with relying on threshold levels.

The CS approach for pulse acquisition, namely the random modulated pre-integration (RMPI) pre-processor as proposed in [10; 11; 75], was designed and implemented in [102] as a fully integrated system. This CS based ADC projects the receive signal to several observations that can be sampled at comparably low frequencies. The reconstruction in the signal processing path leads to the computation of the inherent information. Hence, this type of ADC is actually also known as analog-to-information converter (AIC), since the process results in analog-to-information transformation instead of classical signal sampling. The RMPI is implemented with eight parallel convolution channels, that apply the pseudo-random measurement signals to the receive signal. Afterwards in the signal processing path, where a dictionary based reconstruction is implemented, Gabor and discrete cosine transformation (DCT) signals are chosen as basis functions.

3.2.2 Noise Radar

Initially, only few researchers were interested in noise radars, because in the early 1950ies and 1960ies the required electrical circuitry for analog signal processing was too expensive [45]. Only with the development of fast ADC chips and the increase of computational capacity, the research interest in noise radar systems could rise again. It should be noted, that this is the same reasoning for the increased research interest in CS. One of the major benefits of noise modulation is the low effort in generating it, if there are only low-key constraints given. For example, the most simple approach is to amplify thermal noise. Even if more complex implementations such as (pseudo-) random noise generators are used, it is still advantageous to use noise sequences for creating unique fingerprints in pulses while lowering the required power transmit power. Of course, situations, in which a transmit signal should be hidden in the overall noise floor such as for military use but also regarding privacy in civil applications, do benefit from noise shaped signals as well. In the following, an overview of noise radar research is given.

Two approaches regarding signal acquisition were presented and compared in [49], i.e. a stepped delay method on the one hand and a stepped frequency method on the other hand. The aim was to develop a design that avoids as much as possible the trade-off between a high resolution and a high dynamic range. Therefore, the radar architecture was designed to cover a wide bandwidth while still being able to use slow ADCs. The approach that uses stepped delays, computes the resulting energy of cross-correlations between the received backscatter and reference signals, whereas the cross-correlations are performed at the receiver stage. There, also the reference signals are generated as time-shifted versions of the continuous transmit signal, whereas the time-shifts are adjusted according to predefined time bins corresponding to different range gates. Instead of relying on real signal propagation on air, the fixed range in air with 120 cm was transfered to a propagation through a short-circuit cable with the length of 80 cm. The issue with the range side lobes is, that they cause interference when they are reflected by objects outside of the region of interest.

The drawback of the stepped delay method of the high range sidelobes is addressed with the second approach, the stepped frequency noise radar. With several narrow-band noise pulses that have different center frequencies, a continuous noise wave is synthesized. Afterwards, the signal processing is the same as in the stepped delay method, so that only the transmit signal is generated differently. Hence, the presented stepped frequency method is an improvement of the stepped delay method.

The fully polarimetric and phase-coherent random noise radar system that was developed in [65], features an actual RF frontend and antenna. On the transmitter side an UWB noise signal according to Gaussian distribution is generated. The signal bandwidth covers frequencies between 250 MHz and 500 MHz with an average power of 1 mW. The log-periodic antenna that is tailored to the wide signal bandwidth has a gain of 8 dBi and a 3dB-bandwidth of 100° in vertical direction and 40° in horizontal direction. During signal transmission the transmit antennas are switching between horizontal and vertical polarization. As opposed to the transmit antennas, the receive antennas receive the vertical and horizontal polarized backsatter simultaneously. Similarly to the previously described approach, the receive path comprises delayed versions of the transmit signal, that represent various round-trip times, i.e. target ranges. Here, the delayed versions were generated with delay lines to which the transmit signal is applied after passing a power divider. As a result, several reference signals are available, that are up-converted to 70 MHz and correlated with the received backscatter. Afterwards, the correlation output enter the I/Q detector, where the further signal processing takes place. With the resulting polarimetric range profile, terrain is classified on the one hand, such as ocean or forests, but on the other hand also objects are identified such as airplanes.

In the variety of radar applications, through-wall-detection (TWD) can also be found, which is adressed in [95]. A TWD radar system is basically a short range radar system and was developed here for the detection of human beings. Again, the receiver stage features correlators that are implemented as analog microwave correlators in this work. Analog correlation is advantegeous compared to digital correlation, in cases where otherwise a high effort in sampling due to high frequencies or bandwidth would be necessary. Consequently, also this approach avoids direct sampling by analog correlation. With the evaluation of the correlation output, characteristic patterns were identified, that included various situations such as a breathing, sitting or standing person. Due to the coherent receiver architecture it was possible to determine distance variations and velocities precisely and unambiguously. According to the authors, their radar system is also feasible for anti-collision applications.

As mentioned in the introduction, noise waveforms are well-suited for covert signal transmission, which was the driving motivation in [15], where such an implementation was analyzed and demonstrated. Although it is not a radar, the work demonstrates how noise can be applied in a RF context and actually allowing spectrum sharing, which is interesting for radar, too. The vertical and horizontal polarization of the transmit and receive antennas was exploited to transmit an information signal and a reference signal simultaneously. A power divider splits the initially generated noise signal before the transmit antennas to derive both signals from it. While one part of the signal is delayed by a tunable time delay, the other part is modulated by a bit sequence, resulting in the reference and information signal, respectively. Due to the underlying noise signal it is not possible to determine during free space propagation that a polarized information signal is transmitted. At the receiver side, the information signal can be only determined by reconstructing the reference signal based on the original signal delay from one of the polarized antennas. The critical point of this implementation is to design identical delay lines in both, the transmit and receive path. As long as the delay is only known to the transmitter and receiver, the receive signal cannot be interpreted by a third party user, who also needs to recognize the polarized information signal in the first line. Transferring this method to radar, the implementation can be also beneficial for radar without necessarily transmitting information bits. Multiple users can communicate while accessing the same frequency channel at the same time. It is possible to transfer the method for multiple radar users to illuminate the perception area at the same time. In addition, the proposed spread spectrum technique ensures with its noise waveform that enough signal power reaches the receiver stage, which is beneficial for both, radar and communication. This enables even an operation with SNR and signal-to-information (SIR) levels below zero.

In many applications it is desirable to perform the cross-correlations not in the analog but in the digital domain. That is for example the case for SDR developments, the necessity of flexible tuning of the CCFs, or when expensive hardware developments should be kept to the minimum. But digital correlation unveils one of the main drawbacks of noise radar systems, especially for random noise sequences. In the digital domain, the required signal processing time that is necessary to perform the correlations on the one hand and the memory capacity that is required to store the respective reference signals on the other hand put significant limitations to the implementation.

This was addressed in [97]. The authors used and developed further the initial work in [47], where it was shown that random noise radar (RNR) can be implemented with simultaneous range and velocity detection using digital correlators. The RNR was implemented with a bandwidth of 400 MHz. Their system consists of a direct conversion receiver (DCR) without a quadrature channel as known from regular heterodyne receivers, thus resulting in phase incoherency. The drawbacks regarding signal processing time and memory capacity are mitigated by parallelizing the computation of the correlations on two NVIDIA graphic processing units (GPUs). The parallelization is performed by splitting fast fourier transformations (FFTs) into overlapping segments with zero-padding.

The FFTs are applied on both, the reference and the receive signals before they are multiplied in the Fourier domain. As a result of splitting the FFTs in several segments, the reference signal is composed partially of the previous and the current signal. After multiplication, the result is transformed back by computing the inverse FFTs (IFFTs) for the segmented FFTs and the segments are accumulated again. Although the resulting computation time is still not close to real-time computation, that scalable approach proved its potential of reducing the run time significantly.

3.2.3 Compressive Sensing in Noise Radar Systems

After depicting the general research field for noise radar, it became clear that most research is primarily concerned with analog or digital correlation. Especially the problem statement regarding digital correlation at the receiver stage, which leads to significant runtime and memory capacity problems, is a promising field for the application of CS. Radar scenarios are often sparse in the spatial domain and the numerous performed cross-correlations is highly likely to be compressible.

Measurements using cross-correlation such as in conventional pulse or noise radar concepts are also the starting point for the various reconstruction approaches that were analyzed in [82]. The time-domain model of the transmit waveform is constituted as a random white noise process that is convoluted with low-pass filters (LPFs) that represent the band limiting non-idealistic real world system. The transmit bandwidth of the signal model was assumed to be 500 MHz. The measurements were performed by a regular designed radar system, only the signal reconstruction was adapted to the respective reconstruction method, whereas two of the four discussed methods relied on CS. That makes the evaluation of the four applied reconstruction methods especially meaningful, when compared against each other. One method applies cross-correlations between a filter bank that contains the reference signals and the receive signal. The other non-CS method provides a LS estimate by computing the Moore-Penrose-Inverse with the CCF matrix. The CS methods for reconstruction included ℓ_1-minimization using BPDN with quadratic constraints according to [12]. In one of the two CS approaches the complete set of references was used during reconstruction whereas in the second approach only a subset of 25 % of the total references was applied. Although in the case that considers the complete set of references the LS approach is more appropriate regarding reconstruction effort, the CS performance on the full set was still important in order to benchmark the capability of CS reconstruction on a reduced set of reference. The results were not compared against each other for various noise levels, assuming that noise can be negelected due to the narrow antenna beam of 1° and a low impact of noise in the considered scenario with a single highly reflecting target in the range of 33 m.

The similarity between image processing and synthetic aperture radar (SAR) processing is given by the matrix structure and FFT processing. Therefore, it seems almost natural to apply CS for imaging SAR after being applied successfully in image processing. Along with SAR imaging comes a huge amount of data that needs to be processed, usually with 2D-FFT. Managing and especially reducing the increased number of samples resulting from SAR imaging is the driving motivation in [42] to use CS. The reduction of the SAR image processing effort is obtained quite straightforwardly in the sense of CS, i.e. only a random subset of the echo is is sampled and transformed into the Fourier domain for range-Doppler retrieval. In addition, the transformation operator, which is part of the CS processing, is chosen according to the SAR pulse structure. Since the SAR image is generated in two steps to resolve the two dimensions, also different transformation operators need to be applied in order to meet the CS requirements on the reconstruction in both processing steps. During the first step, the DCT is used as a transformation operator, while during the second step a noiselet transformation operator is chosen. The noiselet transformation operator equals a pseudo-binary random (PBR) function. While PBR consists of randomly binary sequences, noiselets are noise-modulated binary sequences. The reconstruction of the raw SAR image data was performed following the BPDN reconstruction method, whereas an interior-point (IP) algorithm was implemented that was constrained by a barrier function during the iteration steps. As a metric for the reconstruction the peak signal-to-noise ratio (PSNR) of conventional SAR processing and CSSAR processing was compared. In direct comparison, the CS method revealed some losses. But considering the fact, that CS aims to reconstruct the signal information, still a sufficient raw data image reconstruction was obtained from a highly reduced number of samples.

Following the same motivation as [42], in [38] the main problem statement within SAR processing, namely the high data rates, was addressed. In this theoretical work, a random noise SAR was simulated. In addition, the relevant metrics regarding CS were stated and computed for CS based SAR imaging. On the transmitter side, narrowband Gaussian pulses instead of chirps are used. On the receiver side a reduced number of samples from the backscatter is recorded replacing Nyquist sampling in fast time, i.e. the range direction. But also in slow time, i.e. the velocity direction, a reduced number of samples is taken, which in practical implementation means to leave out some of the chirps. Based on the reduced set of samples, CS is used to reconstruct the missing samples in slow time and fast time. The reconstruction matrix includes delayed replica from the transmit signal according to classical FFT processing. The authors showed that the matrix fulfills the random isometry property (RIP) and is therefore a feasible matrix for CS processing in this application. The simulation results implied that the approach provides sufficient reconstructions for a SNR of 20 dB while using only 10 % of the samples in both directions.

3.3 Automotive Radar

Although it took not long after the discovery of radar principles, until first experiments were conducted on automotive radar, it still used to be rather a gadget for the luxury segment than a meaningful ADAS function for a long time. According to the overview on automotive radar history given in [55], the first experiments go back until the beginning of the 1970ies using different frequency bands as there were not yet dedicated any frequency bands to automotive radar. Naturally, some of the prototypes applied rather clumsy radar antennas, but still it was possible to show, how beneficial in preventing accidents radar can be. But apparently, for a long time radar was still far from being an application in the mass market.

Meanwhile, an already well-established radar application in the automotive context, are speed measurements that exploit the Doppler shift of a transmitted CW to determine the velocity of a vehicle. Allocating automotive radar frequencies to 77 GHz and in some regions also to 24 GHz, allowed the realization of handy antenna form factors. This resulted not only in easier antenna mounting, but also enabled a cheaper antenna manufacturing, so that radar came closer to become a basic feature for the mass market. In the meantime, a variety of radar functionalities are implemented and used on the streets as part of ADAS functionalities such as adaptive cruise control (ACC), blind spot detection (BSD), lane change assistant or parking slot measurement.

Because of the cheap and comparably simple to implement architecture, automotive radar systems rely on FMCW principles. Since the transmit signal is quite often, if not almost always, implemented as a FMCW chirp, it is also referred to as a pulsed radar, although the receive architecture differs clearly from pulsed radar architectures. Phased array antennas focus the radar beam, which must not be confused with electronic beam steering (EBS) that allows to adjust the beam electronically during operation. Phased arrays feature not adjustable phase shifts in between the antennas but are fix, so that there is no beam adjusting possible, later on. But multiple antennas allow eletronic beam forming (EBF) during signal post processing and approaching imaging radar functionalities with DoA algorithms.

But still, there are many challenges ahead that come together with increasing numbers of radar systems on the streets and new expectations on the functionality and robustness that are induced by the developments towards autonomous vehicles. On the one hand, there are challenges to build handy, low-cost radar systems incorporating more functionalities such as imaging, on the other hand stands the availability of high computational power even in vehicles. This combination paves the way to think of future radar systems detached from the FMCW principle where reasonable and explore benefits of implementing new algorithms such as CS.

3.3.1 Automotive Noise Radar Application

Although noise radars are not necessarily UWB radars, it seems fair to compare their respective state of the art, because both concepts usually cover a broad frequency spectrum and both set therefore similar constraints and requirements to the radar architecture. Since UWB radars are normally limited in range, they are mainly considered for SRR applications in the automotive domain. SRRs are aimed at taking over obstacle and collision detection within the vicinity of the car.

A SRR implementation was analyzed in [79], where UWB pulses were used. The aim was to compare different pulse modulations against each other, since coding or modulating the transmit pulses helps to deal with potential interfering users in the illumination range or by multi-path propagation of other transmitting units. The modulation was performed with pseudo-random codes, namely Gold codes and maximum length feedback shift register (MLFSR) codes. Two different pulse bases are taken into consideration for the modulation, on the one hand a mono-cycle pulse and on the other hand a Gaussian pulse while both of them have a pulse duration of 1 ns. In the following of the paper, the authors compare the performance for the different modulations applied to the different basic pulse shapes. It turned out that the best performance is achieved in the combination of a Gaussian pulse that is modulated with the MLFSR code. The simulation considered the application of an UWB SRR implemented in a vehicular application scenario.

Based on the work in [79], the work was continued in [80] while using the insight that the mono-cycle Gaussian pulse performs best. The extension in this work consists in principle of evaluating different modulations. Here, a maximum range of up to 5 m was tested for the automotive SRR. In comparison to the previous work, a shorter pulse width of 300 ps was implemented. The mono-cycle Gaussian pulses have a magnitude of only 3 V. This time, the modulation of the Gaussian pulses consists of pseudo-random noise (PRN) codes. The receiver was implemented with an oscilloscope that features a bandwidth of 12 GHz and a sampling rate of 40 GS/sec. The oscilloscope is used as an ADC including thresholding. Hence, the correlation of the sampled signal with the reference signal is performed in the digital domain. With this experiment setup the authors obtained only an accuracy of roughly 20 cm at a range of approximately 2 m, which improved at a range of 5 m to 1 cm.

Besides signal processing, at least at some point adequate chips and hardware implementations are necessary to bring new radar concepts to the market. One of the few examples was set in [66], were a chip for automotive 77 GHz radars was brought to silicon. It is not limited to noise or UWB radar but can be also used for FMCW radar signal transmission and acquisition. For UWB radar operation, the chip offers the feature to configure PRN transmit waveforms. The PRN sequences correspond to maximum length sequences (MLS) that are generated by a linear feedback shift registers (LFSR) on the chip. With binary dividers the clock frequency can be set, while the maximum clock frequency is 4.25 GHz. Selecting the maximum clock frequency results in maximum resolution of less than 4 cm. The binary dividers make it possible to implement subsampling approaches such as CS based methods as well. The receiver stage is conceptualized as a cross-correlation receiver. According to the State-of-the-Art, the cross-correlations are performed in the baseband. Therefore, the chip provides a local oscillator (LO) mixing stage, first. In order to find the time delays comprised by the receive signal, after baseband conversion, the receive signal is correlated with the MLS that are implemented as the reference filter bank. For the computational implementation of the CCFs the efficient Fast Hadamard Transform (FHT) approach is used.

3.3.2 Multi-range Radar

With the development towards fully automated vehicles, that demands more robust and highly reliable sensor systems than the ones that are available today, redundancy becomes increasingly interesting despite the higher costs to improve the safety of the autonomous systems. In this context for example data fusion is discussed intensively, but this is beyond of the scope of this work. Apart from including additional and complementary sensors, it is worth to consider to evolve single sensor types themselves in order to obtain more robust sensors in the future. A low-key approach is to extend the functionality of existing sensors in the signal processing chain. Besides bridging the time until future sensor hardware is ready for the streets, it also adds value to existing sensors and provide insights for future sensors as well.

Automotive radar sensors are often categorized according to their application range that implies also different main lobe beam widths. Different maximum ranges allow different opening angles and range resolutions, which specifies suitable radar applications. While LRR systems are ideal for ACC, where a narrow beamwidth is required, MRR and SRR systems usually have wide opening angles. For the latter, targets within the vicinity of a vehicle are separated by DoA estimation algorithms such as in [42; 101]. LRRs feature narrow beamwidths for two reasons. The first reason is to increase the gain and therefore the transmit power in the main lobe direction in order to improve the illumination of targets that are located ahead. Regarding the high free space attenuation at the carrier frequency at 77 GHz, focusing the beam mitigates the effort to reach the intended maximum ranges of an LRR.

The second reason to design the LRR beamwidth to be narrow, is caused by the application itself. Once a vehicle that is moving ahead is detected, the ego vehicle should lock that distance. Consequently, it is sufficient to only track the speed and distance of the vehicle in front making a DoA estimation obsolete. But after leaving the motorway, where ACC is a useful tool, other challenges than checking the speed and distance of the vehicle arise. Actually, in urban or rural landscapes ACC systems provide low to no benefit at all. Instead, the target location in range and azimuth location becomes essential in order to locate pedestrians or bicycles at intersections. At this point, radar systems that are able to cover several distances including their implied beampattern come into play. After entering urban environments and leaving the motorway, it is advantageous to switch radar sensors into another operating mode instead of mounting separate radar sensors for each functionality. In the following, approaches that cover this problem statement are presented.

To realize a radar system that is suitable for more than one range it takes adjustments in two domains, the antenna hardware and the signal design. On the hardware side the beampattern of the antenna array needs to be adjusted to meet the illumination requirement of the respective range. The toggling between two ranges and their respective antenna beams was realized via switching in [37; 92]. Except for the lag in time, mechanical or electronic switching between two antenna designs does not introduce any additional drawbacks regarding range or azimuth resolution, when compared to systems that are dedicated to a single range.

Both antenna designs are conceptualized for LRR and MRR systems, whereas the beam for the mid range is divided into two beams that feature main lobes of 30° each. In [37] the physical antenna elements for MRR and LRR are placed next to each other, thus resulting in two separate neighboring antenna apertures. During MRR operation the azimuth direction is resolved by digital beamforming (DBF). Slomian realized a different implementation in [92] that preserves the location of the antenna aperture. Instead of two neighbor structures, the different antenna arrays were stacked in different dielectric layers. Both antenna designs were realized as microstrip antenna arrays for 77 GHz.

Apart from the adjustment of the scene illumination by adequate antennas, the signal processing also needs to be adapted to different ranges in order to obtain the best granularity in terms of range resolution. In radar technology this can be reached by adapting the chirp bandwidth or pulse length, depending on the implemented radar system. A solution that is applied on the receiver side is propose in [63].

Table 3.1 – Comparison to the State of the art

reference	[37]	[83]	[64]	[92]	[96]	[50]
Multiple range resolutions	–	✓	✓	–	✓	–
Multiple opening angles	✓	–	–	✓	–	–
Range adjusted beam pattern	✓	–	–	✓	–	–
Multiple target detection	–	✓	✓	–	–	✓
Multi path propagation	–	–	✓	–	–	✓
Angle separation	–	–	–	–	✓	✓

There, different sharpening filters are designed that are tailored to different range gates. At the receiver side the signal is applied to the parallel sharpening filters. For the transmit pulse, pulse compression parameters are implemented that are fitted to the maximum intended range and the aimed maximum resolution. The received pulse is focused first with autocorrelation function (ACF) and then fitted with least error sharping filters, thus compressing the signal to the desired pulse width. Another approach that actually gained a high popularity in automotive radar, was pursued in [64]. Multi-ranging is imprinted in the transmit pulses. The transmit signal is composed of several pulses, that are parametrized in bandwidth and ramp duration and ramp distance in order to include different ranges and implied resolution constraints. From neighboring range cells the clutter is estimated, thus increasing the robustness and reliability of multi-range signal processing.

3.3.3 Interference in automotive radar

Interference occurs in several aspects in automotive radar systems and its impact is significant. Several interfering radar signals that overlap in frequency can cause a high power level on the receiver circuitry that drives the receiver in its non-linear operating mode after saturation. This effect cannot be fulfilled by a simple filter. In addition, interfering signals can result in frequency shifts, which is especially critical for FMCW radar systems. Because FMCW based radar architectures rely on the comparable simple signal acquisition, that compares the transmit and receive signal, which results in the low-frequent beat signal, interference induced frequency shifts will not be recognized. As shown in [30], two interfering FMCW signals result in additional spikes in the baseband signal. This leads either to the detection of ghost targets or actually existent targets are blurred or obscured.

A first source for interference is the RF front-end by itself. Since the transmit and receive antennas are usually co-located, crosstalk between the antennas needs to be considered as a pitfall immanent to the circuit design. In [9] it was suggested to compensate the crosstalk between transmit and receive antennas through spectrum analysis. In a scenario without any targets, the spectral components of the beat signal are evaluated and memorized. These measurements are used as a reference to generate a threshold profile that is applicable to the range profile during later measurements. Since the antennas are fixed, once the RF front-end was designed, the calibration design is feasible, but it cannot prevent any transistors that are part of the receiver circuitry to be driven into saturation. Naturally, calibration cannot be applied to crosstalk from other radar systems in a scenario that is as dynamic as the automotive one.

Consequently, mutual interference between several radar systems remains a critical aspect in automotive radar systems. As the penetration rate of radar systems on the streets is still at a manageable level, turning off the radar during a detected interference remains a feasible practice for now. But it is not a valid longterm solution, since the number of radar systems and therefore interfering systems on the roads will continue to increase significantly. Furthermore, highly automated or autonomous vehicles will become even more dependent on radar sensors as ADAS functionalities will take over more and more tasks in the future.

The interference topic is discussed in [48] regarding collision detection. Automotive radar systems featuring a center frequency of 24 GHz are applied in the experiment. The transmit signals were designed to be PRN sequences. Thus, the mutual interference is lowered significantly, when different PRN sequences are used for each transmitting system. But also, the interference between systems that use the same PRN sequences remains low, which proofs the suitability of applying PRN sequences instead of FMCW signals in the automotive use case. Nevertheless, it might be difficult to introduce PRN radar signals, while FMCW radar systems are still on the road. The impact of the PRN sequences on FMCW can be imagined close to the impact of orthogonal frequency division multiplexing (OFDM) radar systems.

Using only OFDM radar systems, the role of crosstalk could be diminished significantly as is understandable by the orthogonal frequency signal design. But considering the scenario, where OFDM and FMCW are co-existing on the road, the crosstalk between OFDM radar and FMCW based radar systems becomes an issue for the latter, as shown in [69]. On the one hand, OFDM increases the noise floor, which decreases the SNR. With a lower SNR, the minimum receive power needs to increased to ensure a reliable target detection. Otherwise, low-key targets could get lost in the overall noise level. On the other hand, OFDM introduces spikes to the FMCW radar, thus being a throwback regarding the mitigation of interference.

In order to identify interferences in OFDM systems that also result only from other OFDM radar systems, [69] proposed to sort first the spectral components according to their weight and to remove afterwards the strongest components, which are assumed to be clearly a result from interference. Under the assumption that interferences hold the dominant spectral components, the suggested method can be projected to FMCW based radar systems as well. The impact of noise modulated pulses on FMCW was analyzed in [85], whereas the focus is set on the co-existence between communication and radar systems.

3.3.4 Summary and research interest

New applications of radar systems in the automotive context require new concepts and methodologies in order to meet their requirements. These new requirements can be fulfilled by making use of CS methods, which are applicable after computational capacities have been increased dramatically in the past decades. This development not only intesified research on CS, but also research on noise radar systems. So far, noise radar systems were not in the focus of automotive radar system development. The author intends to show the potential of noise radar systems, especially for future applications that come along with the development towards autonomuous systems. The thesis at hand uses the signal acquisition enhancing methods of CS and applies them on an accordingly modified noise radar system for future automotive radar system applications.

4 Compressive Sensing based Noise Radar

In contrast to image perception, which is very close to human perception and therefore easy to understand and interpret as a human being, radar requires a slightly different approach. Radar basically reports all reflecting points within the illuminated area. But a peak amplitude can also result from additive superposition of multi-path propagation. In addition, a high reflectivity of a comparable small object, clutter or interference can impede the interpretation of the received backscatter. During signal processing it is the aim to resolve ambiguities in range, azimuth and Doppler, if possible. If it is possible or not, is influenced by the design of the transmit signal itself. In summary, radar captures anything, but it takes some adequate smart signal processing to extract the information that should be revealed.

As the requirements to detect various information lead to very diverse and some times even contradictory requirements, radar systems are usually dedicated to particular applications, e.g. range-Doppler measurement, near-range separation of objects, clutter detection or weather monitoring. The signal parameters, which define the radar application, comprise a carrier frequency, which is either defined by regulations or practical considerations such as desired maximum range and the according free space attenuation. For the latter, timing aspects such as ramp duration and pulse intervals are crucial, too. Not only the carrier frequency, but also bandwidth and antenna configuration play an important role regarding resolution and separability.

After signal acquisition and initial signal processing, the output still needs to be interpreted. Mainly here, in the data processing part, it is useful and even necessary, to dedicate the radar to certain applications. That is to ensure that correct objects are identified, whereas it is useful to know what typical objects are and what their typical characteristics are. In automotive applications, there are typical velocities for cars or pedestrians that differ significantly from common applications that are often found in the field of airborne systems, for example. Also, in urban scenarios other dimensions can be expected than in applications that are dedicated to earth observation.

This diversity is reflected in a huge variety of applications of CS to radar in order to improve or even enhance its functionality. It is sensible to split a radar system into several parts in order to describe and address manifold CS applications such as in Figure 4.1. The three main categories in terms of types of CS application to a radar system are stated here as RF frontend, low level and high level signal

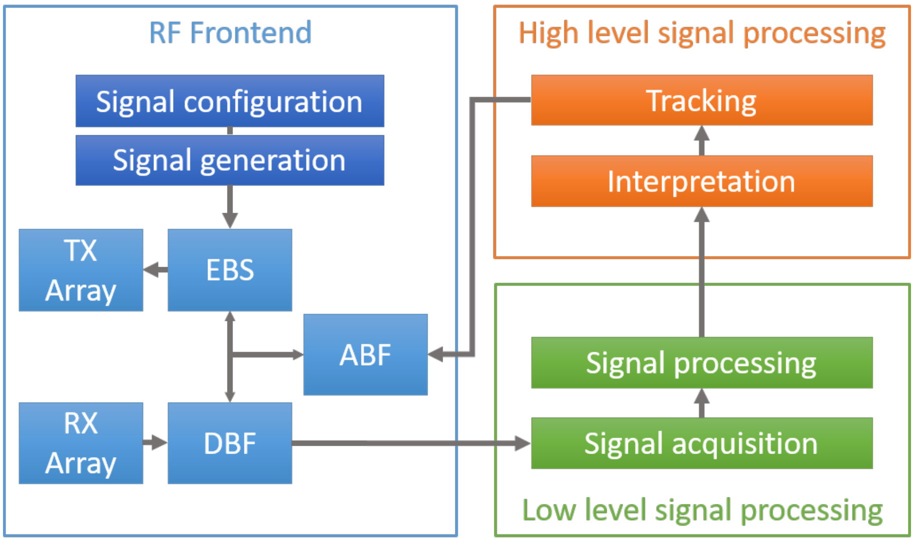

Figure 4.1 – Radar function blocks for CS applications

processing. Integrating CS methods addresses different challenges in each of the three categories. Main challenges in radar applications comprise range and resolution as well as illumination field. In addition, separability of different objects in azimuth, range and also elevation direction belongs to the inevitable limitations along with interference and sampling. The radar RF frontend includes all physical and analog RF components such as transmit and receive antennas but also their application and signal generation. This first category is important from the point of view of CS to generate the required transmit waveforms according to the selected CS implementation. But also the antenna configuration in the physical as well as the application sense are important set screws for the implementation of CS methods. Antenna arrays cover geometrical implementations such as linear, which is the most common one in automotive radar so far, planar, circular or triangular alignment.

They can be designed as phased arrays with fixed or adjustable phase shifts between individual antenna arrays. Phase shifts in between antenna arrays allow to steer the beam of the complete antenna in specified directions. In case of fix phase shifts the beam steering is performed only once and adjusts the radar to cover a certain area, either in horizontal or in range direction. The latter is helpful to reach a particular range, e.g. by narrowing down the beam in order to obtain a higher gain in the main lobe direction and hence an increased range. The other way round, a wide opening angle qualifies the radar to resolve objects that are closer to the radar platform and, depending on the antenna configuration, obtain the azimuth position of an object. With a wider beam the antenna gain decreases in main lobe direction and accordingly results in a limitation in range direction that needs therefore to be taken into account. The antenna platform is interesting for CS methods regarding the realization of patterns that can be used as physical measurement matrices. By switching the activated antennas, the directivity can be adjusted to illuminate different range and azimuth or even elevation areas. Hence, by combining different antenna setups, a diversity in range and azimuth direction can be obtained that enables the application of CS signal acquisition and reconstruction. Accordingly, especially on the receiver side this can be used to enhance DBF using CS for obtaining super-resolution in azimuth direction.

Designing phased arrays and implementing DBF belongs to the category of low level signal processing, which is depicted on the bottom right corner of Figure 4.1 including functional radar blocks. In this category, everything related to signal acquisition and processing is included. For signal acquisition it is not only possible to implement direct sampling, but also a cross-correlation receiver instead, which is using either filter banks or a reference signal such as the transmit signal. The latter is especially suitable for continuous waveforms, while cross-correlation approaches fit to pulse-based radar systems. Direct sampling is rarely applied because usually the required sampling rates are subject to expensive ADCs featuring high sampling rates. While correlating the receive signal with the transmit signal is a favorable way of dealing with continuous transmit waveforms, it is not applicable for pulsed waveforms, which rather work with a correlation receiver. Correlation receivers require a high amount of filters, specifically at least one filter per range gate. Same applies for additional dimensions that should be resolved, such as azimuth and velocity dimension. The required amount of filters is a major drawback for correlation receivers, not only regarding implementation effort, but also regarding acquisition time. That is why correlation receivers are rather used for short distances such as tank level measurements or when it is sufficient to obtain a coarse range estimation. But, with CS the situation for cross-correlation receivers can be understood as a problem statement tackling signal reconstruction from incomplete measurements. Hence, CS can be applied for reducing a full correlation setup to a subspace filter bank and to reconstruct the originally received signal with an adequate matrix. When considering direct FFT conversion at the analog stage, also here a subspace of Fourier coefficients can be applied instead of the full set. CS is then applied to reconstruct the remaining relevant Fourier coefficients. Acquiring different spectral components can be also implemented by using non-uniform sampling. Instead of sampling each and every single value according to the Nyquist frequency such as in direct sampling, samples in varying time distances are acquired, which is equivalent to the usage of different sampling frequencies. This approach is especially feasible for continuous signals that comprise a high bandwidth. The approach of non-uniform sampling allows to mitigate the requirements regarding high-sampling-rate ADCs, although it does not avoid it completely. Apart from non-uniform sampling, it is also possible to apply random measurement sequences on the signal and therefore transform the signal into another domain.

The signal processing stage comprises the possibility for pulse-Doppler processing, which is widely used in radar systems that are applying modulated pulses such as chirps. Additionally, in this block direction of arrival (DoA) estimators are implemented that process signals obtained from EBF in order to obtain a spatial resolution in azimuth direction. DoA estimation can be performed using CS methods either on single or multiple snapshots. Depending on the realized signal acquisition concept, in this block the CS signal reconstruction is implemented, which comprises either 2D- or 3D-FFT computation, CS reconstruction algorithms and other low-level processing such as constant false alarm rate (CFAR) detectors and peak detection. It belongs to the third category on the upper right corner of Figure 4.1 and is described as high level signal processing, because it operates on a higher level of abstraction, such as target and object clustering, categorizing and tracking. Sometimes, it is also referred to as data processing in order to point out the increased distance from the raw radar signal.

Extracted peaks that are recognized as targets are clustered to objects, which are classified and tracked. In this stage, the context of the radar measurements becomes crucial to obtain meaningful results. CS is applicable here to support classical methods and supplement additional information for example from super-resolution techniques or reduce false alarms by merging the results from classical signal processing and CS processing methods. As a result from high level signal processing, adaptive beamforming (ABF) can be adjusted in such a way, that either the illumination area is cut onto the region, where objects have been recognized and tracked or CS illumination patterns are realized. Not all processing interfaces within the radar signal processing chain are equally suitable for CS methods as the trade-off between additional effort and benefits needs to be kept in mind. Especially in the cost-sensitive automotive segment, the silicon design should be only modified if a significant improvement can be expected that finally, in the best case, even lowers the overall costs.

This chapter is organized as follows. First, a study is presented on how to apply CS methods to different existing radar architectures. Then, simulation results are evaluated, before a CS noise radar is chosen for further analysis. The signal and receiver models are introduced as well as according CS metrics and analysis. Finally, different approaches are compared against each other with a proof-of-concept simulation until results from a demonstrator, which is based on a validated emulation, lead to final conclusions.

4.1 Compressive Sensing for Automotive Radar

From the huge variety of possibilities how to address different issues of radar systems using CS methods, some approaches were analyzed in more depth by the author of this thesis. In the following, the analyzed approaches that qualify for automotive applications are addressed. The criteria used to select approaches to be analyzed, were to increase range or azimuth resolution and to improve the robustness towards noise and interference. Overall four methods are introduced and described from mathematical and simulation point of view, whereas one method that qualified best and looked most promising is discussed and demonstrated in detail.

4.1.1 Pulsed Radar - RMPI and SAR

Pulsed radar systems have the benefit of being robust towards interference. Although the required Nyquist frequency for sampling can be lowered e.g. by pulse compression, direct sampling remains an issue. Sampling pulses can be imagined as trying to make a perfect camera snapshot of an athlete jumping into a pool. Instead of hitting the camera trigger once and almost certainly missing the perfect time to do so, a video can project the scenario into a sequence that can be evaluated later on and allows to find the ideal point in time. That is in principle the concept behind RMPI, that works for different technologies, first of all camera such as in [11; 76]. The RMPI makes use of the fact that the signal acquisition in CS consists of projecting the signal into a different domain.

Therefore, instead of directly sampling a narrow pulse, the pulse is convoluted with several projection or measurement signals, which corresponds in this case to spreading the information of the signal, i.e. the peak location, across several dense signals, i.e. the measurement signals here. Hence the observations, which result from integrating the signals that are obtained by the projection process, contain partially the original information in terms of varying energy levels. The crucial part here is to generate the random measurement sequences in a reproducible way so that on the one hand the sequences qualify to spread the information sufficiently and on the other hand the requirements on memory capability does not explode in order to store the measurement matrices for recovery. In [89], the author proposed to generate the measurement matrices by hardware, i.e. by using RF effects of microstrip lines.

As such, the measurement matrix qualifies to spread the signal sufficiently on the one hand and on the other hand, the sequences that are generated depend only on the input signal, so that it can be re-generated for reconstruction while only saving the input signal, e.g. a step function. Of course, the RF hardware effort is initially high, as the bulk is realized here, contradicting the trend towards SDR. Nevertheless, using RMPI and even implementing it in silicon, although not by using microstrip lines, was proved to be feasible in [51], where it was used as an analog-to-information (A2I) converter.

Whereas the principle of using RMPI for pulse acquisition and ToF reconstruction was discussed by the author in [88], it is here carried on for the acquisition of radar pulses, that are implemented as chirps. The natural domain for sparsity of a chirp is the time domain. Therefore the RMPI can be designed close to the camera implementation in [11], which uses among others the mathematical foundations that were laid out in [75]. Direct sampling is replaced by several parallel analog RF mixers

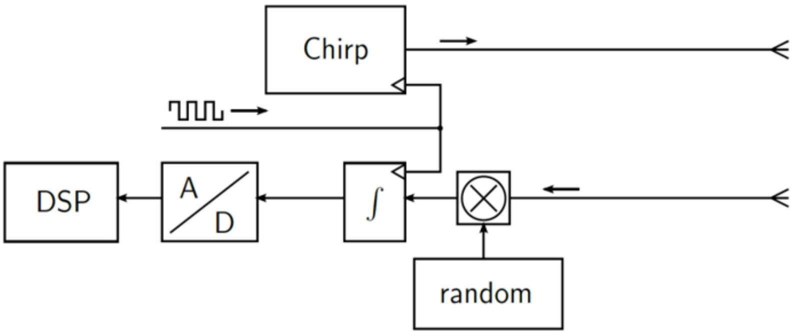

Figure 4.2 – Block diagram of RMPI radar hardware architecture

in the receive path that modulate the received signal with random measurement signals. As suggested by the author in [88; 89], the pseudo-random measurement signals can be obtained from either analog or digital generator functions that avoid the necessity to store the measurement matrix. The schematic block diagram is depicted in Figure 4.2.

Still operating on RF hardware, the signals projected in parallel by the microstrip lines, are integrated during the maximum roundtrip time, which also defines the PRI of the chirp transmission cycle. Given enough initial power of the transmitted pulse, the PRI defines the maximum target distance for unambiguous range detection. In practical implementations, attenuation resulting from free space propagation limits the range, too, especially for pulses. The transmit signal consists of a short linear chirp that is delayed by τ_d at the receiver stage. The time shift τ_d comprises the propagation of the transmit signal and the velocity induced Doppler shift according to (4.1).

$$\tau_d = \frac{2 \cdot (r - v_r \cdot t)}{c_0} \tag{4.1}$$

Hence, the underlying model of the received signal is stated such as in (4.2).

$$s_r(t) = \begin{cases} \mathrm{e}^{j\pi\alpha\cdot(t-\tau_d-t_s/2)^2}, & \text{if } |t-\tau_d-t_s/2| \leqslant t_s \\ 0, & \text{otherwise} \end{cases} \tag{4.2}$$

The chirp rate α is the quotient from bandwidth over chirp duration t_s. During the measurement process, random signals are generated and used for convolution with the received signal. The random signals, that result from a random process with standard normal distribution, state the measurement and reconstruction matrix $A \in \mathbb{C}^{M\times N}$. Accordingly, the resulting observation b is used to state the reconstruction objective in (4.3).

$$\min ||s_r||_1 \ s.t. \ \min ||As_r - b||_1 \leqslant \varepsilon \tag{4.3}$$

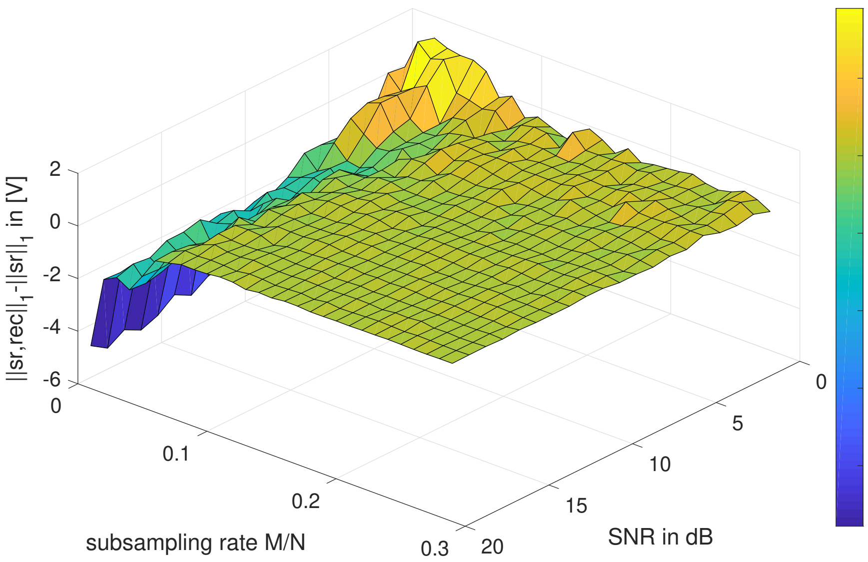

Figure 4.3 – Reconstruction accuracy for RMPI receiver over subsampling rate and SNR

For a proof-of-concept simulation, the aim was to demonstrate the theoretical feasibility of the approach for a reliable reconstruction in the aforementioned pulsed radar system. A reconstruction result was considered to be successful, if the correct time bin was obtained, while the absolute value of the peak amplitude was treated as secondary. The terminology time bin refers to the multiples k, i.e. time steps, of the sampling time interval Δt that results from the assumed sampling frequency.

In these experimental simulations that are subject to purely theoretical contemplation, a bandwidth of 0.5 GHz was applied with the subsequent range resolution of $r_{res} = 0.3\,\mathrm{m}$. Furthermore, the sampling frequency was set to $f_s = 1.1 \cdot B$ and the maximum distance in range to 300 m. The chirp duration was set to 10 ns within the simulation. Results of the simulation show that only 10 % of the measurements that are needed in Nyquist designs are sufficient for a perfect reconstruction result in time at an SNR of 3 dB. For reconstruction, an IP algorithm was used for the BP approach such as described in Appendix 2.4 and a greedy algorithm, namely an implementation of the OMP according to [99], see Appendix 2.1. In Figure 4.3 the dependency of the reconstruction accuracy is plotted for subsampling rates $M/N = 0.01$ to 0.29 and SNRs from 1 dB to 20 dB while using the OMP algorithm. The plotted measure for reconstruction accuracy is the difference between the ℓ_1-norm of the reconstructed signal and the true receive signal. In practical implementations with wideband signals, subsampling still can result in a high implementation effort, given that all correlation stages need to be implemented in parallel RF hardware channels. Therefore, in order to mitigate hardware complexity, the measurements

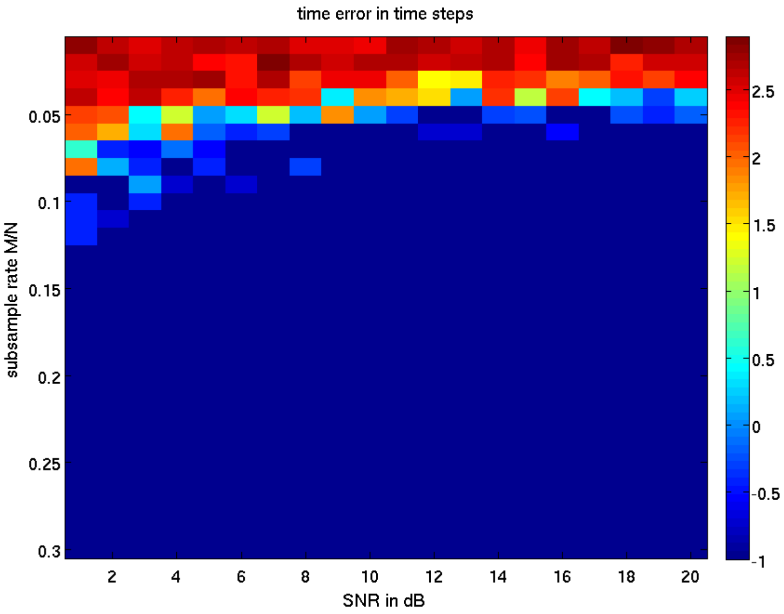

Figure 4.4 – RMPI based radar: time error

should be split to several measurement cycles, e.g. five channels on hardware. This implementation approach requires well-designed pseudo-random signal generators to obtain reproducible measurement sequences but also reconstruction signals. Due to short pulses and especially limited automotive distances, a measurement and reconstruction cycle is still expected to remain reasonably short with a manageable run time, if a greedy algorithm is used. As a benchmark, the measurement cycles of automotive radar sensors available on the market are taken into account, which normally range between 60 ms and 80 ms.

To understand the impact of the sub-sampling factor and the SNR on reconstruction accuracy in time, in Figure 4.4 the time bin deviation between the reconstructed and true receive signal are plotted. Accordingly, the amplitude deviation is plotted in Figure 4.5. Other than the error in time, which is here a discrete value due to the correlation filters, the amplitude error is an analog value, as it is not reconstructed based on correlation filters. Apart from that, the amplitude error shows the same tendency such as the errors in time bins. That means, that for very low sub-sampling or high SNR the error becomes larger.

The advantages of using a RMPI receiver and a pulsed radar in automotive applications are in the low vulnerability towards interference but also the good performance in low SNR channels allowing to keep the transmit power comparably low for a pulsed system. Furthermore, the output of the RMPI receiver is the reconstructed receive signal and not a frequency shift such as in FMCW receivers. Thus, a deeper understanding of the illuminated scenery is possible, e.g. to identify

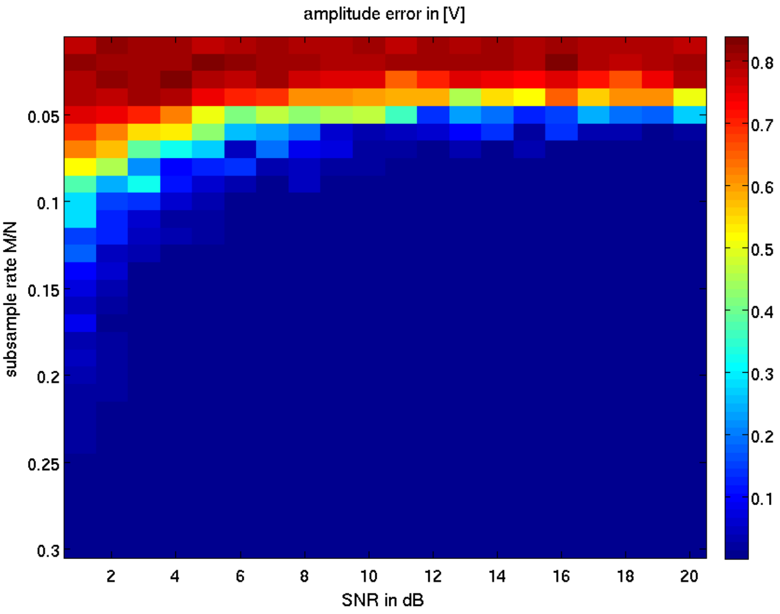

Figure 4.5 – RMPI based radar: amplitude error

clutter characteristics. A slight drawback originates from the importance of the sparsity. As depicted in Figure 4.6 from the author's work on time-of-flight (ToF) measurements using a RMPI implementation, see [88], the reconstruction accuracy depends on whether the signal sparsity is anticipated in the correct magnitude in order to take a sufficient amount of M measurements. The results are transferable to the proposed RMPI radar receiver regqarding reconstruction accuracy for different sub-sampling rates. Besides measurement signals provided by a standard normal random process, uniformly distributed ±1 sequences Bernoulli sequences are used such as depicted in Figure 4.6. Besides the aforementioned Bernoulli sequences, any other random process is aplicable [76] as well, except for a $\{0, 1\}$ sequence, because that would lead to an unintentional reduction in information. After implementing the measurement process on hardware, repeated measurements allow to adjust to an increased sparsity. In order to be able to perform a feasible amount of measurements, tailoring the radar system to its typical applications is crucial.

To some readers the signal model in (4.2) might look familiar since it is a typical notation for chirps, such as in SAR applications. Indeed, using the above presented RMPI receiver approach for range as well as the azimuth direction, SAR images could be reconstructed sufficiently in magnitude, although the phase was lost during range and azimuth computation. The raw SAR data in Figure 4.8 show how the original SAR image in Figure 4.7 is reconstructed after using the RMPI approach with OMP reconstruction on both measurement directions, i.e. range and azimuth. It should be noted that the parameters used during the SAR and CS based SAR simulation

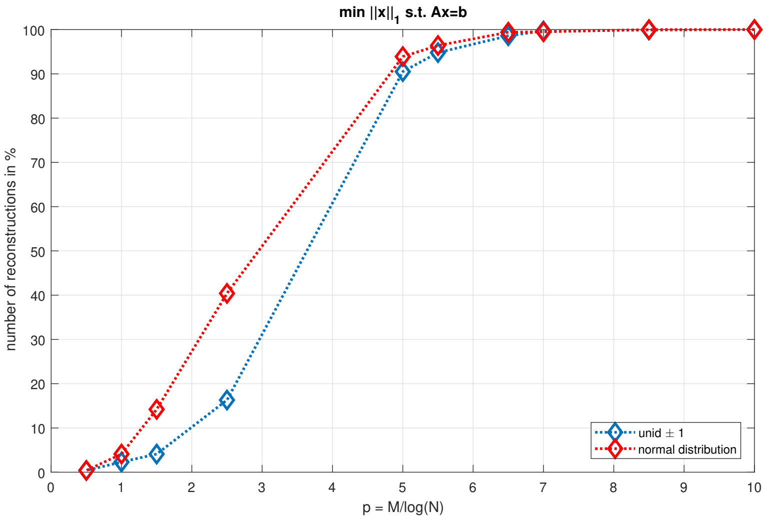

Figure 4.6 – Reconstruction dependency in RMPI receiver systems on sparsity-dependent number of measurements

and reconstruction are obtained from a typical airborne SAR system, which is why the range and azimuth dimensions are much higher than required in any automotive applications.

Expectedly, the result shows that artifacts are obtained by a straightforward measurement reduction for RMPI and CS based SAR signal acquisition. In order to analyze the effect of these artifacts on the SAR image, the RMPI was used separately for range and azimuth signal acquisition, whereas practical implications were neglected. The comparison between the reconstruction results in Figure 4.9 leads to the initial conclusion, that the performance in SAR image reconstruction is more suitable for azimuth direction than range direction, although the location of the maximum peak could be reconstructed in all cases. Only the phase cannot be reconstructed in all implementations. For SAR the RMPI with CS reconstruction is rather promising for increasing the resolution in azimuth direction, that is physically limited by the synthetic aperture as compared with basically drop range measurements as thus is reducing the SNR, which is a crucial factor in radar measurements. Typical SAR applications suffer more from reducing measurements in range direction than CS could level out, when applied such as proposed. But in azimuth direction, it seems to be a promising approach for super-resolution.

4.1.2 Phased Array

Radar antennas are designed with different specifications regarding detection and spatial diversity, which depend on the target specification. Gain and spatial illumination can be adjusted on hardware by connecting single antenna elements to antenna

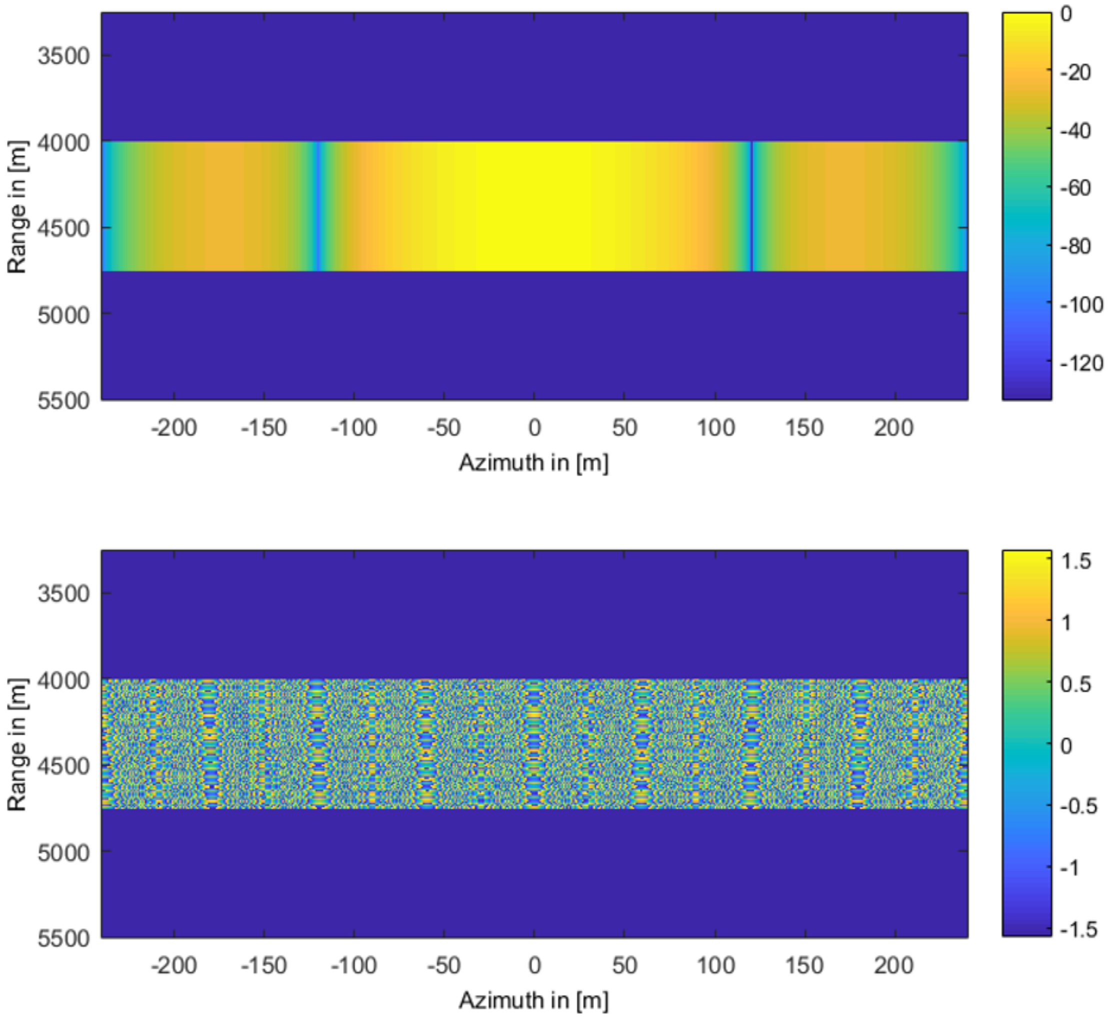

Figure 4.7 – Original raw SAR data

arrays. To obtain a linear array, the elements are connected in series and aligned linearly sharing one common antenna feed. Connecting several antenna elements or arrays increases the overall antenna gain in main lobe direction, while the beamwidth of the main lobe is reduced. Besides defining the main lobe, it also shapes the side lobes of the antenna aperture. Spatial diversity is obtained by placing several antennas with individual feeds on at least one side, either the transmission or the receiver side. On the transmitter side, this allows to control signal transmission for each antenna, while on the receiver side individual receive signals can be acquired for each receive antenna. By sampling all receive antennas individually, different spatial propagation channels can be observed within the receive signals. To sum up, operating radar systems with several connected antennas increases the maximum

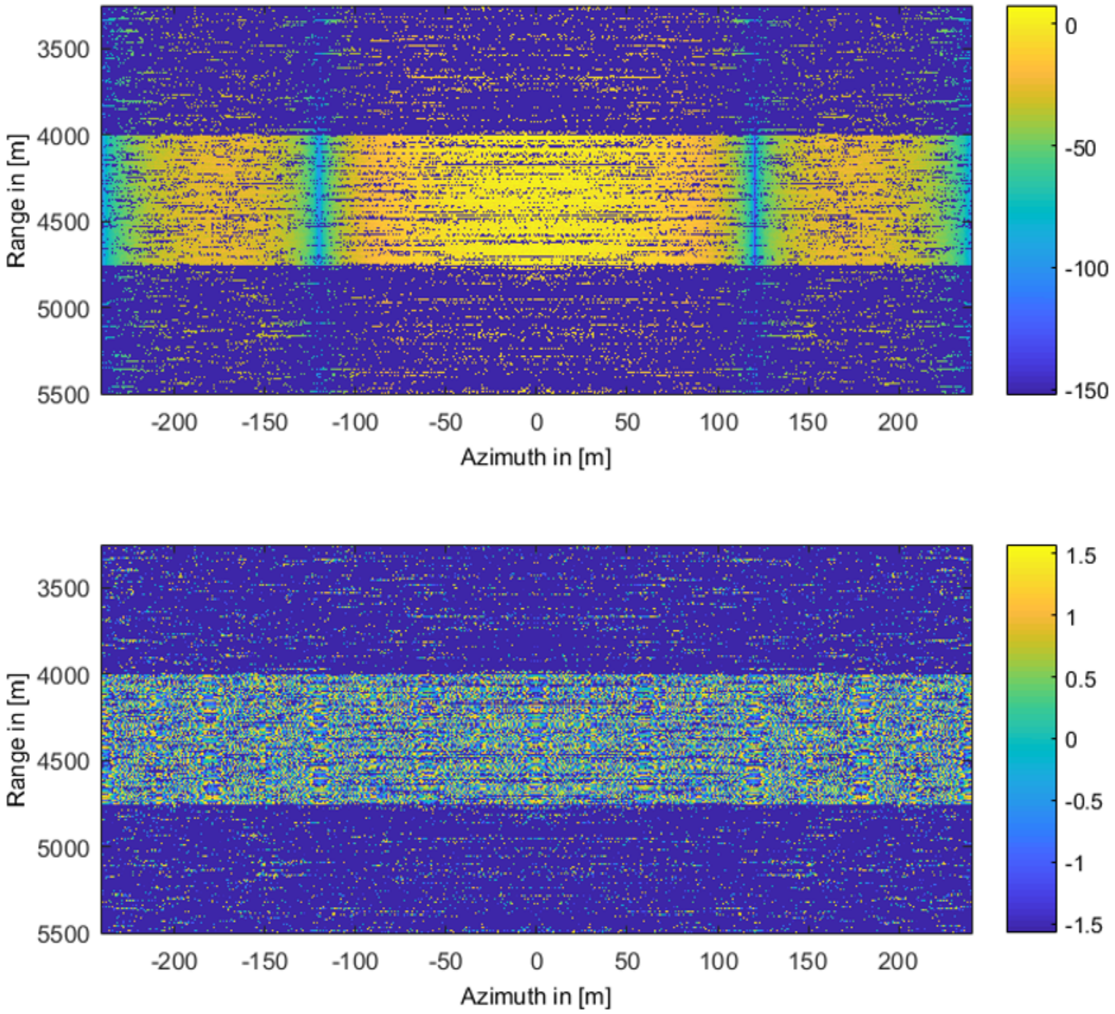

Figure 4.8 – Reconstructed raw SAR data

range a radar system can illuminate from physical point of view, while deploying several individual antennas enables to benefit from spatial diversity. The benefits can either consist of an increased chance to observe non-distorted backscatter or of resolving spatial information. Accordingly, alternating these operation modes makes it even possible to overlay receive signals obtained from these measurements and accordingly enhance the radar performance.

For the amplitude of the receive signal not only the LOS and eventually non-line-of-sight (NLOS) propagation path are pivotal, but also the angle-of-arrival (AoA) at each antenna. Combining the aperture of the individual antenna elements results in the overall antenna directivity and hence angle-dependent antenna sensitivity. Essential for the overall aperture are the number of single antenna elements as well

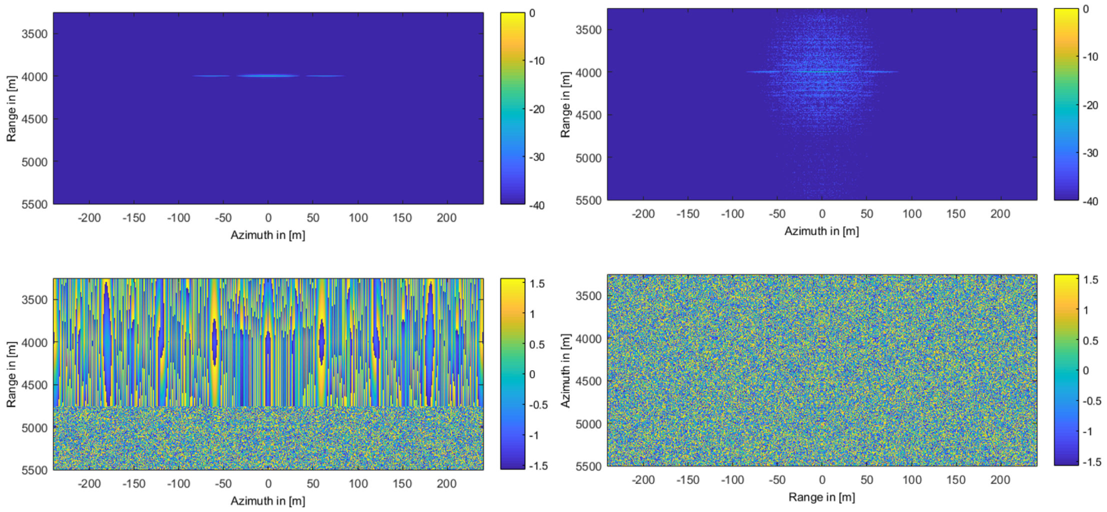

(a) original range (b) reconstructed range

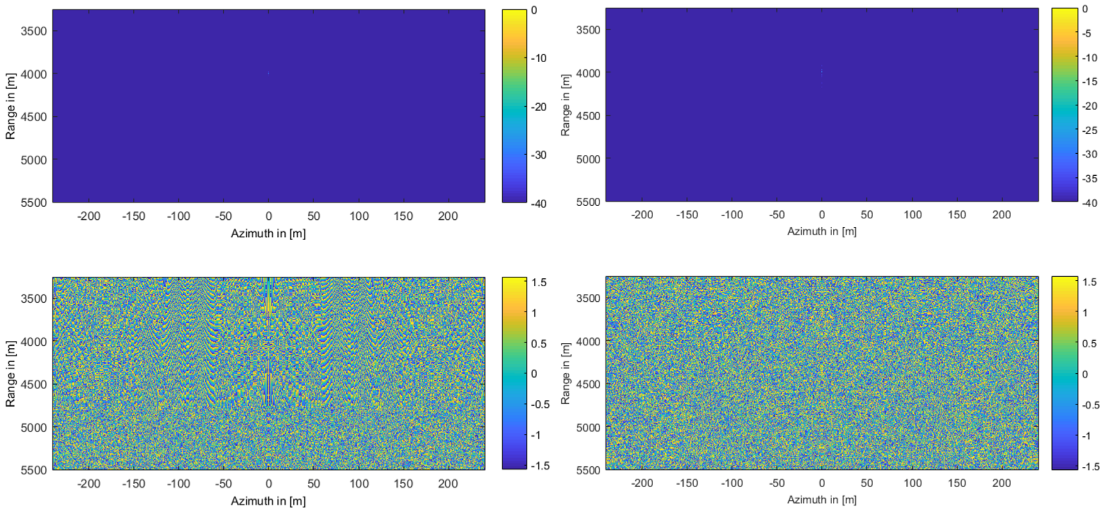

(c) original azimuth (d) reconstructed azimuth

Figure 4.9 – SAR images for Figure 4.9 a original and Figure 4.9 b reconstructed range and Figure 4.9 c and Figure 4.9 d azimuth processing

as the distance in between the elements. For a spacing greater than $\lambda/2$ between two neighbor elements, grating lobes, also known as side lobes, appear in the resulting antenna pattern. Grating lobes reduce the antenna gain in the main lobe direction, which is in many non-urban ADAS functions the main direction of interest. Hence, antenna arrays for non-urban long range applications should be designed in such a way, that grating lobes are avoided, where possible. Contrasting to this approach, spatial diversity, which is also obtained from grating lobes, can be used as additional information for separating objects in azimuth direction, making grating lobes actually useful.

Phased array antennas are arranged in such a way that the antenna signals are phase-shifted to each other. In order to understand how antenna arrays can be used for CS techniques, some fundamental equations are recalled in the following. The equations below not only describe phased arrays, but are also fundamental for CS equations. In an antenna array comprising N antennas, the i-th receive signal is the result of the superposition of the signals that arrive at each antenna. Neglecting for now the superposition of the wavefronts in LOS as well as NLOS propagation paths, the geometry of the individual antennas within the array induce phase shifts in azimuth and elevation direction, thus resulting from the AoA φ in azimuth and ϑ in elevation direction. In general cases, where the placement of the antenna elements either cannot be chosen arbitrarily or in systems with a higher complexity, introducing the wave vector $k = (k_x, k_y, k_z)$ such as in [72], is helpful for simplifying the characteristic equations. Hence, the wave vector is stated in (4.4), while $\{x, y, z\}$ remain the axes in a Cartesian coordinate system.

$$k_x = \frac{2\pi}{\lambda} \cdot \sin(\vartheta)\cos(\varphi) \tag{4.4}$$

$$k_y = \frac{2\pi}{\lambda} \cdot \sin(\vartheta)\sin(\varphi) \tag{4.5}$$

$$k_z = \frac{2\pi}{\lambda} \cdot \cos(\vartheta) \tag{4.6}$$

The resulting receive characteristic at each individual element equals the sum of the phase shifts as stated in 4.7 [72].

$$y_i = \mathrm{e}^{-jk_x x_i}\mathrm{e}^{-jk_y y_i}\mathrm{e}^{-jk_z z_i} \tag{4.7}$$

For a linear aligned phased array that is arranged in a Cartesian system in such a way that $(x, y) = 0$, (4.7) can be simplified to (4.8).

$$y_i = \mathrm{e}^{-jk_z z_i} \tag{4.8}$$

If the antenna signals are not considered individually, the total received signal is computed as the sum over all N antenna array elements (4.9).

$$y = \sum_{i=1}^{N} \mathrm{e}^{-jk_z z_i} \tag{4.9}$$

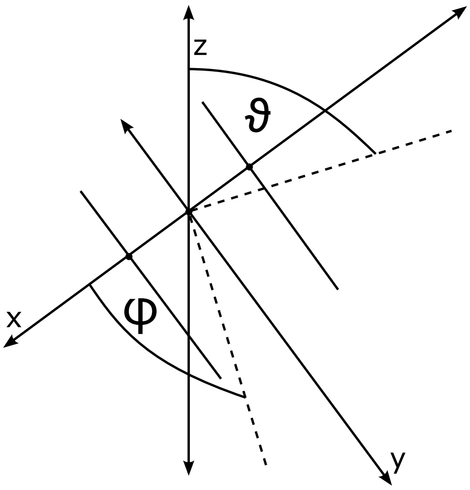

Figure 4.10 – Linear phased array antenna with three elements in Cartesian coordinates

Assuming a spacing of $\lambda/2$, which uncorrelates the antenna beams in the sense, that individual main lobes will exist, and centering the odd number of antenna elements around zero, (4.9) can be stated in an even more handy way such as in (4.10).

$$y = \sum_{m=\lfloor N/2 \rfloor}^{\lfloor N/2 \rfloor} \mathrm{e}^{-jm\pi\cos(\vartheta)}. \tag{4.10}$$

In Figure 4.10 the placement of three antenna elements is sketched in an Cartesian coordinate system, whereas the elements are arranged corresponding to (4.10). The single antenna elements are indicated as lines that cross the x-axis, which goes along with the previously stated assumption, that the elements of the linear array show no displacement in y- or z-direction. The dotted lines indicate two separate incident rays, whereas one ray illustrates the incident angle φ in azimuth direction and the other one the incident angle ϑ in elevation direction.

After manufacturing the antenna frontend, the spacing between the antenna elements is a fixed physical constraint that cannot be adjusted, although the dependency from $\lambda/2$, or multiples of it, suggests this necessity for signals with a broader spectrum. Antennas are therefore often designed for the center frequency of the target application and the slightly different antenna patterns that result from the application of deviating frequencies are accepted. For the matter of illustrating the impact that can be expected for automotive antennas, in an example the spacing is designed initially for the wavelength at the carrier frequency f_c equal to 78 GHz. The according $\lambda/2$-spacing between two antennas is therefore 1.9 mm. The blue line in Figure 4.11 depicts the resulting antenna pattern for the carrier frequency of 78 GHz and the aforementioned spacing of $\lambda/2$. If the carrier frequency is increased to 79 GHz while keeping the previous spacing, the aperture equals the green line in

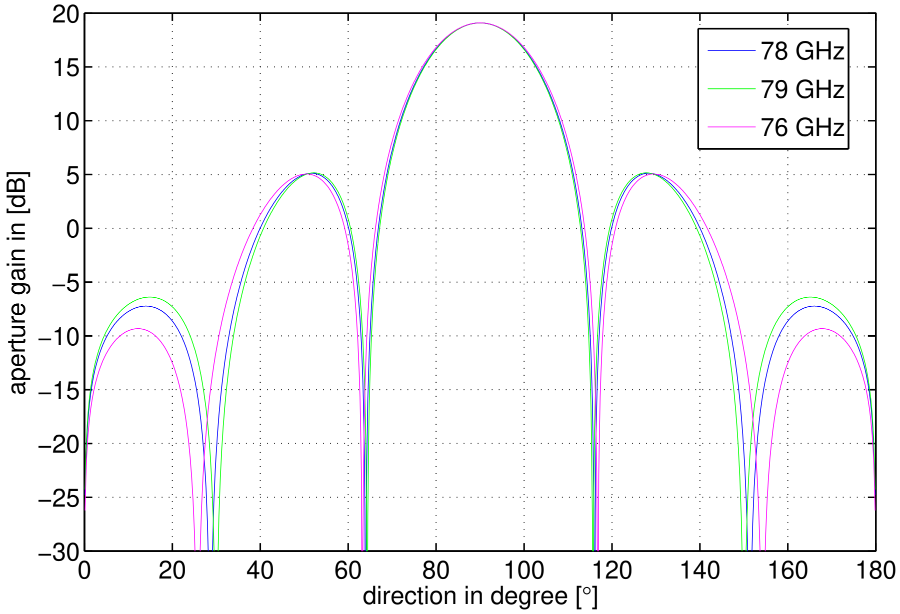

Figure 4.11 – Effect on antenna pattern for different carrier frequencies at a fixed antenna spacing according to $\lambda/2$, $f_c = 78$ GHz

Figure 4.11. Besides, the carrier frequency is decreased to 76 GHz, which results in the magenta line.

In summary, the simulation results show, that although the amplitude of the antenna aperture does not change in main beam direction, the side-lobes including the directional nulls get shifted by tuning the frequency while the physical spacing remains fixed. For broadband applications, where the deviations cannot be neglected, the signal processing stage can be calibrated to the frequency dependent changes in antenna aperture. As the effect is reproducible and computable from mathematical models, the aperture change therefore can be factored in for such applications that incorporate DoA estimation, where the side-lobe and directional null shifts play a role.

For a more general setting, namely a main beam direction other than 90 deg, the array factor (AF) is introduced according to [52], where the AF is again described depending on the incident angles ϑ, φ.

$$\mathrm{AF}(\vartheta, \varphi) = \sum_{i=0}^{N-1} a_i \cdot \mathrm{e}^{j\varphi_i} \mathrm{e}^{k r_i \cdot \hat{r}} \tag{4.11}$$

The excitation $a_i \cdot \mathrm{e}^{j\varphi_i}$ depends on the direction of the main beam, which can be changed with an individual signal phase shift at each antenna element i.

$$\varphi_i = i \cdot \beta \tag{4.12}$$

The vector $r_i = [x_i, y_i, z_i]$ gives the coordinates according to (4.13).

$$\hat{r} = \hat{x} \cdot \sin\vartheta \cos\varphi + \hat{y} \cdot \sin\vartheta \sin\varphi + \hat{z} \cdot \cos\vartheta. \tag{4.13}$$

Given a distance d between two antenna elements in a linear array the position of the i^{th} element is $r_i = i \cdot d$. For $a_0 = a_1 = \dots a_{N-1}$ the AF is rewritten as

$$\begin{aligned}
\mathrm{AF}(\vartheta, \varphi) &= a \cdot \sum_{i=0}^{N-1} \mathrm{e}^{ji\beta} \mathrm{e}^{jkid\cos\vartheta} && (4.14)\\
&= a \cdot \sum_{i=0}^{N-1} \mathrm{e}^{ji(kd\cos\vartheta + \beta)} && (4.15)\\
&= a \cdot \sum_{i=0}^{N-1} \mathrm{e}^{ji\psi(\vartheta)}. && (4.16)
\end{aligned}$$

As a result, the main beam location is controlled with $\psi(\vartheta)$ in (4.17), whereas the wave number corresponds to $k = \frac{2\pi}{\lambda}$.

$$\psi(\vartheta) = k \cdot d \cdot \cos\vartheta + \beta \tag{4.17}$$

Accordingly, the central equation to change the main beam direction in a phased array is

$$\beta = -\frac{2\pi}{\lambda} \cdot \cos\left(\vartheta_{max}\right) \ . \tag{4.18}$$

The normalized AF can be simplified via $\sum_{i=0}^{N-1} \mathrm{e}^{i} = \frac{c^N - 1}{c-1}$ to the fraction

$$\mathrm{AF}(\vartheta, \varphi) = \frac{\sin\left(N \cdot \psi/2\right)}{N \cdot \sin\left(\psi/2\right)} \tag{4.19}$$

Regarding algorithm implementation, the normalized version of the AF in 4.19 is beneficial to runtime, since a for-loop can be avoided. But it should be noted, that (4.19) becomes undefined for the main lobe direction, since the denominator becomes zero at this position. Therefore, additional routines are necessary, eventually eliminating the advantage of the loop-avoiding implementation.

Phased arrays enhance radar perception in multiple ways, such as increasing the gain in main lobe direction or shaping the beam. In addition, changing the main lobe direction electronically, allows a highly flexible aperture pattern generation that can be again used for CS approaches that qualify to increase spatial resolution.

Although other waveforms qualify as well, the same transmit signal that was used for the RMPI approach is assumed, which is a modulated chirp of chirp duration t_s and the bandwidth B at the carrier frequency f_c.

$$s_t(t) = \mathrm{e}^{j2\pi f_c t} \cdot \mathrm{e}^{j\pi\alpha \cdot \left(t - \frac{1}{2}t_s\right)^2} \cdot \mathrm{rect}\left(t - \frac{t_s}{2}, t_s\right) \tag{4.20}$$

The received signal experiences a time shift depending on the distance of the target and a Doppler shift according to the relative speed between the platform and the target, analogous to the previous RMPI approach. Hence, the receive signal $s_r(t)$ incorporates the time shift τ_d, that comprises both effects.

$$s_r(t) = \mathrm{e}^{j2\pi f_c t} \cdot \mathrm{e}^{j\pi\alpha\cdot\left(t-\tau_d-\frac{1}{2}t_s\right)^2} \cdot \mathrm{rect}\left(t-\tau_d-\frac{t_s}{2}, t_s\right) \tag{4.21}$$

The aperture pattern for each main lobe direction ϑ_i is denoted with the steering vector $a(\vartheta_i)$ according to (4.22).

$$a(\vartheta_i) = \left[1 \ \mathrm{e}^{j2\pi\frac{d_0}{\lambda}\sin\vartheta_i} \ldots \mathrm{e}^{j2\pi(M-1)\frac{d_0}{\lambda}\sin\vartheta_i}\right]^T \tag{4.22}$$

The resulting steering matrix for K main lobe directions corresponds to $A(\vartheta) = [a(\vartheta_0)a(\vartheta_1)\ldots a(\vartheta_{K-1})]$. In the context of CS, the steering matrix and hence the known sensor positions can be understood as an overcomplete dictionary for spatial CS such as suggested in [68]. The observation that results from the model in (4.23) is then used for stating the CS optimization problem and solving for superresolution, i.e. synthetically increasing the number of main lobe directions.

$$y(t) = A(\Theta)s_r(t) \tag{4.23}$$

The signal acquisition is performed using a correlation receiver, whereas each implemented main lobe direction is processed individually as sketched in the block schematic principle in Figure 4.12. As could be expected from the overcomplete dictionary that is stated by the sensor positions, the reconstruction performance of the CS algorithm is of very good quality. The quality in superresolution for spatial separability in automotive use cases needs further analysis and evaluation, especially while incorporating automotive specific constraints that mainly originate in hardware development costs within a cost-sensitive market.

Due to the equivalently chosen signal model, additionally the signal processing in range direction can be performed using the RMPI approach, thus easing the signal acquisition issue. That means, that the reference signal denoted as $S_r ref$ in Figure 4.12 either can be a filter bank according to a correlation receiver or a random measurement sequence. For individual main beam directions, the aperture matrix $A_p \in \mathbb{C}^{M\times N}$ reflects M spatial sampling points and N samples taken in the range directions.

$$y_{ap}(\vartheta_i, t) = A_p(\vartheta_i) \cdot s_r(t) \tag{4.24}$$

Consequently, (4.24) is the CS problem statement, which shows the same reconstruction behavior as the RMPI.

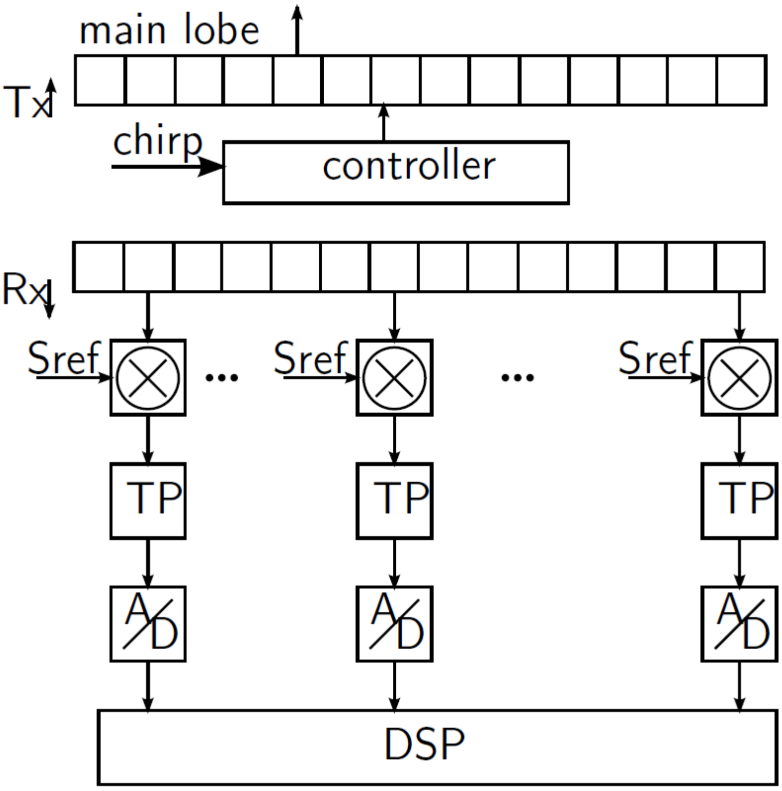

Figure 4.12 – Principle of CS based signal acquisition of a linear antenna array

4.2 CS Noise Radar

After introducing the RMPI based signal acquisition concept for a pulsed radar and showing possibilities that phased arrays offer for an improved radar perception, this section describes the author's proposal for applying CS to automotive radar, by implementing a CS based noise radar. The concept uses noise modulated pulses that are acquired with a modified correlation receiver, deploying only a reduced number of filter banks. Reducing the number of filter banks is critical in order to reduce the computation run time for online application, since in automotive scenarios obstacles need to be recognized fast enough to initiate reaction maneuvers. The reduced number of correlations and therefore range gates does not imply a limitation in range or a decrease in range resolution, since the signal acquisition is performed by applying CS methods.

The CS approach on noise radar will be discussed in more detail as it offers a high potential for solving the problem of robust radar systems in environments with a high sensor density while obtaining a comparable high resolution and keeping the sampling effort low. In contrast to the RMPI approach, no substantial hardware changes are required. Nevertheless, an access to additional interfaces of FMCW radar chips is required, which is indeed a drawback from the effort and cost perspective, but an effort that still remains at a low scale. The concept and its benefits regarding interference has been explained in [86] and the theory behind the suggested concept is elaborated in this section.

The main idea behind using noise modulated pulses for radar is to benefit from the advantages of pulse shaped radar on the one hand and mitigate its disadvantages on the other hand. Disadvantages of pulses lie in their range limitation due to free space propagation but also high side lobes in the frequency domain, that result from rectangular waveforms. Therefore, despite of the high robustness against interference that pulsed radar systems show, the possibility for reasonable applications remains in very short ranges such as tank level measurements in industrial plants. Using noise modulated pulses instead, levels not only the required transmit power, but also attenuates the side lobes in the frequency domain.

Additionally, noise modulation comes with a comparable low effort because either thermal noise can be amplified or delay lines that introduce RF effects such as suggested by the author in [89] can be used. Noise modulation also improves the robustness towards interference by adding a fingerprint to each pulse, which is comparable to coding techniques. However, noise modulation does not necessarily cause the same pulse spreading in time such as coding, which increases the time until a scene is captured and hence might cause critical delays for obstacle detection. Due to replacing direct sampling by CS observations, the sampling rate equals the pulse repetition interval avoiding the otherwise necessary high Nyquist frequency. Depending on the object sparsity of the surrounding environment, the number of correlation based measurements can be reduced by 60 % to 70 % as shown in the following section, where a proof of concept is given in a simulation. In summary, CS processed noise radar enables the implementation of a robust pulsed radar system, while ensuring that each pulse can be recognized by its fingerprint and still mitigating additional effort in signal acquisition and run time of the correlation receiver.

The concept behind the noise radar goes back to fundamental principles of information theory. The following paragraph is a short deep dive into information theory fundamentals, which recalls fundamental equations from [40] that are essential to understand why CS works in the suggested signal acquisition concept. According to Shannon, information is transmitted by signal energy. The signal energy therefore correlates to the entropy of a signal. Given a signal $s(t)$ that contains a symbol that should be transmitted, the energy of the symbol is computed by integrating the squared signal function over time according to (4.25).

$$E_{symbol} = \int_0^T s^2(t)dt \tag{4.25}$$

In a correlation receiver, which is the principle behind a matched filter (MF) receiver design, the product of the received signal $s_r(t)$ and the expected signal $s_e(t)$ is used to calculate the energy within an intervall corresponding to (4.25).

$$E_{symbol} = \int_0^T s_r(t) \cdot s_e(t) dt \tag{4.26}$$

In a general MF system description, the output $y(t)$ corresponds to the convolution of the input signal $x(t)$ and the system's unit impulse response $h(t)$.

$$y(t) = x(t) * h(t) \tag{4.27}$$

$$= \int_{-\infty}^{\infty} x(t) \cdot h(t-\tau) d\tau \tag{4.28}$$

Accordingly, a MF design specifies the expected signal $s_e(t)$ in (4.25) to be the mirrored unit impulse response $h(t-\tau)$ in (4.27) delayed by the time τ. Apart from the time shift τ, the unit impulse response equals the input signal, which is why it is also referred to as search or correlation filter. Usually, the number of correlation lines at the receiver stage corresponds to the number of possible symbols and accordingly covers the full symbol space. In terms of a MF design, a symbol is defined by the time shift τ_n resulting in a required number of correlation filters that equals the number of range gates according to range resolution and maximum range. For unique and unambiguous correlation results, qualified correlators need to be orthogonal to each other, meaning that (4.29) needs to be fulfilled, which is at same time a requirement on CS compliant measurement and reconstruction matrices.

$$\int_0^T s_1(t) \cdot s_2(t) dt \overset{!}{=} 0 \tag{4.29}$$

To avoid inter-symbol interference (ISI), subsequent symbols, i.e. signal copies shifted by the time delays τ_1 and τ_2, representing two subsequent range gates, must fulfill (4.30).

$$\int_0^T s_1(t-\tau_1) \cdot s_1(t-\tau_2) dt \overset{!}{=} 0 \tag{4.30}$$

Using noise modulation, (4.29) is fulfilled for subsequent noise pulses, if the noise is the result of a random uncorrelated process. Assuming in addition (4.30) for the CS measurement matrix design, i.e. the correlation receivers, the resulting matrix meets the requirements on coherence.

The signal acquisition process suggested in [15] relies on noise modulated pulses that are not only applied to the transmit antennas, but also to the receiver such as in FMCW receivers. But in contrast to FMCW receivers, the transmit signal is applied to several delay lines, thus implementing the measurement or reference signals of the correlation receiver. The resulting time-shifted copies of the transmit signal

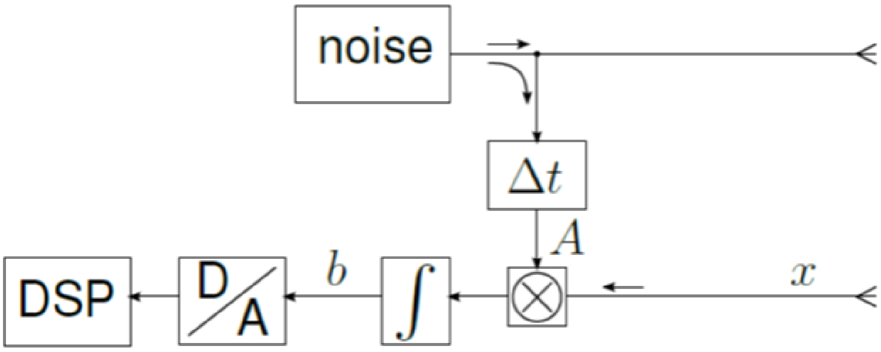

Figure 4.13 – In contrast to CCF receivers, the correlation output is integrated over maximum pulse roundtrip time.

that are used for correlation in the receiver, represent distortion free receive signals corresponding to several randomly chosen round-trip times of signal propagation. Figure 4.13 depicts the block schematic of such a receiver, whereas the measurement signals are denoted with the matrix A. Basically, it is sufficient to determine the existence and range of a reflecting target from the energy that is obtained in each time bin, i.e. range gate, such as in [79]. Beyond short ranges, this method results in a cumbersome procedure for major distances, if it is aimed to preserve the range resolution. Therefore, the energy obtained from each time bin is interpreted as an observation instead, that is used to reconstruct the remaining energy levels by stating an underdetermined system of equations using the measurement matrix A and the observations at each range gate.

Assuming N required range gates according to regular correlation receivers, a subset of M range gates, i.e. time shifts Δt_m are realized. Subsampling ratios are therefore expressed with the quotient $\frac{M}{N}$.

4.2.1 Signal Model

For the noise radar concept, two different noise processes are considered by the author, whereas one reflects an idealized band-limited white noise signal for analysis purposes and the second one reflects colored noise, that contains weighted spectral components within a specified bandwidth. Unless stated otherwise, the waveforms and the analysis are described in the frequency domain. In (4.31) the band-limited white noise transmit pulse such as applied in [86] is stated. It serves mainly for study and analysis purposes of the concept, but in itself it is rather an idealized signal model than an implementable waveform.

$$X_{wn,nn}(f) = \begin{cases} \frac{N_0}{2}, & \text{if} -\frac{B}{2} \leq f \leq \frac{B}{2} \\ 0, & \text{otherwise} \end{cases} \tag{4.31}$$

The factor corresponds to the thermal noise $N_0 = kT_aB$ with the Boltzmann constant k, ambient temperature T_a and bandwidth B. Normalizing (4.31) to one and using the rectangular function for a closed signal statement, the signal turns into (4.32).

$$X_{wn}(f) = \mathrm{rect}\left(\frac{f}{2B}\right) \tag{4.32}$$

In time domain this pulse form corresponds to the sinc-function (4.33).

$$\begin{aligned} x_{wn}(t) &= 2B\frac{\sin(2\pi Bt)}{2\pi Bt} \\ &= 2B\,\mathrm{sinc}\,(2\pi Bt) \end{aligned} \tag{4.33}$$

The second noise waveform, i.e. the colored noise, is derived from the rectangular shape in frequency and features randomly weighted spectral components within the bandwidth B.

$$X_{rn}(f) = W(f)\cdot \mathrm{rect}\left(\frac{f}{2B}\right) \tag{4.34}$$

The weighting function $W(f)$ diversifies the contributions of individual spectral components within the specified bandwidth. It takes a random process to generate the weighting coefficients in such a way that the spectral components sum up to a unique fingerprint for each transmit pulse. As such the weighting function is generated by a random process that corresponds to a standard normal distribution, i.e. variance $\sigma = 1$ and mean $\mu = 0$, which is described by the probability function in (4.35).

$$p(W(f)) = \frac{1}{\sqrt{2\pi}\ e^{-\frac{1}{2}W(f)^2}} \tag{4.35}$$

The waveforms are depicted in time and frequency domain in Figure 4.14.

The channel model features the time delay τ_l resulting from the two-way propagation between the radar sensor location and each of the L reflecting targets in the scene. While the sensor platform is moving with the velocity v_e, most targets are dynamic moving with a velocity $v_l > 0$, which results in relative velocities $v_r = v_e - v_l$. The overall time shift $\tau_{s,l}$ after two-way signal propagation through the channel to and from the targets, is accordingly composed not only of the time shift τ_l but also of the Doppler time shift $\tau_{D,l}$.

$$\begin{aligned} \tau_{s,l} &= \tau_l + \tau_{D,l} \\ &= \frac{2r_l}{c_0} + \frac{-2v_rt}{c_0} \\ &= \frac{2\left(r_l - v_rt\right)}{c_0} \end{aligned} \tag{4.36}$$

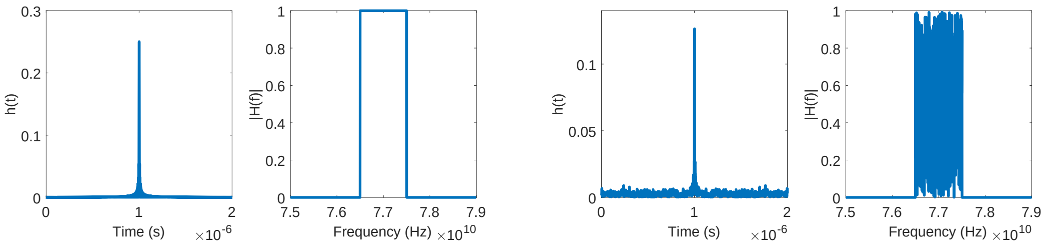

(a) Bandlimited white noise waveform (b) Bandlimited random noise waveform

Figure 4.14 – Transmit waveforms in time and frequency domain with Figure 4.14 a white noise and Figure 4.14 b random noise.

Incorporating the target related channel attenuation a_l, the receive signal becomes the sum in (4.37).

$$S_{r,p} = \sum_{l=0}^{L-1} a_l \cdot S_t(f) \cdot e^{-j2\pi f_c \tau_{s,l}} \tag{4.37}$$

During the signal acquisition, the channel is assumed to be stationary, so that all parameters are constant during one sweep. Transmitting several pulses P with time spacing τ_p increases the SNR in the receive path on the one hand, on the other hand it increases the Doppler resolution.

$$\begin{aligned} S_r &= \sum_{p=0}^{P-1} S_{r,p} \cdot e^{-j2\pi f \tau_p} \\ &= \sum_{p=0}^{P-1} \sum_{l=0}^{L-1} a_l \cdot S_t(f) \cdot e^{-j2\pi f \tau_{s,l}} \cdot e^{-j2\pi f \tau_p} \\ &= \sum_{p=0}^{P-1} \sum_{l=0}^{L-1} a_l \cdot S_t(f) \cdot e^{-j2\pi f \left(\tau_{s,l} + \tau_p\right)} \end{aligned} \tag{4.38}$$

The transmit signal $S_t(f)$ in (4.37) and (4.38) corresponds to the waveforms stated in (4.32) and (4.34).

According to the general radar range equation based on Frii's formula, the radar range equation for two-way propagation is defined in (4.39) for a radar systems using noise waveforms [44].

$$P_R = \frac{P_T G_T G_R S_0 \lambda^2}{(4\pi)^3 L R^4} \tag{4.39}$$

To determine the minimum detectable receive signal power $P_{R,min}$ not only the unwanted noise power P_N in (2.7) needs to be considered as continuous wave radar systems. There, a definition depending on the expected SNR is feasible. Instead, the detectability factor D comes into play in (4.40), which is specific to pulsed waveforms and replaces the alternative formulation via the SNR.

$$P_{R,min} \geqslant P_N \cdot D \tag{4.40}$$

To compute the detectability factor D for the medium pulse integration time t_i in (4.41), a threshold D_0 is chosen according to the probability of detection and the probability of false alarm, i.e. false alarm rate (FAR).

$$D = \frac{D_0}{t_i B} \tag{4.41}$$

The medium integration time [44] is restricted by the time-bandwidth product (4.42), where the propagation time and the maximum velocity v_{max} frame constraints on parameter selection.

$$t_i \cdot B \leqslant \frac{c_0}{2 v_{max}} \tag{4.42}$$

According to [17], the velocity resolution of a noise modulated pulse radar tends to be rather poor, which can be only met by allowing a sufficiently long pulse integration time.

After designing the pulse shape, the transmit waveform still has to reflect a realistic impulse response by limiting the impulse response in time with a window function, e.g. a rectangular, Hamming or Hann window. As the signal is processed and analyzed in the frequency domain, the window function in the time domain is not elaborated here. The inherent limitation of the frequency band that can be adapted to real environment and hardware constraints, contributes a distortion free channel.

4.2.2 Signal acquisition and reconstruction

In the following paragraphs the signal acquisition using a modified, i.e. reduced correlation receiver followed by CS signal reconstruction is presented along with the underlying signal theory. Depending on the analysis aim, it is beneficial to either work with a signal and processing model in the time domain or in the frequency domain. The duality of Fourier transformation specifies how to switch easily between time and Fourier domain, if necessary. According to the frequency shift property stated in (1) a frequency shift results in an according envelope in the time domain.

$$\mathrm{e}^{j\omega_0 t} x(t) \;\frac{\quad}{}\!\!\circ\; X(\omega - \omega_0) \tag{4.43}$$

Vice versa, the time shift property in (2) states that a time shift corresponds to a frequency shift in the Fourier domain.

$$x(t - t_0) \multimap \mathrm{e}^{-j\omega t_0} X(\omega) \tag{4.44}$$

Sampling and therefore discretization in the time domain reflects a convolution of the signal to be sampled with a chain of Dirac pulses spaced with the usually equidistant interval kT (4.45).

$$f(t - kT) = f(t) * \delta(t - kT) \tag{4.45}$$

Non-uniform sampling varies the spacing between sequential Dirac pulses and hence realizes different sampling frequencies. The Fourier transformation of a discrete Dirac pulse chain in (4.46) shows the interdependency between sampling rate and sampling frequency with $\frac{k}{T}$ being the correspondent frequency steps to the time sampling intervals kT.

$$\sum_{k=-\infty}^{\infty} \delta(t - kT) \multimap \frac{1}{T} \sum_{k=-\infty}^{\infty} \delta\left(f - \frac{k}{T}\right) \tag{4.46}$$

The foundation of a correlation receiver lies in designing a filter that maximizes the output of the filter stage at the receiver side. With a signal $s(t)$ of finite energy E and the impulse response $h(t)$ corresponding to a transfer function $H(f)$ of a filter, the output of the filter stage equals $y(\tau)$ according to (4.47).

$$y(\tau) = \int_{-\infty}^{\infty} s(\tau - t) h(t) \,\mathrm{d}\,t \tag{4.47}$$

The energy is computed by integrating the square of the absolute value of an energy signal, resulting in (4.48).

$$\begin{gathered} \int_{-\infty}^{\infty} |h(t)|^2 \,\mathrm{d}\,t = E \\ \int_{-\infty}^{\infty} |s(t)|^2 \,\mathrm{d}\,t = E \end{gathered} \tag{4.48}$$

The Cauchy-Schwarz inequalty (4.49) states as a consequence from (4.48), that the energy at the output of the filter stage cannot exceed the energy of the individual signals or impulse responses.

$$\int_{-\infty}^{\infty} s(\tau - t) h(t) \,\mathrm{d}\,t \leqslant \sqrt{\int_{-\infty}^{\infty} |s(\tau - t)|^2 \,\mathrm{d}\,t} \sqrt{\int_{-\infty}^{\infty} |h(t)|^2 \,\mathrm{d}\,t} \leqslant E \tag{4.49}$$

The impulse response $h(t)$ can be expressed with its eigenvalues λ, whereas $\lambda > 0$.

$$h(t) = \lambda s(\tau - t) \tag{4.50}$$

In order to maximize the energy at the filter stage output in (4.47), the eigenvalues are set $\lambda = 1$ and therefore the optimal impulse response becomes $h(t) = s(\tau - t)$.

$$\max(y(\tau)) = \int_{-\infty}^{\infty} |s(\tau - t)|^2 \,\mathrm{d}\,t = E \tag{4.51}$$

A correlation receiver therefore contains a set of time shifted copies of an expected signal to determine which time shift results in the maximum energy and therefore obtain the actual time shift. In applications where transmitter and receiver systems are synchronized e.g. with pilots that are known at both ends, the correct time shift $t = \tau$ is determined. Accordingly, $h(t)$ is matched to the propagation channel and is therefore called the MF for (4.51). This approach is widely used in communication systems using methods such as OFDM. In case of moving targets, the correlation receiver incorporates not only the range propagation time shift but also the velocity difference between transmitter and moving target. Correlation processing of moving targets in general, but also for noise modulated pulses [44], includes according to the time and frequency shift properties in (2) and (1) the propagation component as a time shift and the Doppler shift component as power to the e-function resulting in the complex envelope of the receive signal in (4.52).

$$\begin{aligned} x_r(t) &= \alpha x_t \left(t - \frac{2r}{c}\right) \mathrm{e}^{j2\pi\left(-\frac{2v_l f_c}{c}\right)t} \\ &= \alpha x_t \left(t - \tau_{r,l}\right) \mathrm{e}^{-j2\pi f_c \tau_{D,l}} \end{aligned} \tag{4.52}$$

With the additional Doppler direction, a non-matched filter with an integration interval T features additionally the windowing function $w(t)$ providing the range-Doppler ambiguity function $y(r, v)$ according to (4.53).

$$y(r, v) = \int_{t=0}^{T} w(t) x_r(t) x_t^* \left(t - \frac{2r}{c}\right) \mathrm{e}^{j2\pi\left(-\frac{2v_l f_c}{c}\right)t} \underset{\cdot}{\mathrm{t}} \tag{4.53}$$

The matched filter is designed to have the same Doppler integration time as the receive signal and therefore does not have an additional windowing function (4.54).

$$y(r, v) = \int_{t=0}^{T} x_r(t) x_t^* \left(t - \frac{2r}{c}\right) \mathrm{e}^{j2\pi\left(-\frac{2v_l f_c}{c}\right)t} \underset{\cdot}{\mathrm{t}} \tag{4.54}$$

Given an ergodic random process $x(t)$, the ACF $R_{xx}(\tau)$ states the inverse Fourier transform of the power spectral density function $S_x(f)$ [15]. From the information theoretical point of view, reflected radar signals are stochastic signals as they carry information about environment and target scenarios that are not known a-priori and cannot be determined in advance from previous signals. In practice, this assumption seems to be only partially true, because object tracking is indeed applied on a higher system level to accelerate radar perception. During one test drive the environment and target scenario will most of the time not change spontaneously, in the sense that a car moving in front will not suddenly disappear. On the other hand, it is always possible that new objects appear out of the blue. Additionally, it is not possible to determine the target scenario in a street from previous records, because the target scenario will always be different apart from static objects such as buildings. But still, a target scenario does not depend from previous scenarios. Technically speaking, the target scenario system block does not have a memory, that would allow to determine future targets from previous perceptions. Therefore, even tracking does not prevent the reflected radar signal from being a stochastic process.

$$R_{xx}(\tau) \Leftrightarrow S_x(f) \tag{4.55}$$

The peak of the ACF at $\tau = 0$ corresponds to the average power $P_{ave}(t)$ of the ergodic random process x(t). In order to determine the time shift that matches the one obtained in the receive signal best, either the peak of the individual correlation functions can be compared or the energy by integrating the correlation function.

$$P_{ave}(t) = R_{xx}(\tau) \tag{4.56}$$

The correlation process, which corresponds to a convolution in the time domain, equals the multiplication of the signal with its conjugate complex and hence the square of its absolute value for $\tau = 0$ according to the Wiener-Khinchine theorem [40] stated in (4.57).

$$u(t) * u^*(t) \;\frac{\quad}{}\!\!\circ\; U(f) \cdot U^*(f) = |U(f)|^2 \tag{4.57}$$

Using the Wiener-Khinchine theorem as well as the time and frequency shift property, the reference signals $s_{ref}(t)$, i.e. the correlation filter bank, are stated in a reference matrix using the frequency representation. Since these signals, other than the transmitted signal do not experience the channel characteristics, it differs from the original transmit signal only regarding the time shift and is not affected by other channel characteristics such as noise or attenuation. Hence, the matrix of reference functions $S_{t,ref}(f, \varDelta t)$ corresponds in the compressive sensing context to a measurement matrix, that is denoted as the measurement matrix $\varPhi$ in the general compressive sensing formulation.

$$S_{t,ref} = \begin{bmatrix} \mathrm{e}^{j2\pi f_0 \varDelta t_0} & \mathrm{e}^{j2\pi f_1 \varDelta t_0} & \dots & \mathrm{e}^{j2\pi f_{N-1} \varDelta t_0} \\ \mathrm{e}^{j2\pi f_0 \varDelta t_1} & \mathrm{e}^{j2\pi f_1 \varDelta t_1} & \dots & \mathrm{e}^{j2\pi f_{N-1} \varDelta t_1} \\ \vdots & \vdots & \ddots & \vdots \\ \mathrm{e}^{j2\pi f_0 \varDelta t_{M-1}} & \mathrm{e}^{j2\pi f_1 \varDelta t_{M-1}} & \dots & \mathrm{e}^{j2\pi f_{N-1} \varDelta t_{M-1}} \end{bmatrix} \cdot \mathrm{diag}\left(S_{t,f(0)\dots f(N-1)}\right) \tag{4.58}$$

The expression $\operatorname{diag}\left(S_{t,f(0)\ldots f(N-1)}\right)$ denotes the diagonal matrix with the vector elements of $S_t(f)$. Using the measurement matrix $S_{t,ref}$, the scalar products in R_{xy} of the reference signals and the actual received signal are computed.

$$R_{xy} = S_{t,ref}^H \cdot S_r \tag{4.59}$$

So far, the signal acquisition does not differ from other correlation receivers. Depending on the range that should be covered by a radar and the aimed range resolution, a complete correlation bank requires too much effort and computational runtime at the receiver side to be applied in on-line automotive applications that require fast reaction times. Therefore, instead of processing all N correlations, the signal acquisition is performed using a random subset of M different reference signals, i.e. time shifts, stating a reduced compressive sensing measurement matrix. The M observations from (4.59) are used to reconstruct the original receive signal and time shift information using an implementation of the OMP algorithm. From this point the procedure resembles therefore the RMPI approach with the minimization objective in (4.60), while exploiting the spatial sparsity of the target scenario.

$$\min ||\hat{S}_r||_{\ell_1} \quad s.t. \quad ||R_{xy} - S_{t,ref}^H \cdot \hat{S}_r||_{\ell_2} \leqslant \varepsilon \tag{4.60}$$

The feasibility of the measurement matrix is analyzed in the following section, while the number of sufficient measurements M are determined experimentally.

4.2.3 Compressive Sensing Analysis

To check the feasibility of the measurement matrix, three different metrics are used for analysis. The worst-case coherence is a measure for the coherence of the columns of a matrix A [21]. The lower the mutual coherence of the measurement matrix, the higher is the probability of successful compressive sensing reconstructions. It is computed by finding the highest scalar product in between the columns of the matrix A and marks the highest correlation that occurs in between the columns. The norming factor is the product of the Euklidean norms of the vectors that are used for scalar product computation.

$$\mu_A = \max_{i \leqslant i \neq j \leqslant N} \frac{|\langle a_i, a_j \rangle|}{\|a_i\|_2 \|a_j\|_2} \tag{4.61}$$

The coherence between the rows of the matrix are computed with the spectral norm of A [6], which is the same as the maximum singular value of A or the Euclidean norm.

$$\|A\|_2 = \sqrt{\lambda_{max}\left(A^T A\right)} \tag{4.62}$$

For stating the point-spread function (PSF) of the projection matrix, it is decomposed to an undersampled transformation operator F_u and the $\{i, j\}$-th vectors e of a natural basis, which is derived and explained with the example of an undersampled Fourier transformation operator in [58].

$$\mathrm{PSF}(i,j) = e_j^* \cdot F_u^* F_u \cdot e_i \tag{4.63}$$

In the case where the natural basis equals the identity matrix such as here, where the measurement matrix equals the correlation matrix, the PSF of A equals the Gram matrix [82] thus corresponding to the ACF matrix of the noise radar correlation receiver.

$$G = A^T A \tag{4.64}$$

In the absence of mutual correlation between the matrix elements, the energy is distributed only on the main diagonal, resulting in $\mathrm{PSF}(i,j)|_{i \neq j} = 0$. This ideal case cannot be obtained in an undersampled setting, since the subsampling results in non-idealities within the matrix elements. As a consequence, the PSF obtains sidelobes, such that $\mathrm{PSF}(i,j)|_{i \neq j} \neq 0$. But also in the full set of correlators, mutual intereference within the elements occur while being applied and processed by the same hardware. Based on the PSF, another metric that reflects these non-idealities is derived to measure the level of incoherence, i.e. the maximum sidelobe-to-peak-ratio (SPR). According to (4.65), the SPR is the ratio of the maximum PSF obtained for any sidelobe to the main lobe PSF such as used among others by [58].

$$\max_{i \neq j} \left| \frac{\mathrm{PSF}(i,j)}{\mathrm{PSF}(i,i)} \right| \tag{4.65}$$

In a real system, where the ideal case of completely disappearing sidelobe elements cannot be obtained, the matrix A is considered as a feasible matrix, if the diagonal elements have much higher values than the off-diagonal elements. A high SPR indicates a low correlation between the rows and columns exist as only auto-correlation leads to significant levels in the Gram matrix. Although an optimal matrix is expected to have true random characteristic in oder to increase the probability of beeing mutually uncorrelated, other and especially also cyclic matrices can be feasible as well. The latter is of particular interest, since real systems introduce always some cyclic dependencies by their digital or analog filter characteristic, which is often even unintendend. In the following, several matrices are compared to each other according to the mutual coherence and the spectral norm, while the frequency band is assumed to be limited with an ideal bandpass filter to the specified bandwidth B. In practical aspects it is not only hard to create this type of waveform, but it also comes along with high sidelobes in correlation processing. Therefore, another beneficial aspect of using noise waveforms is that the correlation induced high sidelobes are reduced and subsequently lead to an improve of the reconstruction performance. The comparison of the Gram matrices in Figure 4.15 contains an unstructured

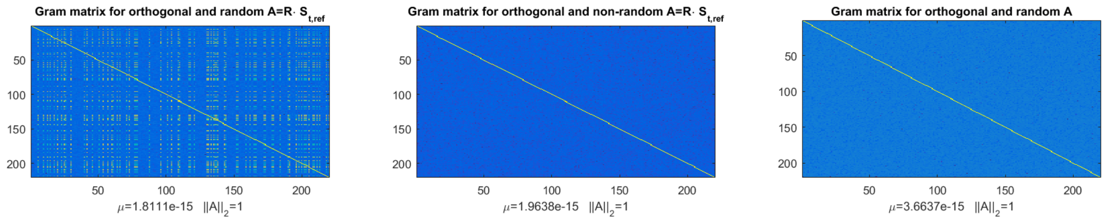

(a) orthogonalized random (b) orthogonalized sorted (c) orthogonalized random

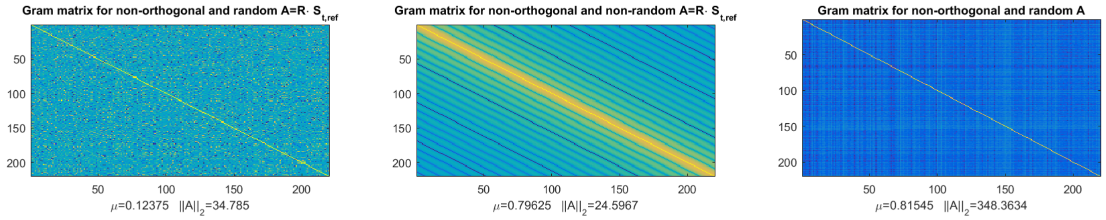

(d) non-orth. random (e) non-orth. sorted (f) non-orth. random

Figure 4.15 – Gram matrices referring to the frequency domain for a Figure 4.15 a, Figure 4.15 b, Figure 4.15 d, Figure 4.15 e: subset of time shifts, Figure 4.15 c, Figure 4.15 f: matrix entries. All matrices were designed with N columns and $M = 0.1 \cdot N$ rows.

random matrix generated according to standard normal distribution in Figures 4.15 c and 4.15 f. The other matrices are two variations of the reduced correlation matrices. While both matrices contain a subset of the complete correlation set $S_{ref} \in \mathbb{C}^{N \times N}$, the reference selection operator R in one case arranges the extracted subset correlation matrix $A = R \cdot S_{ref}$ in a sorted way, while in the other case the individual signal selections are arranged randomly in the resulting subset $A \in \mathbb{C}^{M \times N}$. The difference in between the upper and lower lines of matrices in Figure 4.15 is that the upper line corresponds to non-orthogonalized matrices, which reflects a realistic hardware based matrix generation. The bottom line is the idealized case of orthogonalized measurement matrices.

While all matrices show a clear diagonal, the sidelobe patterns differ. Comparing Figures 4.15 d and 4.15 e reveals that randomizing the subset helps to distribute correlated sidelobe matrix entries and therefore improves the reconstruction probability using CS. Especially the difference between the sorted and randomized subset function alignment should be noted as it shows that randomization leads to a structure of the Gram matrix by omitting distinct sidelobes.

The interdependency between reducing the correlation set and sidelobe entries is observed best by direct comparison. For the full correlation set of N randomized time shifts in Figure 4.16, the Gram matrix shows a pronounced diagonal, while still in the non-orthogonalized version of the correlation matrix, the Gram matrix shows some scattered peaks on off-diagonal places as well as Figure 4.16 a. The coherence of the full but randomized and non-orthogonalized correlation matrix is $\mu_A = 0.071025$ and the spectral norm $\|A\|_2 = 82.3755$. The off-diagonal elements

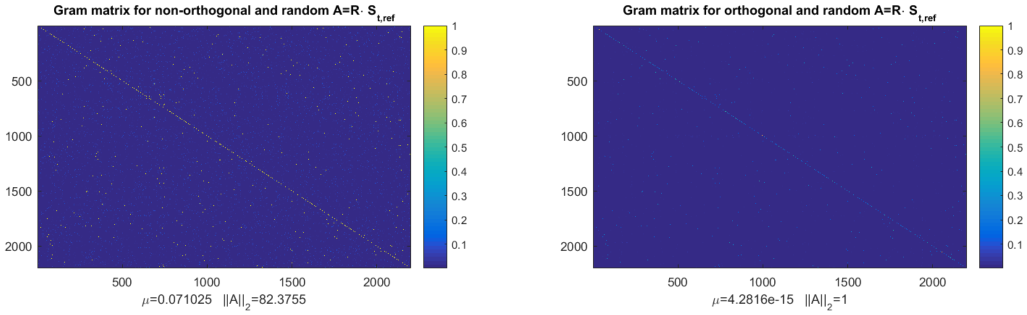

(a) non-orthogonalized full set (b) orthogonalized full set

Figure 4.16 – Randomly selected and aligned time shifts of the full set Figure 4.16 a non-orthogonalized, Figure 4.16 b orthogonalized.

disappear if the matrix is orthogonalized, but the values on the diagonal decrease as well. Nevertheless, the coherence decreases to $\mu_A = 4.2616e - 15$ and the spectral norm to $\|A\|_2 = 1$. Hence, orthogonalization affects first and foremost the spectral norm in a significant way, as the coherence μ_A remains in both cases sufficiently low, i.e. much lower than one, thus being a good hint for the feasibility of practical implementation.

Reducing the correlation set to a subset of M randomly picked time shifts, in that case $M = 0.3 \cdot N$ as this proofed to be a good compromise between reduction and performance in diverse environments, the Gram matrix improves regarding the SPR, while the other measures remain within the same range. As before, the PSF is compared to the non-orthogonalized correlation matrix in Figure 4.17 a and the orthogonalized matrix in Figure 4.17 b. Scatterers on the Gram matrix of the non-orthogonalized version are still present, but show a tendency towards the diagonal. The mutual coherence is similar to the complete set with $\mu_A = 0.060171$ while the spectral norm is slightly improved, i.e. decreased compared to the full set with $\|A\|_2 = 62.6076$. However, the reduction of the spectral norm is a consequence of having less rows in total and it has therefore limited value. For the orthogonalized reduced correlation matrix, the Gram matrix again shows a clear diagonal with only few and low scatters in the off-diagonal. But the presence of scatterers even in the orthogonalized version indicates the reduction of the correlations, thus leading to a rectangular instead of quadratic matrix. Analogously to the full set, the mutual coherence of the correlation matrix is lower compared to the non-orthogonalized with $\mu_A = 3.2321e - 15$ and the spectral norm $\|A\|_2 = 1$.

In summary, the correlation matrix $A = R \cdot S_{ref}$ that is designed from time shifted versions of the transmit waveform, is not completely uncorrelated according to the PSF evaluation . Furthermore, the correlation matrix is a circulant matrix, that especially in real hardware implementations is not orthogonal, which is best observed in Figure 4.17 a with the clear high energy elements within the off-diagonal area.

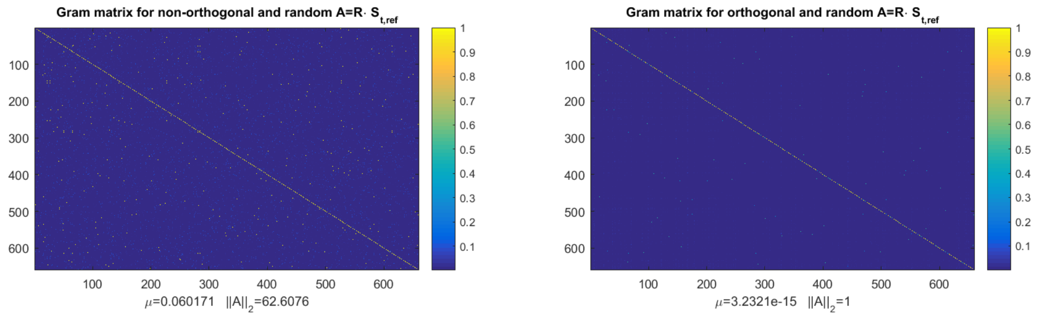

(a) non-orthogonalized sub-set of 30 %

(b) orthogonalized sub-set of 30 %

Figure 4.17 – Randomly selected and aligned time shifts reduced to 30 % Figure 4.16 a non-orthogonalized, Figure 4.16 b orthogonalized.

Applying non-orthogonalized and not completely uncorrelated circulant measurement matrices is justified by the fact, that hardware implementations always introduce these effects and therefore generating a perfectly uncorrelated matrix is always limited by system inherent correlations. In addition to the correlations produced within the time shifted versions of the transmit waveforms, the random process for signal selection will never be completely random as it can be implemented only in a finite manner. But also the noise modulation is not completely uncorrelated and depends on the underlying algorithm of the noise generator that produces sequences that are actually correlated. These characteristics lead to the non-ideal effects observed in the PSF analysis of the $N \times N$ matrix designed from a normally distributed random process that is depicted in Figure 4.16, showing the non-ideal behavior of the applied random generator.

4.3 Proof-of-Concept

The aim of the analysis performed with the noise radar concept is twofold to provide for the fact that either the concept itself may fail or further hardware adjustments are necessary. Especially for distinguishing those effects, a separate evaluation is therefore helpful. Evaluating the feasibility of the signal acquisition and reconstruction concept works best if the analysis is performed first detached from any hardware effects and constraints. Only if this proves to be successful, it makes sense to move on to hardware analysis. Hence, before emulating the noise radar correlation receiver, a proof-of-concept is performed in order to demonstrate basic feasibility of the radar concept. While the proof-of-concept focusses on the signal processing and reconstruction algorithm, the emulation additionally considers physical sensor characteristics.

4.3.1 Simulation Model

The proof-of-concept simulation simplifies the radar frontend by assuming isotropic antenna patterns and ideal transmitter and receiver stages without additional filter characteristics or noise sources. Each target is modeled as a point scatterer with equal RCS and the power of the receive signal is normalized to one. Due to the normalization, the free space propagation is not incorporated in the channel model. Instead, different SNR levels, that comprise any noise sources, either within the channel or the system, are used for benchmarking. Thus allows an initial estimate on applicability to a real system. Hereby, the channel noise is modeled as AWGN that is superposed to the receive signal. Assuming a discrete time vector of length N, with elements spaced by the time step Δt according to the range resolution and hence time bin, a regular correlation receiver requires N correlation filters. Sub-sampling defines here the reduction of the correlation matrix to $M \ll N$ with the sub-sampling rate $r = \frac{M}{N}$. The reduction capacities of the sub-sampling rate is derived from exploring the reconstruction performance with variations of the sub-sampling rate. The selection of the correlation filters results from an equally distributed random process, so that the time bins used by the correlation filters are not sorted but randomized. Varying the sub-sampling rates benchmarks the capability and applicability of the CS approach, as a low sub-sampling rate justifies and at the same time limits the initially raised implementation effort.

Besides SNR and sub-sampling, also the noise radar implementation is varied to determine the best setup of the individual components, which are measurement and reconstruction matrix and transmit waveform. Two different matrices are used, one of them is a completely uncorrelated random matrix, which is hard to realize on hardware, but is optimal from the perspective of CS requirements. Being completely uncorrelated random, makes the first matrix most suitable to act as an optimal CS reference implementation. The other matrix is introduced and analyzed in Section 4.2.2. It incorporates different randomly selected correlation filters in the spectral domain. Its characteristics reflect realistic features such as the circular structure due to the time shifts and the presence of mutual correlation of the matrix elements. In addition, the implementation of correlation filters, that are generated by delaying the transmit waveform and are then applied to the receiver, can be easily reproduced and avoids the necessity of storing the measurement matrix. Together with the reduced correlation matrix, two different waveforms are used. Both are pulses, whereas one pulse consists of band-limited white noise (4.32) and the other waveform features randomly weighted spectral components according to standard normal distribution (4.34).

During simulation, several system configurations are compared consisting of different matrix and pulse structures. The different matrix structures are a random matrix with entries derived from a process according to standard normal distribution and a reduced correlation matrix. All transmit waveforms are in principle pulse

Table 4.1 – Measurement matrix and waveform combinations for proof-of-concept simulation

ID	Measurement matrix	Waveform
M1	red. correlation	$S_t(f) = \mathrm{rect}\left(\frac{f}{2B}\right)$
M2	random sequences	$S_t(f) = \mathrm{rect}\left(\frac{f}{2B}\right)$
M3	red. correlation	$S_t(f) = w(f) \cdot \mathrm{rect}\left(\frac{f}{2B}\right)$
M4	random sequences	$s_t(t) = e^{-j\pi\alpha t^2}$

shaped. One pulse is obtained from band-limited white noise, the other one from band-limited noise with weighted components and the third one is a linear chirp (Table 4.1). First, the different matrices are used to measure band-limited white noise and perform the reconstruction by minimizing the ℓ_1-norm of the receive signal estimate in the Fourier domain (M1, M2). In (4.66), the reduced correlation matrix is used as measurement matrix, whereas the optimization objective is the ℓ_1 norm of the reconstructed signal spectrum S_r (M1).

$$\min ||S_r||_{\ell_1} \ s.t. \ ||r_{xy} - S^H_{t,ref} S_r||_{\ell_2} < \varepsilon \tag{4.66}$$

Furthermore, the reduced correlation matrix is applied to the noise pulse consisting of randomly weighted spectral components (4.67) (M3).

$$\min ||S_r||_{\ell_1} \ s.t. \ ||R_{xy} - S^H_{t,ref} S_{r,rnd}||_{\ell_2} < \varepsilon \tag{4.67}$$

The same optimization objective is used in (4.68), but there the measurement and reconstruction matrix is the random matrix $\varPhi_{rnd}$ containing elements that are generated by a random process according to standard normal distribution (M2).

$$\min ||S_r||_{\ell_1} \ s.t. \ ||y - \varPhi_{rnd} S_r||_{\ell_2} < \varepsilon \tag{4.68}$$

In the fourth and final measurement and reconstruction approach in (4.69), the random measurement matrix $\varPhi_{rnd}$ projects a linear chirp, such as used in commercial automotive radar systems (M4). In contrast to the other approaches, the CS acquisition takes place in the time domain.

$$\min ||s_r||_{\ell_1} \ s.t. \ ||y - \varPhi_{rnd} s_r||_{\ell_2} < \varepsilon \tag{4.69}$$

Table 4.1 lists the matrix-pulse combinations that are used during the proof-of-concept-simulation. In the following, the four stated acquisition methodologies are referred to as M1, M2, M3 and M4 according to Table 4.1 in order to simplify description and improve clarity.

In practical parametrization of the simulation runs, the sub-sampling rate was tuned from $r = 0.01$ to $r = 0.49$, since early evaluation showed that reconstructions already turned out to have only negligible to none deviations from the original ground truth waveform. Although SNR levels are expected to be higher in automotive applications, the SNR range is between −6 dB up to 6 dB. This not only tests the performance during adverse conditions, but even demonstrates how the CS methods can improve the state-of-the-art instead of only preserving it with a new method. The detection range was covered by sequentially placing the point-scattering target in the short, mid and long range, i.e. 30 m, 150 m and 270 m. The velocity of the targets was set to a relative velocity between radar-equipped ego-vehicle and moving target of 20 m/s to ensure comparable results. Furthermore, the analysis is limited to the evaluation of range reconstruction. In order to obtain a range resolution of 15 cm, the bandwidth was set to 1 GHz.

4.3.2 Simulation Results

Simulations with each parameter configuration were performed several times to cover numerical variations from the random processes. For each sub-sampling rate and SNR level, the absolute error $e_{abs} = \hat{r} - r_{true}$ of the reconstructed range $\hat{r}$ and the true range r_{true} and the relative error e_{rel} in range are computed and compared between the four different matrix and signal model combinations. The aim is to evaluate the performance regarding probability of information reconstruction while varying matrix and signal model. Since range reconstruction was applied for different range distances, the relative error e_{rel} of the reconstructed range is used to measure the reconstruction capability.

$$e_{rel} = \frac{\hat{r} - r_{true}}{r_{true}} \tag{4.70}$$

Each range region, i.e. short, mid and long range, has a different criticality regarding deviation from the real range value, thus defining here the ground truth, and therefore the relative error additionally benchmarks the impact of range reconstruction deviations. Accordingly, the first comparison evaluates the CS reconstruction performance for the band-limited white noise pulse measured with a random and a reduced correlation matrix. The different matrix-waveform combinations are denoted with M1-4, according to Table 4.1. The proof-of-concept results are structured as follows. First, the results for a pulsed band-limited white noise waveform measured with a reduced correlation matrix and a random matrix are presented. Then the results of the RMPI approach using a linear chirp is compared to a reduced correlation receiver using band-limited random noise. In the final comparison a closer look is given to the difference in performance between the white noise and colored noise waveform while applying a reduced correlation matrix for measurement and reconstruction.

Applying a random matrix to a pulsed waveform is close to classical CS approaches, where it was proven that random matrices fulfill the RIP condition while showing a low mutual coherence. Accordingly, the reconstruction performance in Figure 4.18 b and Figure 4.18 d is steadily high, almost independent from the SNR corresponding

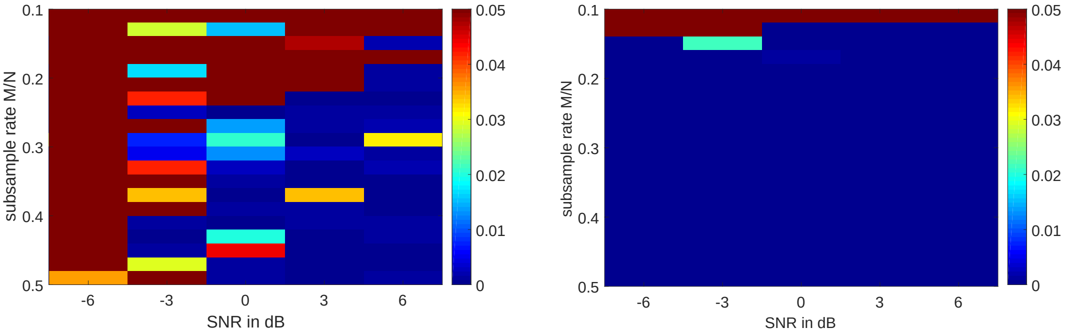

(a) M1: short range (b) M2: short range

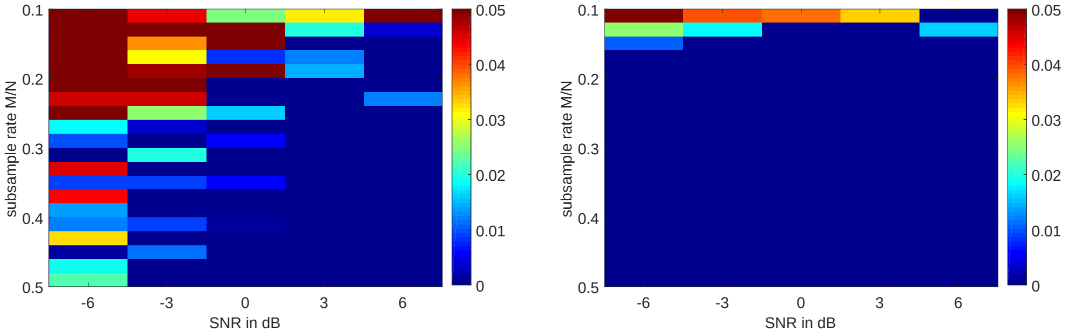

(c) M1: long range (d) M2: long range

Figure 4.18 – Relative error in range depending on sub-sampling rate in percent and SNR level for bandlimited white noise transmit waveform. Short range performance is represented with a target located at 30 m for Figure 4.18 a M1 (reduced correlation measurement matrix) and Figure 4.18 b M2 (random measurement matrix). Long range performance is tested with a target at 270 m for Figure 4.18 c M1 and Figure 4.18 d M2.

to general CS findings. In a correlation based concept, the matrix is already close to the transmit waveform. Band-limited white noise as transmit waveform and simultaneously basic waveform for generation of correlation filters increase the mutual coherence and therefore reduces the reconstruction capabilities. Therefore, the dependency of the reconstruction performance decreases for lower SNR levels, which according to the results in Figure 4.18 a and Figure 4.18 c can be partially compensated by increasing the number of measurements, i.e. correlations.

A separate evaluation of SNR and sub-sampling impact on reconstruction fidelity reveals the higher influence of SNR while using the correlation-related approach in Figure 4.19 a compared to the random matrix in Figure 4.19 c, that indicates even a negligible effect from SNR on M2. Reducing the sub-sampling rate below 15 % is possible using the random matrix of M2, see Figure 4.19 d, while the reduced correlation in M1 needs at least 30 % of the correlation set to reduce and stabilize the reconstruction error to a minimum. Still, the correlation effort is reduced by 70 % in M1.

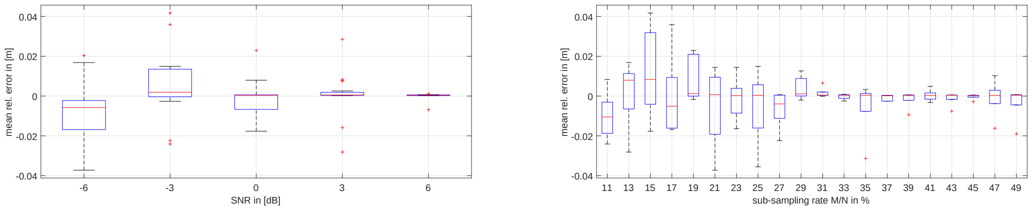

(a) M1: SNR (b) M1: sub-sampling

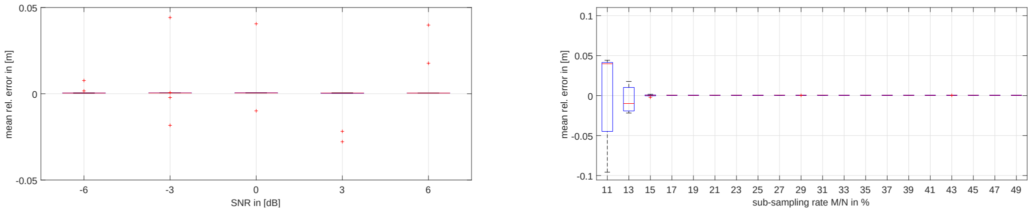

(c) M2: SNR (d) M2: sub-sampling

Figure 4.19 – Boxplots to evaluate the relative mid-range error for M1 regarding Figure 4.19 a SNR and Figure 4.19 b sub-sampling. Same for M2 with Figure 4.19 c SNR and Figure 4.19 d sub-sampling.

The following comparison includes the reduced correlation matrix, but this time in combination with the noise waveform consisting of randomly weighted spectral components (M3). The measurement M4 consists of a random measurement matrix projecting a chirp waveform to several observations. For both, M3 and M4, the low reconstruction error is remarkable with its close-to-zero characteristic, even for SNRs below zero and sub-sampling rates below 20 %. In contrast to M3 but same as M2, the relative error drops not gradually but shows a clear cut between reconstruction errors that are close to zero and errors that indicate a performance far beyond feasibility. While the reduced correlation matrix in combination with random noise apparently provides accurate results, see Figure 4.20 a and Figure 4.20 c, the results for a linear chirp keep a remaining error offset such as depicted in Figure 4.20 b. Also in Figure 4.20 d a remaining error in relative range exists, but only for very low SNR and subsampling levels.

The consistency in the finding of the remaining error offset for M4 reveals while analyzing the according boxplot for M4 in Figure 4.21 c and Figure 4.21 d. There, the statistics are plotted regarding the SNR (Figure 4.21 c) and sub-sampling (Figure 4.21 d) dependency for a target distance representing the mid-range, i.e. in that case 150 m. Apart from the error offset, the SNR dependent boxplot shows only a slightly increased variation from the mean error compared to its equivalent M4 in Figure 4.21 c, that in addition features a zero mean in the relative error for any SNR and sub-sampling rate. While several outliers occur for an SNR of −6 dB, there is almost no variation for higher SNR level. Regarding sub-sampling, the results indicate a minimum sub-sampling rate of at least 18 % for M3 and at least 22 % for

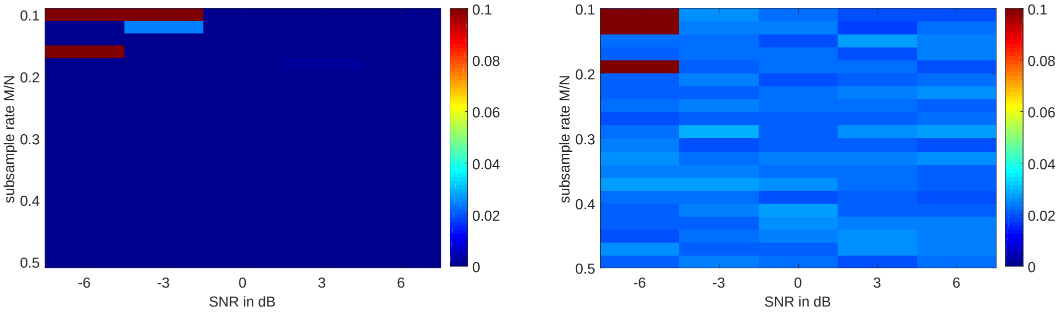

(a) M3: short range

(b) M4: short range

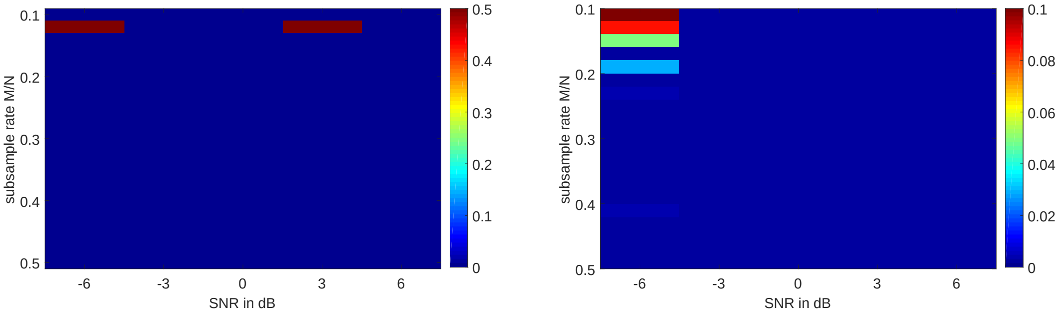

(c) M3: long range

(d) M4: long range

Figure 4.20 – Relative error in range depending on sub-sampling rate in percent and SNR level. Short range performance is represented with a target located at 30 m for Figure 4.20 a M3 and Figure 4.20 b M4. Long range performance is tested with a target at 270 m for Figure 4.20 c M3 and Figure 4.18 d M4.

the chirp implementation M4.

A numerical comparison is performed in Table 4.2 with the sub-sampling rates $r = 0.21,\ 0.31$ and 0.41, because this is the sub-sampling region, where the error figures change most drastically. The SNR of -3 dB represents a case far below SNR levels where commercial radar is still operational, which ranges approximately between 10 dB and 20 dB. Those assumptions on automotive radar propagation channels are approximated by evaluating the results at 6 dB, thus still being below usual SNR levels but also covering regions, where the error figures show major improvements. Error figures comprise additional error values apart from the previously addressed relative error, that are captured in Table 4.2. Namely, it contains besides relative errors also absolute errors and standard deviation for both, absolute error σ_{abs} and relative error σ_{rel}. Values for short range and long range representatives are extracted since the boxplots in Figure 4.19 and Figure 4.21 refer already to that range. The values show how standard deviation correlates with the magnitudes of the error figures, thus indicating that valid conclusions are possible based on the relative and absolute error distribution.

The measurement setup that uses a linear chirp in combination with random

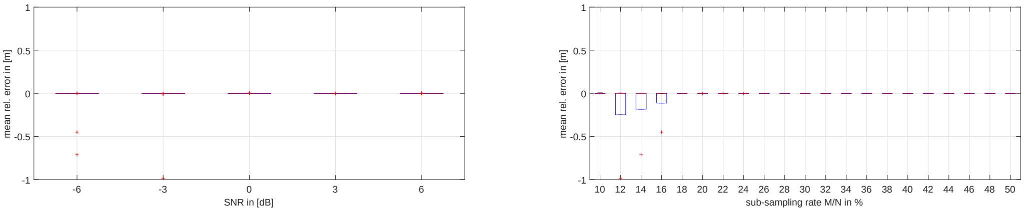

(a) M3: SNR (b) M3: sub-sampling

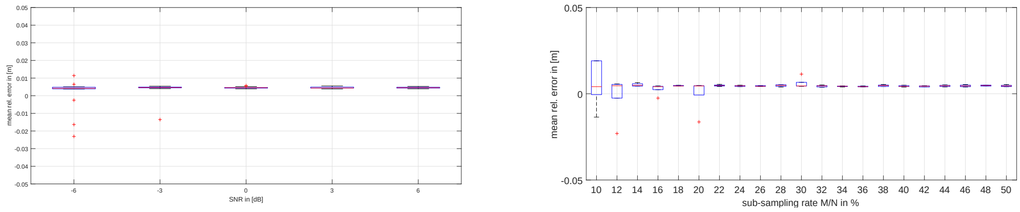

(c) M4: SNR (d) M4: sub-sampling

Figure 4.21 – Boxplots to evaluate the relative mid-range error for M3 regarding Figure 4.21 a SNR and Figure 4.21 b sub-sampling. Same for M4 with Figure 4.21 c SNR and Figure 4.21 d sub-sampling.

matrices shows a stable behavior throughout all parameters including a constant offset of approximately 0.7 m such as indicated already during boxplot analysis. Comparing results for different sub-sampling rates shows drastic improvements for M1 after increasing the amount of correlations by only 10 %. Increasing the SNR to 6 dB improves the reconstruction results towards the low error figures of M2 and M4, while diminishing the importance of sub-sampling as well. M2 finally shows the best performance among the acquisition and reconstruction configurations listed in Table 4.2.

Measurements for M3 are left out in the table, as they turned out to have error metrics that are mostly zero and otherwise way lower than turned out from the other measurements M1, M2 and M4. Therefore, purely numerical comparisons do not give a deeper understanding of error characteristics for M3. However, comparing M1 and M3 reveals the effect of the noise waveform on reconstruction results. Both measurements use reduced correlation matrices, which are easier to handle in real world implementations given the possibility of significant reduction in correlation effort. The only difference in the shape of the transmit and hence correlation waveforms consists of the weighting of the spectral components instead of homogeneously incorporating all spectral components within the allocated radar bandwidth. Although the waveforms differ only slightly, the impact on the error figures is significant as revealed in Figure 4.22. While there are only few outliers for an SNR below zero for M3 in Figure 4.22 c, the results for M1 show comparable confidence values only above a 0 dB level, while still featuring outliers (Figure 4.22 c). The dependency on sub-sampling rates as depicted in Figure 4.22 b for M1 and Figure 4.22 d for M3

Table 4.2 – Proof-of-concept error metrics

	-3 dB			6 dB		
30 m	M1	M2	M4	M1	M2	M4
e_{abs}	2.8341	0.0034091	0.73295	0.040909	0.0034091	0.69205
	0.15682	0.0034091	0.56932	0.036364	0	0.56591
	0.045455	0	0.70909	0.029545	0	0.61023
σ_{abs}	22.809	0.021561	0.40462	0.55309	0.021561	0.43931
	12.783	0	0.38925	0.3432	0	0.45126
	0.1923	0	0.39207	0.34433	0	0.43451
e_{rel}	0.09447	0.00011364	0.024432	0.0013636	0.00011364	0.023068
	0.0052273	0.00011364	0.018977	0.0012121	0	0.018864
	0.0015152	0	0.023636	0.00098485	0	0.020341
σ_{rel}	0.76029	0.0007187	0.013487	0.018436	0	0.014644
	0.42609	0.0007187	0.012975	0.01144	0	0.015042
	0.0064101	0	0.013069	0.011478	0	0.014484
270 m	M1	M2	M4	M1	M2	M4
e_{abs}	22.464	0.0034091	0.6	0.046945	0.0034091	0.69545
	5.3773	0	0.67159	0.022727	0	0.74318
	2.4	0	0.57955	0.011364	0	0.82841
σ_{abs}	60.902	0.021561	0.443	0.2976	0.021561	0.46914
	33.75	0	0.42943	0.29511	0	0.45379
	17.064	0	0.42538	0.19974	0	0.40072
e_{rel}	0.083159	1.262e-05	0.0022222	0.00017378	1.262e-05	0.0025758
	0.019906	0	0.0024874	8.4133e-05	0	0.0027525
	0.0088844	0	0.0021465	4.2066e-05	0	0.0030682
σ_{rel}	0.22545	7.9815e-05	0.0016407	0.0011017	7.9815e-05	0.0017375
	0.12494	0	0.0015905	0.0010925	0	0.0016807
	0.063167	0	0.0015755	0.0007394	0	0.0014841

shows the high potential in reducing the amount of correlations, especially regarding M3.

4.3.3 Evaluation and Discussion

The overall conclusion of the proof-of-concept is that all applied CS methodologies result in a satisfactory reconstruction performance during low SNR levels while significantly reducing the amount of correlation filters or random measurements. Nevertheless, detailed error figures show strong variations within the implemented approaches, especially when it comes to receive signals with very low SNRs or low sub-sampling rates. There, the diversity and need for matrix design adjustments in

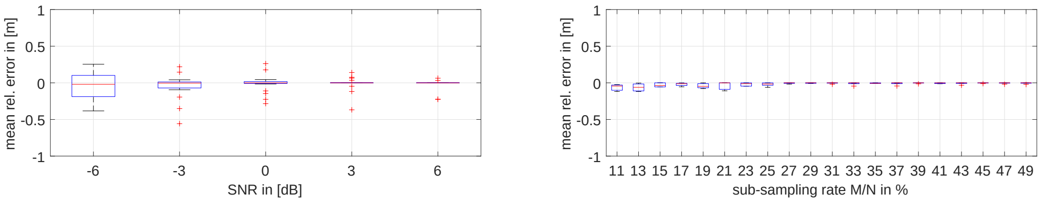

(a) M1: short range (b) M1: long range

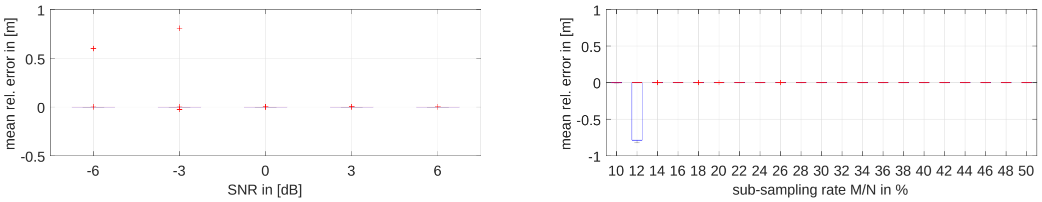

(c) M3: short range (d) M3: long range

Figure 4.22 – Boxplots to evaluate the relative error for M1 regarding Figure 4.22 a SNR at short range and Figure 4.22 b sub-sampling at long range. Same for M3 with Figure 4.22 c SNR for short range and Figure 4.22 d sub-sampling for long range.

different scenarios that impact the receive signal becomes evident, whereas correlation and random matrices turn out to differ in robustness. Comparing white noise, random noise and linear chirps shows that the selected waveform has an even if not higher impact on the reconstruction success than the measurement matrices. This finding reveals the limitation of coherence as a metric for feasible measurement matrices as it does not capture the actual characteristics of a transmit waveform but only its signal model if it captures it at all. Otherwise, only the mutual coherence of the measurement matrix is captured ignoring real signal features, that may even vary during measurements, completely. In contrast, the RIP incorporates the relation between matrix and signal characteristics, thus enabling to determine benchmarks based on matrix-signal interdependencies.

Using a correlation receiver introduces the issue of increasing the coherence between measurement signals and received signal, thus impacting the reconstruction capability of the system. Accordingly, the error figures of M1, which uses a white noise pulse, are more prone towards a decreasing SNR and tend to require more correlations than the other waveforms to provide similar low relative or absolute errors. In contrast to M1, the relative error of M3 that uses random noise pulses is almost not influenced at all by low SNR levels. The improvement of the error figures is directly connected to the random weighting of the spectral components, as it makes each pulse unique and therefore distinguishable. The relative and absolute error in range does not decrease gradually but abruptly. This indicates the moment, where the matrices meet CS requirements regarding RIP. Since a matrix does not change its characteristics, the mutual coherence remains the same and is independent from actual shapes of the receive signal. Therefore, mutual coherence is not feasible as stand-alone criterion to determine any conclusions about the reconstruction process. Hence, the mutual coherence is not feasible as stand-alone metric, but needs in addition the RIP to incorporate real signal characteristics such as noise and distortions. This shows, at which moment the initially feasible measurement matrix needs to be adapted to signal variations by increasing the number of measurements in the most simple case.

The dependency from the similarity between measurement signals and receive signal becomes not only obvious in the comparison between M1 and M3, but also M1 and M2. Differently to the previous comparison, here the pulse remains the same but instead of a reduced correlation matrix a random matrix is used as measurement matrix. According to Figure 4.18 b and Figure 4.18 a a sub-sampling rate of 15 % is sufficient for a successful range reconstruction using random matrices instead of reduced correlation matrices. Nevertheless, in practical implementations it is more challenging to implement a hardware-based pseudo-random generator that reproduces the measurement signals perfectly at the receiver side or alternatively storing the complete measurements matrix than designing several delay lines.

Comparing M2 with M3, the boxplots in Figure 4.19 c and Figure 4.21 a show the same behavior, that suggests SNR as a minor impacting factor to both systems. But also the behavior regarding sub-sampling is almost the same such as depicted in Figure 4.19 d and Figure 4.21 b. Hence, using a random noise modulated pulse results in a comparable reconstruction performance including the favorable features of a random measurement and reduced correlation acquisition approach.

M4 uses a linear chirp instead of random measurements. Apart from the remaining constant offset that is almost equal for all ranges, sub-sampling rates and SNRs (see Table 4.2), the reconstruction results appear reliable for a safe operation. Nevertheless, M3 features lower deviations according to the boxplot in Figure 4.21 b than M4 in Figure 4.21 d. While comparing the deviations for different SNRs, M4 shows in Figure 4.21 c more outliers and higher variations than M3 in Figure 4.21 a.

In summary, M3 with its random noise pulse and the reduced correlation receiver fulfills the CS requirements on coherence between signal and measurement signal, whereas the pulse modulation turns out to be a crucial part in a stable correlation receiver relying on CS. At the same time, the correlation approach results in less hardware adjustments than a random measurement implementation. The correlation matrix with not completely incoherent elements reflects the fact, that analog hardware always introduces correlation to transmit and receive signals, which is sensible to be taken into account while designing the measurement and reconstruction matrix. Based on these findings, the radar emulation introduced in the following Chapter 5 uses the methodology of M3. It will be analyzed, how actual RF hardware with focus on physical characteristics of the applied antenna arrays, affects the reconstruction methodology.

5 Demonstrator and Experimental Results

This chapter contains practical implementations to demonstrate several performance aspects of radar and noise radar in particular. Due to chip manufacturing and intellecutal property rights, raw radar signals are hardly accessible in commercial radar systems. Since manufacturing a radar signal processing chip was not the scope of this work, therefore the demonstrator consists partially of emulated components. For validation purposes a LFMCW radar system was set up in parallel to ensure meaningful conclusions from the noise radar demonstrator.

The heart of the demonstration is a physical radar sensor mounted on a FPGA development board and allowing access to low-level beat signals. As such it is the reference version for a phenomenological radar sensor model that can be used in a very versatile way allowing physical emulation of the proposed noise radar concept. For increasing realistic sensor behavior, data-driven weather models are developed and applied. The extracted information is used to determine typical changes in the receive signal characteristic corresponding to different weather conditions that the radar radome is exposed to. The work flow to establish a demonstrator for analysis using a sensor emulation is visualized in Figure 5.1. The orange colored blocks indicate real world components, while and blue-colored blocks highlight virtual components. Green blocks represent the semi-virtual validation process.

The chapter structure reflects the block structure in Figure 5.1. It starts with an introduction and parameter description of the physical radar sensor. The design of performed test measurements is then introduced and the measurements are analyzed regarding weather conditions affecting the radar radome. The implementation

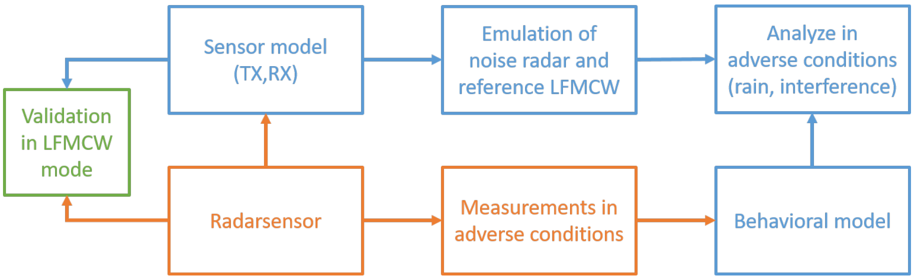

Figure 5.1 – Demonstration work flow: Real world radar sensor and measurements (orange) are used to generate virtual models and systems (blue). The real and virtual radar are validated with point-wise measurements in LFMCW mode (green).

of a phenomenological radar sensor simulation, that is validated by point-wise measurements, follows afterwards. The phenomenological radar sensor model is used to emulate the CS noise radar and evaluate it regarding reconstruction performance and reliability in noisy or interference-affected propagation channels.

5.1 LFMCW Radar

In Section 2.1.2 the underlying principles of LFMCW radar systems are presented. Here, a radar sensor is described that serves as reference and benchmark for a phenomenological sensor simulation. After developing the radar sensor model according to the parameters of the radar sensor, the model is validated against real-world measurements with focus on the range profile, since the objective of the CS noise radar is to improve the range reconstruction. Besides validation measurements, the hardware radar system is used for measurements related to weather and environment conditions, specifically rain effects on the radome, that lead to data-driven behavior models of adverse environmental conditions. The parametrization of the development board that is used to operate and configure the radar sensor, is limited by the contradicting optimization goals of resolution and range. Acceptable trade-offs need to be tailored to individual target applications.

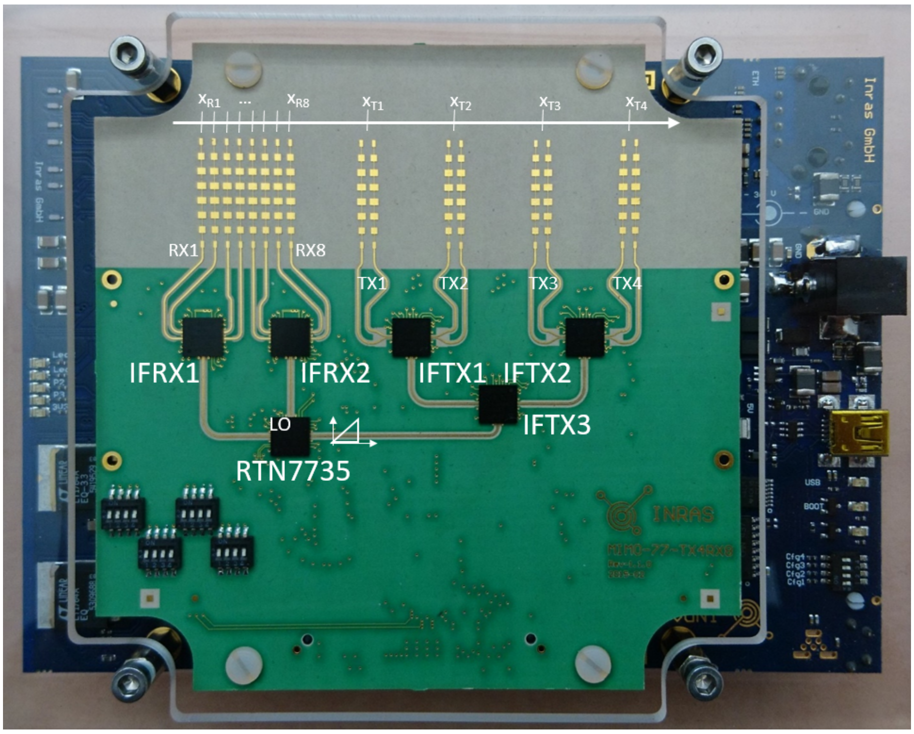

Figure 5.2 – INRAS' Radarbook with mounted 77 GHz RF frontend

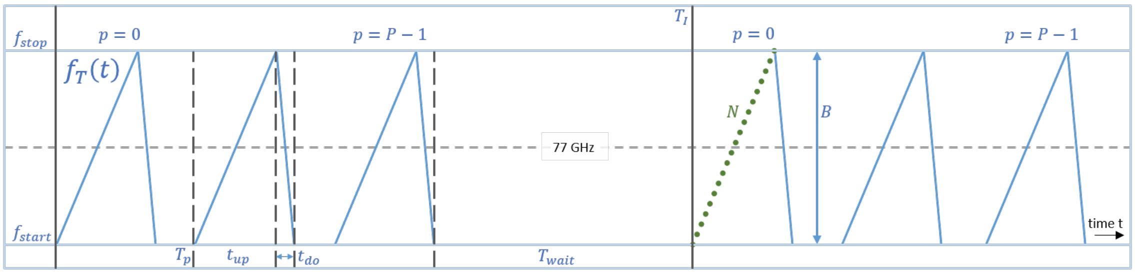

Figure 5.3 – Configurable chirp parameters on radar development board

5.1.1 Radarbook Parametrization

The reference LFMCW radar system that was used for real world measurements was the radar development platform Radarbook from the Austrian company INRAS, depicted in Figure 5.2. The corresponding data sheet is attached in Chapter 6. The benefit of this radar development platform is not only a fully working 77 GHz radar system that almost allows out-of-the-box measurements, but especially the access to the beat signal at the intermediate frequency. Commercial radar systems often return preprocessed target and object lists that are extracted with signal processing that is tailored to particular applications such as BSD or ACC. In Figure 5.2 some essential components of the radar frontend are annotated, that are described in more detail in Chapter 6. RX marks the eight linear receive antenna arrays, each consisting of eight patch elements. The antenna elements as well as the antenna arrays are spaced with $\lambda/2$. On the right side of the RF frontend are four transmit antennas TX placed with mutual distance $7\lambda/2$. As a result, a virtual antenna of up to 32 channels can be implemented with this multiple-input multiple-output (MIMO) frontend, whereas the transmit antennas are addressed sequentially.

Configuration and beat signal acquisition is performed by a remote host PC using the provided MATLAB or Python class. The core of the radar sensor is the RCC1010 chip from Infineon used for transmit signal configuration, generation and acquisition. Signal configuration is restricted to chirp configuration. The setup allows to vary linear chirps in the frequency range between 76 GHz to 81 GHz with a maximum bandwidth of 4 GHz, thus covering the full allocated frequency band of automotive radar. In order to adapt the radar platform to different applications in different scenarios, the parameters of the transmit chirps can be configured by the user. Afterwards, the signal processing of the sampled beat signal is completely programmable by the user, thus allowing a versatile radar operation. Different environments, e.g. intersections or highways such as described in Table 2.4 require adaptation of the transmit chirp parameters in terms of covered bandwidth and chirp timing to fulfill different application specifications such as resolution or range. Of course, the parametrization is not only subject of compromises to meet different and even opposing criteria, but is in addition restricted by hardware. Considering the transmit signal as a time-dependent frequency signal model $f_T(t) = \frac{f_{stop}-f_{start}}{t_{up}} \cdot t$ according to (2.16), the frequency is linearly increased from the start frequency f_{start} to the stop frequency f_{stop} during the rise time t_{up} such as depicted in Figure 5.3, where configurable chirp parameters are annotated for two chirp trains, each lasting for the interval time T_I. In most automotive radar implementations, the bandwidth $B = f_{stop} - f_{start}$ is allocated around the center frequency $f_c = 77$ GHz. A chirp interval consists of N_p chirps. The number of chirps can be raised to at most $N_p = 256$ chirps. The number of chirps and therefore slow time samples, defines the resolution $\mathit{\Delta} v_p$ in velocity direction.

$$\mathit{\Delta} v_p = \frac{2|v_{p,max}|}{N_p} \tag{5.1}$$

The velocity resolution depends on the maximum velocity $v_{p,max}$. The pulse period T_p, which corresponds to the slow-time sampling rate T_p, defines the maximum relative velocity $v_{p,max}$, which is resolvable with the radar configuration. While slow-time sampling refers here to the pulses, fast time refers to values within a pulse. The velocity v_p and therefore $v_{p,max}$ depends among others on Doppler frequency f_D and the slow time sampling rate T_p such as stated in (5.2). The maximum Doppler shift $f_{D,max}$ is limited to the maximum bandwidth of the system, hence $f_{D,max} = B/2$.

$$\begin{aligned} v_p &= f_D \frac{c_0 t_{up}}{B} \\ v_{p,max}\left(f_{D,max}\right) &= \frac{c_0 t_{up}}{4T_p} \end{aligned} \tag{5.2}$$

The Doppler time shift only needs to be considered if either the relative velocity of a reflecting target is significant or the time interval T_p between two pulses is sufficient to result in a notable Doppler shift. Hence, targets moving with same speed will not introduce any Doppler frequencies. Additional timing limitations regarding T_p originate from required configuration time between two chirps equal to the configuration time T_{cfg} of 50 µs, which needs to be considered while setting the up-chirp duration t_{up} and down-chirp duration t_{do}. The sum of the up-chirp, down-chirp and the configuration time provide the minimum duration of $T_p = t_{up} + t_{do} + T_{cfg}$. After all N_p chirps are transmitted, a minimum initialization time of $T_{init} = 2$ ms is required before the next train of chirps can be transmitted. Hence, a chirp interval needs at least the time

$$T_I = N_p T_p + T_{init} \ . \tag{5.3}$$

Parameter selection of up-chirp duration t_{up} and number of fast time samples N.is restricted to the maximum sampling frequency of the ADCs. While all ADCs are enabled, the overall sampling frequency equals 80 MHz resulting in a sampling frequency $f_{AD} = 10\,\mathrm{MHz}$ per receive channel. Hence, the fast time sampling frequency f_s of individual chirps, which is restricted by ADC capabilities, is computed by

$$f_s = \frac{N}{t_{up}} \ . \tag{5.4}$$

As indicated with N green dots, replacing one continues line of a ramp in Figure 5.3, sampling only takes place during the up-chirp. During down-chirps, signal acquisition remains in idle mode. With the maximum expected necessary sampling frequency of $f_s = 2f_{r,max}$ the required sampling frequency still needs to be decreased to include cascaded-integrator-comb-filter (CIC) filter of order N_{div} for the sake of system robustness. Since the transfer function of the CIC filters is adapted to the ADC clock dividers, the denotation of the filter order and clock divider are the same, i.e. $N_{div} = \lfloor \frac{20\text{ MHz}}{f_s} \rfloor$. It needs to be ensured that the sampling frequency f_s is less than 20 MSPS, which corresponds to the maximum sampling rate at each intermediate frequency (IF) channel. The number of fast time samples N results from the chirp rise time t_{up} and the realized sampling frequency $fs = \frac{20\text{ MHz}}{N_{div}}$, see (5.5). It should be noted, that the minimum applicable ramp duration t_{up} is 71 µs.

$$N = \left\lfloor t_{up} \frac{20\text{ MHz}}{N_{div}} \right\rfloor \tag{5.5}$$

For radar perception, the maximum unambiguous range r_{max} in (5.6) and the range resolution $\varDelta r$ are among the most relevant parameters.

$$r_{max} = \frac{\varDelta_{R,res} N_f}{2} \tag{5.6}$$

With the range resolution

$$\varDelta_{R,res} = \frac{c_0}{2B_c} \tag{5.7}$$

the maximum frequency related to range $f_{r,max}$ is calculated by using the chirp rate $\alpha = \frac{B}{t_{up}}$ and maximum round-trip time $t_{r,max}$, as

$$f_{r,max} = \frac{B}{t_{up}} \cdot \frac{2r_{max}}{c_0} = \frac{B}{t_{up}} \cdot \frac{N\varDelta_{R,res}}{c_0} = \frac{N}{2t_{up}} \ . \tag{5.8}$$

In conclusion, not only range resolution $\varDelta_{R,res}$ as given in (5.7) restricts the maximum unambiguous range r_{max} in (5.6), but also the number of samples N that is constrained by ADC sampling rate. In (5.9) the dependency of the required number of samples N from the quotient of the maximum distance and the range resolution is stated explicitly.

$$\begin{aligned} N &= \frac{r_{max}}{\varDelta_{R,res}} \\ &= r_{max} \cdot \frac{2B}{c} \end{aligned} \tag{5.9}$$

(a) Radar with host PC (b) Measurement setting

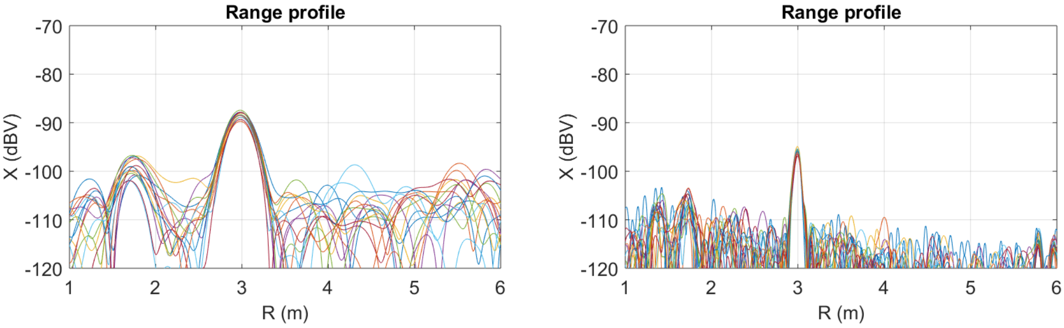

(c) Range profile 1 GHz (d) Range profile 4 GHz

Figure 5.4 – Corner reflector measurements: Figure 5.4 a shows the Radarbook and the host PC and Figure 5.4 b depicts the measurement setting with a corner reflector placed 3 min front of the radar. The range profile is displayed in Figure 5.4 c for 1 GHz bandwidth and in Figure 5.4 d for 4 GHz bandwidth.

Measurements with a corner reflector placed 3 m in front of the radar sensor such as depicted in Figure 5.4, demonstrate how bandwidth affects range resolution, but also peak power. The same scenario was measured with a bandwidth of 1 GHz and 4 GHz and all 32 virtual antennas were processed by applying a FFT to the range profile. The range profile shows signal level intensities depending on distance. It contains all virtual antennas, i.e. RX-TX combinations, hence several lines are found in Figure 5.4.

In addition to maximum ranges and velocities, the question of minimum ranges also needs to be answered. Depending on mechanical antenna dimension d and the wavelength λ of the carrier frequency, far-field and near-field regions are defined for radar operation. According to (2.43) the transition between near field and far field happens at the minimum far field range $r_{ff,min} \geqslant \frac{2d^2}{\lambda}$. Many radar signal processing assumptions regarding signal propagation do not hold below that range and therefore near field reflections need to be considered. The Radarbook features four transmit antennas that are switched on sequentially and that are spaced by $7\lambda/2$. Together with the fix dimension of the receive antennas that are operated simultaneously, the begin of the far field region depends on the active transmit antenna. According to

Chapter 6, the antenna dimension alters with [25.614 39.250 52.887 66.523] mm. The variation in antenna dimension results in minimum far field ranges $r_{ff,min}$ between 34 cm and 2.3 m. These individual minimum far field ranges for each antenna are sketched in Figure 5.5.

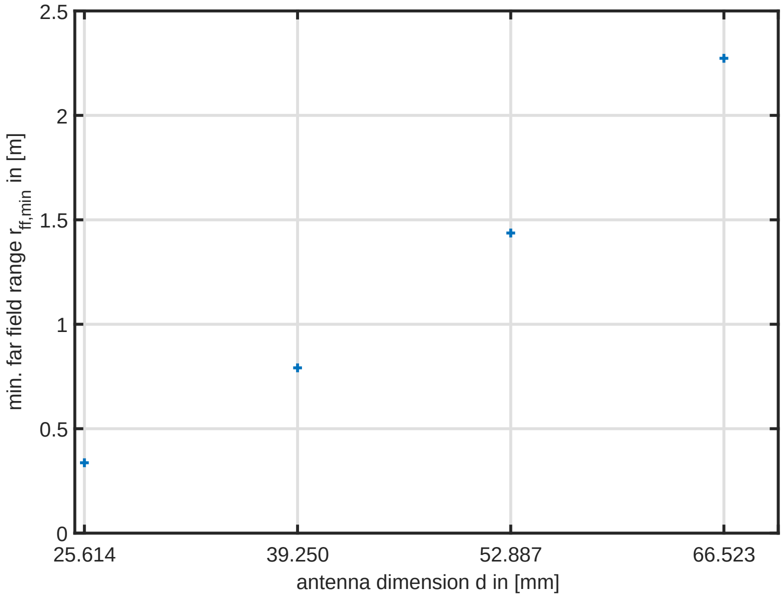

Figure 5.5 – Begin of far field region for different TX antenna postions.

5.1.2 Measurement of weather effects

In general, three categories of interfaces can be distinguished that are impacted by adverse weather and environment conditions. Namely, those are the radar or specifically its radome, the propagation channel and reflecting targets. In Section 2.3.2 adverse weather and environment conditions were discussed with the result, that specific rain attenuation only becomes important in heavy storm events as automotive radar covers only short radar ranges compared to other radar applications. However, radome impacting effects may cause severe attenuation of the radar backscatter that even outweighs the changes in reflectivity of target surfaces. Therefore, the focus in this work lies on effects occurring in the ultimate vicinity of the radar affecting the radome. Rain drops covering the radome attenuate the receive backscatter before it reaches the receive antennas and additionally act as lenses, depending on their shape. Besides static attenuation as a result from partial or complete radome water coverage, dynamic variations caused by radome drying or non-continuous events need to be distinguished in case there are variations within a radar sweep. The aim is not only to consider effects resulting from adverse weather conditions, but also to develop models

(a) Radar mounting (b) Target location

Figure 5.6 – Experiment setup for static measurement of rain effects: Figure 5.6 a radar mounted on railing, Figure 5.6 b geometry of targets and radar

that mimic realistic adverse weather conditions. These models generate stimulation signals that can either be applied in a holistic environment-sensor simulation such as in [78] or applied directly on a real radar sensor. Thus enables a faster sensor validation since adverse weather conditions are hardly reproducible and measurement campaigns cannot be planned according to unpredictable environment conditions. Depending on rain drop coverage or water film on the radar radome, individual attenuation models can be observed during measurements. Attenuation is not stationary, but it changes depending on the rain intensity, i.e. the change of the rain drop coverage on the radome, and the intensity of other water sources, such as splash water. A stationary attenuation can be only observed, if the water coverage on the radome remains constant. Otherwise, a drying process on the radome can be observed on the radome attenuation depending on time that shows how the receive signal level recovers from adverse weather attenuation. In summary, overall radome attenuation consists of specific rain attenuation $a_s(t)$, attenuation from constant water coverage $a_{cwc}(t)$ and attenuation from dynamic water coverage $a_{dwc}(t)$, which comprises singular events and dynamic change of intensities. The specific rain attenuation $a_s(t)$ results from the atmospheric propagation channel attenuation. As most rain events are lasting for a longer period of time and rain events can be treated separately, specific rain attenuation is assumed as a constant value a_s as stated in Table 2.6 in Section 2.3.1. The other parameters, i.e. static and dynamic attenuation, were determined from measurements. In typical automotive scenarios and applications, where a radar is mounted on a moving platform, there are many environment parameters and effects that impact radar backscatter and therefore results of signal processing. Thus makes it hard to isolate weather effects from other influences during realistic test drives. However, a well-defined and controlled environment and scenario enables the separation of weather and environment influences from other effects, such as Doppler and multi-path propagation. Typical dynamic scenarios were analyzed in order to extract individual elements that are part of a complete weather and environment scenario. Based on the analysis, experiments were designed that reflect particular effects with focus on radome effects. Concentrating on the radome results from understanding that interface as the most critical one, even compared to experimental changes of the RCS by temporal water coverage of an object. A constant water coverage on the radome occurs, when the drying process of either a water film or single rain drops is prevented by a constant source of a water stream or water drops. The prevention of stopping the drying process of water drops needs to be understood as a statistical process, i.e. for each drying water drop there will be a new water drop. In that scenario, the attenuation from the constant water coverage is also assumed to be static $a_c wc$.

Splash water is a sum of highly time variant single events. Assuming P events of the attenuation process $a_{sw,p}(t)$, each delayed by individual point in times τ_p, it can be stated with the individual static scaling factor α_p as

$$a_{sw}(t) = \sum_{p=0}^{P-1} \alpha_p \cdot a_{sw,p}(t - \tau_p) \tag{5.10}$$

The attenuation from the dynamic water coverage $a_{dwc}(t)$ reflects the change of the water coverage on the radome. After an initial water coverage status and an according initial attenuation $a_{i,wc}$, the radome can be either subject to a drying process, reflected by the time variant attenuation $a_{dp}(t)$ or a constant increase of the water reflected by the time variant attenuation $a_{wp}(t)$. A constant increase in water coverage results in a time process of attenuation that differs from the time process of attenuation of the drying, therefore it needs to be taken into account separately. The overall attenuation resulting from a dynamic water coverage produces (5.11). It factors in the points in time, when the different processes start with τ_{dp} for the drying process and τ_{wp} for the process that increases the water coverage.

$$a_{dwc}(t) = a_{i,wc} + a_{dp}(t - \tau_{dp}) + a_{wp}(t - \tau_{wp}) \tag{5.11}$$

Unpredictable weather models in combination with various environment effects including multi-path propagation, micro-Doppler and non-stationary propagation channels make it hard to identify with a high fidelity weather induced effects within the backscatter from real driving maneuvers. Nevertheless, real field measurements served as source for creating static scenarios that isolate individual effects and quantify their impact using measurements.

The experiment setup consists of the radar such as described in Section 5.1.1, which is supported by a Raspberry Pi camera in order to evaluate the measurement results. Together with the radar, the camera is mounted in a water-proof installation box that serves on the one hand as a radome and on the other hand as a housing for all environment perception sensors and a Raspberry Pi taking over the role of a controller. As depicted in Figure 5.6 a, the radar box, which refers to the environment sensor configuration placed in one housing with the radar, is mounted on a railing.

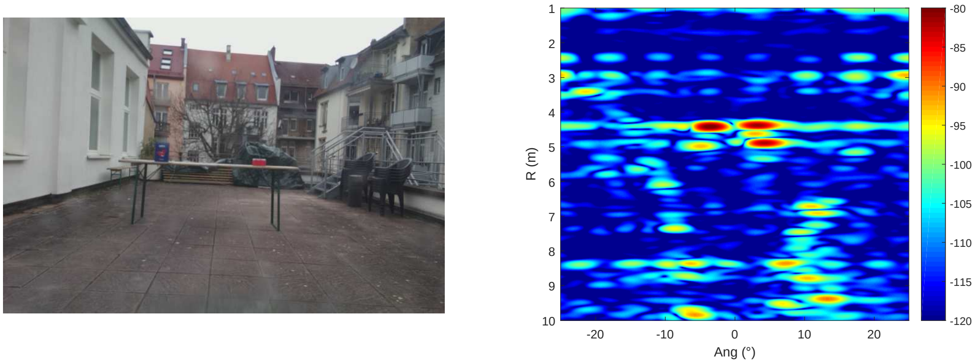

(a) Camera: Dry (b) Radome: Dry

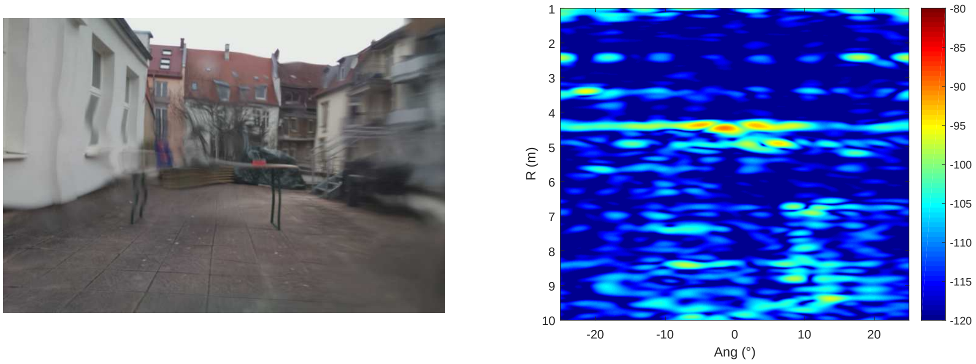

(c) Camera: medium wet (d) Radome: medium wet

Figure 5.7 – Different constant attenuation due to radome water coverage

Static targets of different shapes and sizes were placed in front of the radar at an approximately same height as the radar. With a distance of 85 cm to the ground, the intensity of ground clutter within the ultimate vicinity of the radar is mitigated. The experiments were conducted for different target distances and repeated several times, while keeping the height and the mutual distance in between the two used targets constant. Both targets are metallic, but one target has a rectangular and the other a cylindrical shape. In Figure 5.6 the experiment setup is depicted from the perspective of the targets.

Each individual measurement was performed for several minutes and repeated several times. The radome was moistened in different intensities using a water can in order to realize constant thick water films as well as an aerosol for application of water drops. In an analogous manner, the targets were humidified.

For evaluation, the range-azimuth map was considered and annotated closely to the camera pictures that were recorded in parallel with the co-mounted Raspberry Pi camera. A comparison between camera and range-azimuth pictures supports a visual impression of the water coverage affecting the radome. For the identified peak levels assigned to individual scenario targets depicted in Figure 5.7 a, the variation is evaluated for different conditions affecting the radome. The range-azimuth map in Figure 5.7 b is focused on the target position. Besides the metallic targets also a part of the table causes an equally strong backscatter, so that there are three main peaks visible in the map. Initially, the radome in Figure 5.7 a and Figure 5.7 b is completely dry, which serves as reference for expected attenuations of the peak level. During the next measurement, the radome is partially covered with water, which already results in a significant blur of the camera image in Figure 5.7 c. There, the left target is already hard to recognize and localize for algorithm-based evaluation. In contrast, the targets are still good to recognize using radar perception in Figure 5.7 d, although the peak level dropped significantly by approximately 6 dB to 10 dB. Besides the attenuation, the outlines of the peaks differ compared to measurements with a dry radome in a way that it might look like split into half. The reason behind it is the lens effect induced by the structure of the water drops and surfaces covering the radome. Hence, apart from attenuation also a meander-like structure similar to the camera picture can be observed on the range-azimuth map while the radome is exposed to water varying water streams. That is, because the local attenuation changes while the water is flowing down the radome. Increasing the intensity of the water stream running down the radome leads finally to an attenuation of approximately 20 dB in Figure 5.8 b. With the decrease of the signal strength reflected by the actual dedicated targets, extended targets become more present, as can be observed in the same graph. That is, because extended targets benefit from a wide reflecting surface and hence a higher propagation channel diversity, which increases the chances of less distortions during signal propagation. Hence, the flanking wall to the left of the targets is still recognizable, besides of the fact that it has a larger surface being favorable for a high RCS. It should be noted that the extend of an object does not necessitate a high RCS, because the energy reflected back to the radar depends not only from the target dimensions but also from scattering characteristics as explained in Section 2.3.2. Although receive signal levels degrade significantly at a constant water stream, peaks can still be identified by using a-priori knowledge from dry or less impacted measurements. In contrast to the radar output, the camera picture is already completely blurred with unidentifiable objects. Accordingly, tracking objects can help to compensate single events of radome impacts. Depending on the surface structure of a radome, it takes some time until the perception recovers from additional attenuation due to radome water coverage. Figure 5.8 c and Figure 5.8 d shows a measurement only few seconds after stopping the application of a constant water stream. Here, the radome features an even surface and hence water flows down quickly. But due to various design choices, whereas the aim is to integrate the radome seemless in the front of a vehicle, the radome might include edges or other shapes, which allows the gathering of water. That might lead to a lasting impact on signal perception.

While analysis of the range-azimuth map reveals information about stationary at-

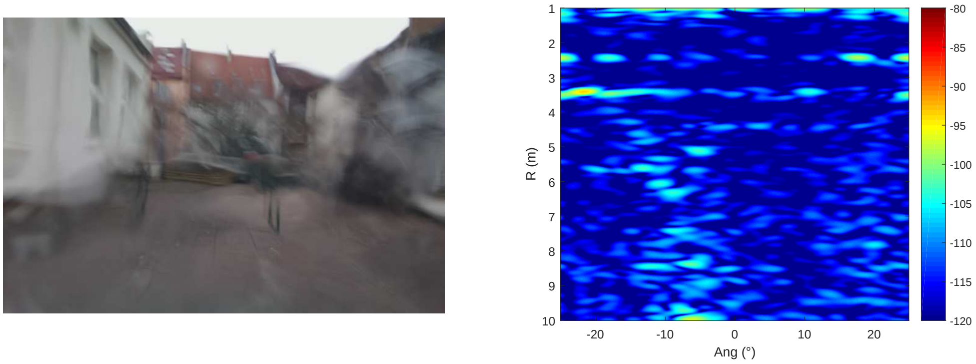

(a) Camera: intensive wet (b) Radome: intensive wet

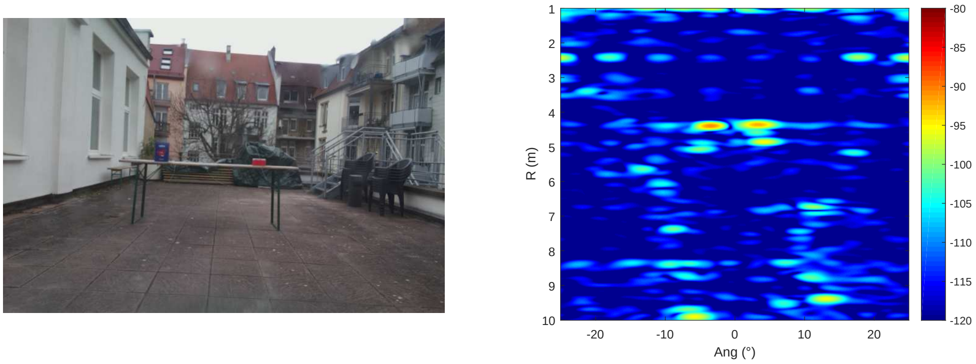

(c) Camera: drying (d) Radome: drying

Figure 5.8 – Different constant attenuation due to radome water coverage

tenuation, tracking the peak attenuation allows conclusions about dynamic processes. Hence, in Figure 5.9 the received peak levels in dB for both targets were tracked for different dynamic processes during measurement time in seconds. The first dynamic experiment in Figure 5.9 a shows peak levels for an initially dry radome. In an intermediate stage the peak level drops by approximately 10 dB before it goes down by 20 dB. After the waterstream stops, the peak level recovers with a characteristical exponential drying course shape. The initial peak of the blue marked peak level attenuation can be understood to be an outlier, which is unrelated to performed water experiments. Adverse incidents causing this characteristic peak attenuation course are for example incidents related to splash water. It can be seen as the most characteristic and significant incident that can occur.

Another dynamic measurement includes a higher diversity of events, i.e. random repetitive sprinkles on the radome. In Figures 5.9 b to 5.9 d several details of such a measurement are depicted. Since the measurement already started with water drops being on the radome surface, a variation in the peak level is already observed in the beginning of the measurement in Figure 5.9 b. After the radome dried within

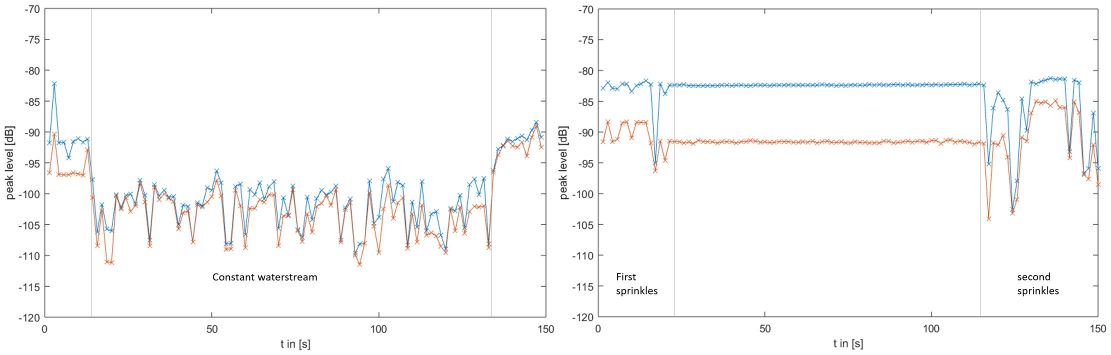

(a) const. waterstream (b) rep. water sprinkles

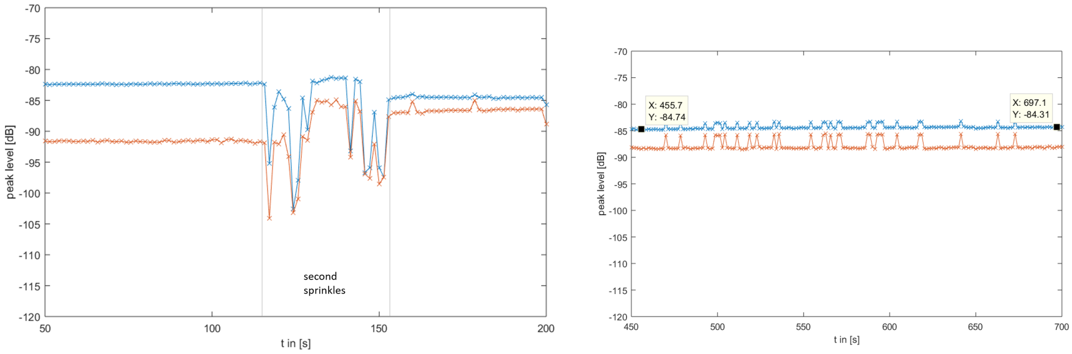

(c) rep. water sprinkles (d) drying

Figure 5.9 – Peak level attenuation of both targets (blue and orange lines) during various levels of water coverage on the radome: Figure 5.9 a Application of constant waterstream, Figure 5.9 b first water sprinkle incident, Figure 5.9 c second water sprinkle incident, Figure 5.9 d drying radome.

some seconds, the peak level for both targets remains constant until new sprinkles cover the radome indicated by a short but significant drop of peak level. Figure 5.9 c shows the detail of the impact that the application of sprinkles has on the radome revealing a clear temporal correlation between increase in attenuation and water application. After stopping the repetitive application of water sprinkles, the peak level remains basically constant with some outliers as shown in Figure 5.9 d, while the overall attenuation slowly decreases according to the time the radome needs for drying.

Accordingly, adverse weather conditions can be simulated in general by additional attenuation of 10 dB to 20 dB occurring in random time intervals. For generating stimulation models that go beyond that rule of thumb additional requirements and specifications are necessary. If an environment simulation that provides the simulation ground truth to a radar sensor offers the level of detail that contains local weather prediction models or road conditions comprising specific locations of puddles, realistic timing and intensity of splash and sprinkle models can be generated. If only a rain intensity is given but a radome structure and rain duration is known, the impact of rain on the radome and according increase in attenuation over time can be derived. Therefore, the testing objective needs to be specified properly to design an appropriate way of incorporating adverse weather conditions into a testing system without creating a misleading level of detail while using the measurement results for stimuli generation.

5.1.3 Radar sensor model

It is sensible to transfer prototyping as much into the virtual world as possible, especially during early development phases. Similar to the reasoning in Section 5.1.2 regarding the level of detail for virtual weather condition models, here the level of detail also depends from the overall testing goal that should be covered within the simulation. That is explained in more detail in [32]. While testing algorithms or functions may be performed sufficiently using radar data at a high level of abstraction, the evaluation of effects that occur at a low level of abstraction level requires a more detailed sensor modeling. Accordingly, the level of detail and hence the complexity needs to be adjusted to the testing objective, whereas not all components need to correspond to the same real-life fidelity. A modular sensor model allows early stage prototyping and development with a thoughtful deployment of resources, thus allowing early experimental designs. As the overall goal is to emulate a noise-modulated pulsed radar system to test compressive sensing signal processing such as introduced in Section 4.2.2, the characteristics of the physical radar sensor needs to be captured by a phenomenological sensor simulation. Electric parameters beyond noise figures can be neglected in order to perform tests on the function level. Also realistic simulation of the circuitry including timing or phase and voltage jitter can be neglected at early prototype development stage, since the feasibility depends mainly from correct sparsity assumptions and matrix design as discussed in Section 4.2.3.

Based on the real world radar system that was introduced in Section 5.1.1, a phenomenological radar sensor model has been developed that reflects physical characteristics of the radar sensor used by the Radarbook. In the following, functional components of the radar system are shown and its individual components are modeled and characterized, see also the author's further work in [91]. The phenomenological radar sensor model is validated in LFMCW mode against real-world measurements. Furthermore, the radar sensor model is connected to an exemplary environment simulation that realizes a high abstraction level with low complexity. As the validation of the radar simulation is performed in LFMCW mode, the simulated radar system in this section corresponds to LFMCW processing, which is only relevant in the left side of Figure 5.10 as explained in the following. On a high level perspective, the radar system simulation is subdivided in three main parts which can be assigned to the signal, sensor and environment domain. The signal domain consists of signal generation, acquisition and processing. Similarly, the environment domain

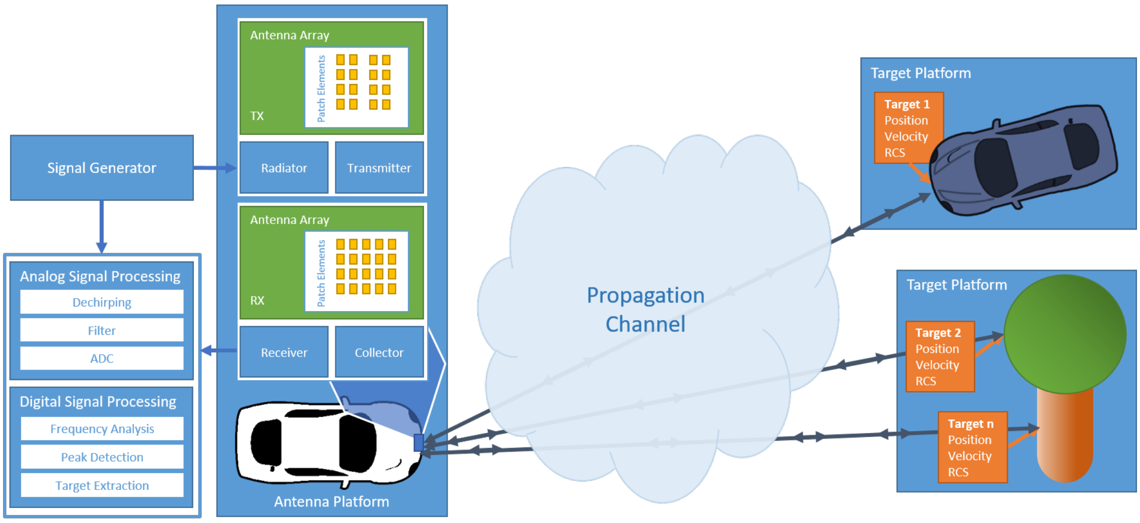

Figure 5.10 – Schematic of radar system simulation depicting signal domain on the left, sensor domain in the center and environment domain on the right.

includes everything that has an effect on the radar backscatter, i.e. propagation channel, reflecting targets or adverse environment conditions. The actual radar sensor simulation is integrated in between the signal and the environment domain and is the heart of the radar system simulation that will be used in the following to emulate the noise-modulated radar system. Accordingly, the sensor simulation module features the highest level of complexity and fidelity to the real world compared to the modules of the signal and the environment domain. The modular concept of the radar simulation allows to exchange individual components also within the three main domains of simulation, making it a flexible simulation platform for various applications.

Signal domain

The components belonging to the signal domain are depicted on the left of Figure 5.10. They are grouped to three blocks, namely the signal generator, analog and digital signal processing. The signal generator provides arbitrary transmit waveforms to the radar sensor model. For LFMCW radar systems the transmit waveform consists of linear chirp pulses that can be for example parametrized according to the signal generator of the Radarbook following the design rules in Section 5.1.1.

The transmit waveform is usually not only provided to the transmit antennas but also to the analog signal processing block that conatins the RF-frontend. During analog signal processing, the transmit waveform is compared to the receive waveform before the result is discretized using ADCs for further processing. The implemented simulation regards losses, noise figure and number of samples of a real system.

The analog signal processing block is followed by the digital signal processing block. The latter is exactly the same for the real and the simulated radar as the real radar signal is processed on the same host PC as the simulation. This is possible because the interface of the real and simulated radar are identical at the input of the digital signal processing block.

Environment domain

Simulation at environment level includes propagation channel characteristics, adverse weather and environment conditions and reflecting targets. The propagation channel is usually assumed to be an AWGN channel resulting in different SNRs at the receiver and can be set to one-way or two-way propagation. Different specific rain attenuation is included as path loss, that considers ambient temperature and humidity as well. In addition to the implemented LOSs paths also NLOSs can be taken into account. Adverse weather and environment conditions according to the modeling approach in Section 5.1.2 are also incorporated as part of the resulting SNR.

Targets are included as reflecting points that belong to objects within the simulated scenario. In default mode they are characterized by their position and velocity in $\{x, y, z\}$ direction and their RCS. While the velocity and RCS are assumed to be stationary, the position is updated after each pulse for every target. Target parameters can be either entered manually or by co-simulation with a dedicated environment simulation. The latter case might require an adaption to the environment simulation though in order to handle different output specifications, e.g. Doppler frequency instead of velocity or different coordinate systems.

Sensor domain

The highest level of detail is realized within the sensor domain by incorporating the physical dimensions of the Radarbook radar sensor into the simulation. Components that belong to the radar sensor model are depicted in the blue box of the antenna platform in Figure 5.10. All antennas are realized as microstrip antennas consisting of patch elements as atomic components. As depicted in Figure 5.11 a, a single patch element is modeled by its physical dimensions, width W_p, length L_p, and height h_p. In addition, the position f of the feed is specified. Also, the ground plane is considered with its two dimensional extents in terms of width W and length L. In the bottom left corner of the directivity plot in Figure 5.11 b, the tilt of the patch element is indicated, which corresponds to 90 deg according to an assumed mounting at the front grill of a car. But the actual information of the directivity plot that belongs to a single patch element consists of the gain that is obtained in azimuth and elevation direction. It depends on the physical patch, the ground plane dimensions, and the center frequency, which corresponds to 77 GHz. The 3D directivity is plotted in a $\{x, y, z\}$ coordinate system. Both, the transmit and receive antennas are implemented as linear arrays of eight single patch elements. While

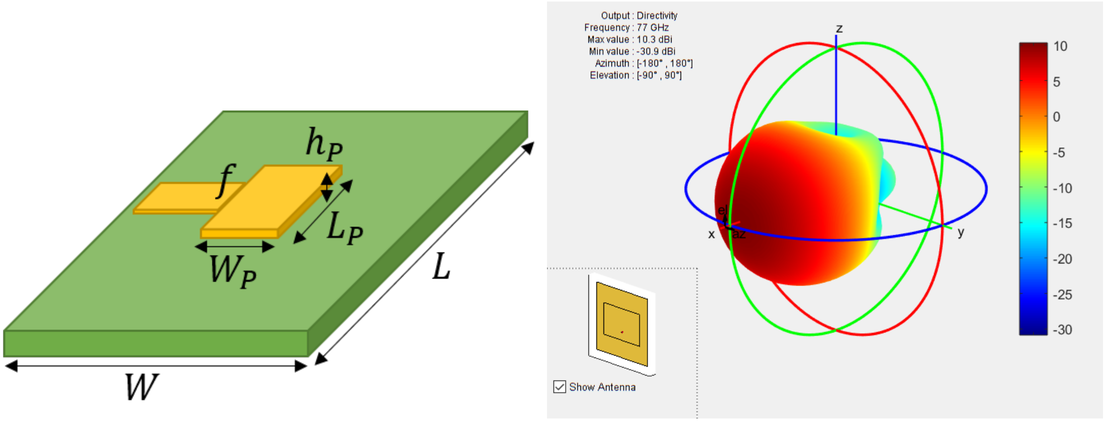

(a) Parameters (b) Directivity

Figure 5.11 – Microstrip patch element. In Figure 5.11 a the modeled parameters are visualized and in Figure 5.11 b the directivity of a single patch element is given.

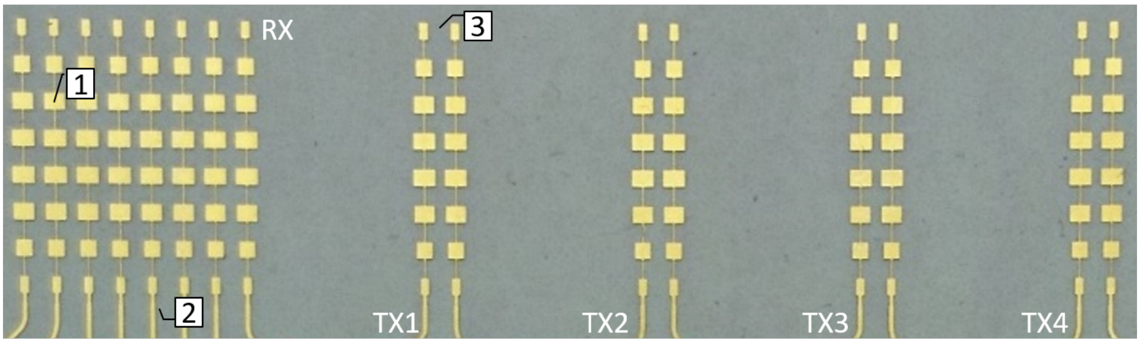

Figure 5.12 – Receive and transmit antennas: (1) is a single patch element, (2) a single receive antenna and (3) a single transmit antenna.

individual receive antennas consist of a single linear array, each transmit antenna is build up with two linear transmit antennas. Receive antennas are spaced with $\frac{\lambda}{2}$ and transmit antennas with $\frac{7\lambda}{2}$ as stated in Section 5.1.1, which is reflected in the sensor simulation. In Figure 5.12, the physiscal elements of the receive and transmit antennas are annotated. While the transmit antennas are switched on sequentially, the receive antennas are activated constantly and accordingly perceive the radar backscatter in parallel. Hence, the directivity of all receive antennas equals the superposition of the directivity of individual receive antennas, while the directivity of the transmit antennas remains independent from each other. Figure 5.13 depicts the directivity characteristics of the transmit and receive arrays. The top line shows the different directivities such as the directivity of individual patch elements, while the bottom line shows the two dimensional azimuth directivity cut for elevation angle zero. A single linear antenna array features a broader beamwidth than two

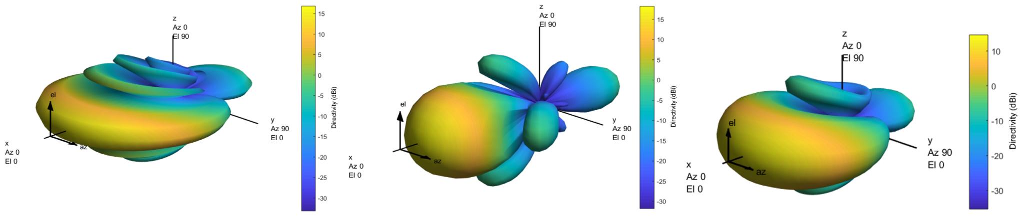

(a) Single RX (b) Full RX (c) Single TX

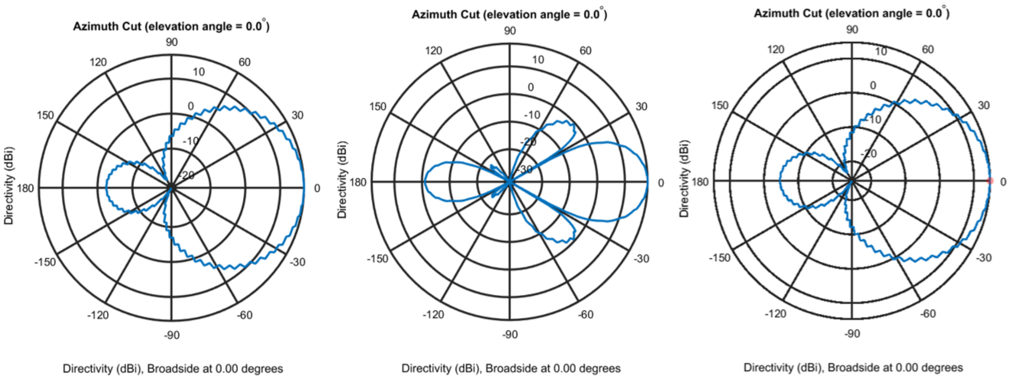

(d) Single RX (e) Full RX (f) Single TX

Figure 5.13 – Directivity of Figure 5.13 a single RX array, Figure 5.13 b superposed RX arrays and Figure 5.13 c a single TX array. Directivity cut of Figure 5.13 a single RX array, Figure 5.13 b superposed RX arrays and Figure 5.13 c a single TX array.

or more superposed linear arrays. Along with a narrower beamwidth, sidelobes occur. The radiator and collector are simulation-specific components that translate the characteristics of the antenna directivity in aperture handles. The radiator specifies the antenna gain in each direction and includes the antenna aperture as well as the resulting directivity of the transmit antenna array. Similar to the radiator, the collector computes the backscatter at the receive antenna arrays, whereas the directivity of the receive antenna array is determined from the previously computed physical array dimensions. Other than the radiator and collector, the transmitter and receiver have physical representatives. For the transmitter stage the signal power as well as the transmitter inherent noise are specified including thermal noise and noise figure. The receiver stage is modeled by its gain that increases the power of the receive signal and by the thermal noise of the receiver. The output signal of the receiver corresponds in the simulation to the time sequence at the real receive antenna, which is not accessible in the real world radar system. After the receiver, mixers are located that generate a beat signal and therefore are part of the simulation within the signal domain. The collocated transmit and receive antennas are part of the antenna platform, that specifies the mounting position of the sensor system. The antenna platform is specified with its initial position in $\{x, y, z\}$ direction and its velocity in $\{x, y, z\}$ direction. As indicated in Figure 5.10, a vehicle can be an

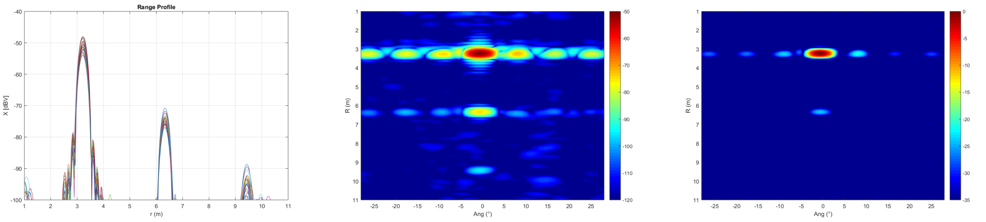

(a) Real range profile (b) Real range-azimuth (c) Real norm range-azimuth

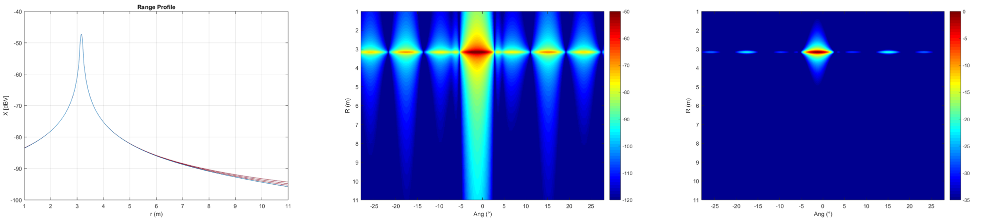

(d) Sim range profile (e) Sim range-azimuth (f) Sim norm range-azimuth

Figure 5.14 – Measurement results for a corner reflector placed at a distance of 3 m: Figure 5.14 a resulting range profile with peak at 3 m and additional peaks obtained by the environment, Figure 5.14 b measured range-azimuth map and Figure 5.14 c normalized measured range-azimuth-map. Simulation results for single point-scattering target at 3 m: Figure 5.14 d simulated range profile with no additional scatterers, Figure 5.14 e according simulated range-azimuth map and Figure 5.14 f normalized simulated range-azimuth map.

antenna platform, for example. Here, the antenna platform corresponds to the ego vehicle. While the velocity is stationary and therefore remains the same during signal acquisition, the antenna platform position is updated after each pulse.

The developed radar sensor modeled was validated by point-wise measurements against real measurements. For that purpose, a common comparable interface of the real and virtual radar sensor is necessary. As the real radar sensor of the Radarbook offers the opportunity to access the beat signal, which is rare in commercial radar systems, this was the interface of choice. Both, the simulated and the real world discretized beat signal $\{s_{b,v}[k], s_{b_r}[k]\}$ are processed with exactly the same algorithms on a host PC. Therefore, differences that occur during the evaluation can be traced back to the environment or the sensor itself that is still an abstraction of the real world sensor. A challenging task is to model the real world environment within the simulation, especially as reflecting points need to included manually. Since objects consist of a huge number of reflecting targets and NLOS propagation brings even visually obscured targets back to the radar, it means a tedious work with little benefit apart from modeling exactly one single scene. While simulated environments can only hold explicitly stated objects with a limited number of attributes, a real environment contains an arbitrary high level of detail. For validation, a clear relation between the observed real-world scenario and its virtual representative is essential. Therefore, it was necessary to consider the limitations of the environment simulation and design

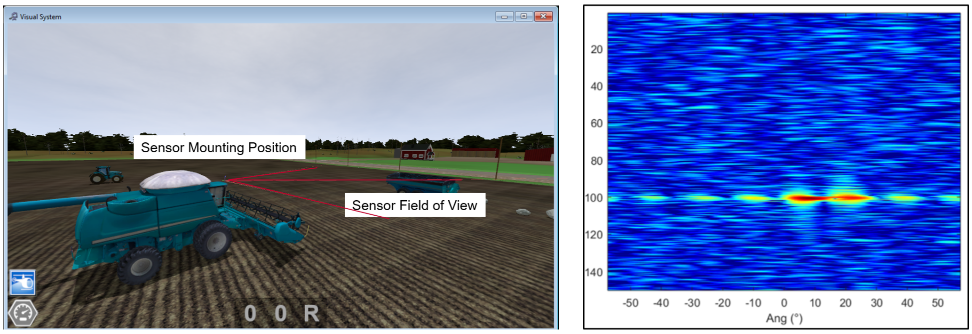

(a) AgSim solution by Creanex (b) Radar simulation

Figure 5.15 – Co-Simulation with agricultural environment simulation. Figure 5.15 a The radar is mounted on the harvester. The trailer is modeled as point target with adequate RCS. Figure 5.15 b shows the resulting radar output that indicates the trailer as a peak.

the radar measurements according to that. The initial goal for testing and validating the radar sensor was to qualify its functionality with regard to peak detection within the range-azimuth dimension. Accordingly, weather and environment conditions with impact on the measurements had to be avoided.

To mimic reflectivity of point targets, that are the most straightforward target in a simulation, cube corners were used to approach the reflecting behavior from a point scatterer as close as possible. The static corner reflectors were positioned at distances ranging between 1 m and 10 m while the radar sensor was rotated within the angles ±45 deg. This simple scenario was adapted in the simulation with point targets positioned accordingly. For validation the localization and level of the maximum peak in the range profile as well as in the range-azimuth map were determined and compared. Corner reflectors were used as validation targets, because they approximate the focused reflexion characteristic of a sphere, while featuring higher target gains with lower dimensions than spheres. That also implies, that the reflected signal power within the radar beam is bundled, thus ensuring that most of the transmitted power is reflected back to the radar.

Figure 5.14 depicts the measurement and simulation results. While the upper line contains the measurement results, the bottom line shows the according simulation results. Although at first sight the results seem to differ, a closer look proves a variation of less than 1 dB at peak level and the correct localization of the target. The remaining differences have their source mainly in the differences between simulation and measurement environment. While the simulation does not contain any other reflecting targets or surfaces in the surrounding environment, the measurements were taken in a parking house. Apart from the backscatter of the corner reflector, clutter from ground, ceiling, sidewalls and columns were obtained. An idea about the characteristic of the environment is given in Figure 5.4, that displays the same measurement surroundings. The outline of the maximum peak itself in Figure 5.14 c reveals how the used corner reflector still differs from a point-scattering target and shows to be extended compared to the outline of the peak in the simulation Figure 5.14 f. It becomes even more obvious while comparing the peak width in the measured Figure 5.14 a and simulated Figure 5.14 d range profile. Artifacts introduced by the windowing functions that are used during FFT processing, are more present in the simulated range-azimuth map due to the lack of other scatterers. After normalizing to 0 dB and clipping the normalized range-azimuth spectrum to −35 dB, the effect is mitigated, see Figures 5.14 c and 5.14 f.

The radar sensor model was applied within the project European Initiative to Enable Validation for Highly Automated Safe and Secure Systems (ENABLE-S3) [22] to an agricultural simulation platform using asynchronous co-simulation. The radar sensor model and system simulation where developed with MATLAB. Using embedded Python, the simulation input from the simulation environment provided a vector including the required information from surrounding objects and the harvesting machine, that acted as the antenna platform, see Figure 5.15. The project demonstrator and the contributions by the author are documented in [78] and [77].

5.2 Noise Radar

After validating the concept of the noise modulated radar system in Section 4.3, the aim is to test the practical functionality in more realistic conditions. The previously developed radar system simulation of Section 5.1.3 serves as an early stage evaluation platform. Spatial sparsity is crucial for CS based signal processing that is applied to retrieve information about reflecting targets. The emulation of the radar sensor and its spatial illumination characteristics may confirm the functionality of the system in real world applications. Therefore, the spatial sparsity assumption is tested under more realistic conditions. The modularity of the radar system simulation allows to replace single blocks while preserving the remaining simulation setup, which enables to perform fair comparisons between variable components. The radar sensor model is the heart of the system emulation and is applied for different radar system architectures. Reflecting targets, propagation channel and weather conditions vary during the simulation but always in the same way for all radar architectures. The environment simulation plays an important part in system evaluation as it allows a direct comparison of the performance of different systems. Otherwise, this is not possible between a real and a virtual system as results from the validation performed in Section 5.1.3.

For emulating the noise radar system, the signal domain of the radar system simulation is replaced by a signal generation providing noise modulated transmit pulses. The signal processing is realized with a reduced correlation receiver using a subset of correlation filters. In parallel, a second radar system is implemented for comparison and benchmarking. This reference LFMCW radar system represents commercial state-of-the-art automotive radar systems. It has been evaluated how the emulated noise radar system performs under different conditions. Furthermore, the noise radar and LFMCW radar system emulations are tested regarding their performance during interference. Robustness against interference is a weak point for FMCW radar systems, motivating the development of alternative systems. The impact of the noise radar system on FMCW performance is also illuminated to give an outlook on potential co-existence of the two different radar systems.

5.2.1 Emulation with radar sensor model

As depicted in Figure 5.16, the radar system simulation requires slight adaptations of the radar system simulation as discussed before and illustrated in Figure 5.10. Besides replacing the transmit waveform, analog and digital signal processing are also affected. Instead of mixing the receive signal with the transmit signal, the first analog processing step consists of correlating the receive signal with a subset of delayed transmit signals, i.e. the correlation filters and at the same time CS measurement functions. The observations are provided to the digital signal processing stage, where the correlation functions also need to be available in order to perform the range reconstruction using OMP.

As indicated in Figure 5.16, CS reconstruction is only performed in range direction, while the velocity direction is performed using classical FFT computation on the reconstructed range profile. The reason is, that there is no additional value in applying CS for the second perception dimension as well, after the signal acquisition issue in terms of sampling rate is already solved. CS signal acquisition reduces the required ADC sampling rate to the PRF as only one single value needs to be sampled per correlation filter instead of the complete beat signal sequence. Afterwards the signal does not need to be sampled anymore, so that after reconstructing the first dimension, which corresponds here to the range direction, it is convenient to use FFT for resolving the second dimension, thus being here the velocity direction. During parameter design it is necessary to choose a pulse width large enough to be affected by the Doppler effect, if the velocity should be reproduced by using the FFT. Otherwise, the velocity needs to be determined differently, e.g. by tracking a peak for several measurement cycles.

5.2.2 Performance testing and impact of weather effects

For performance testing, the range profile as well as the range-azimuth map were evaluated. The number of correlation filters M were selected in order to realize different sub-sampling rates $r = \frac{M}{N}$. Two targets of equal RCS at a distance in range of 52 m and 67 m in front of the radar sensor are assumed. While the antenna platform moves with $100\,\mathrm{km\,h^{-1}}$, the closer target has the velocity $150\,\mathrm{km\,h^{-1}}$ and the more distant target $120\,\mathrm{km\,h^{-1}}$. The results are compared with results from

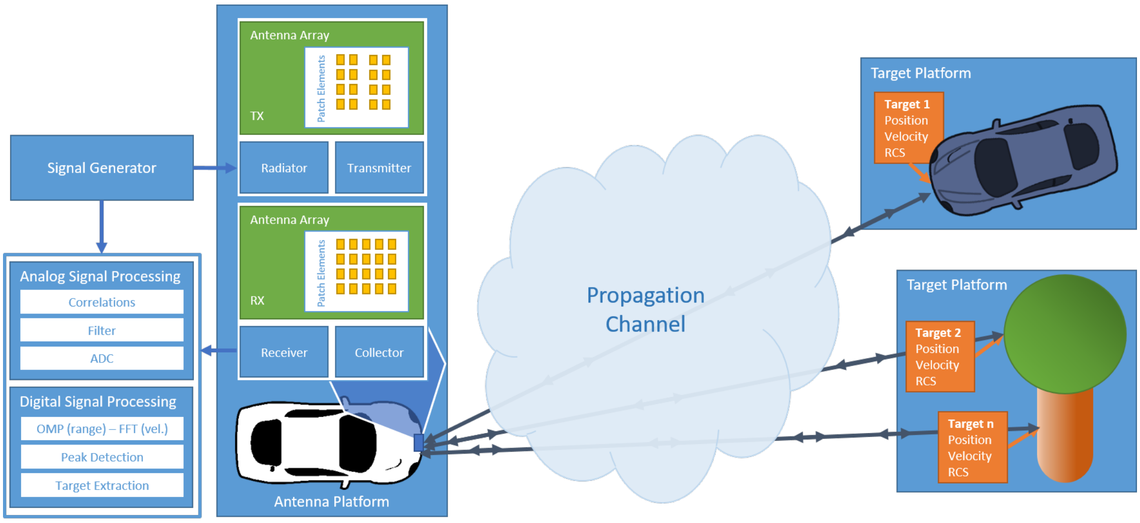

Figure 5.16 – Noise radar system simulation

simulation runs performed by an emulation of the corresponding reference LFMCW radar system. This LFMCW reference simulation differs only in signal model and signal acquisition from the proposed noise radar system, i.e. alle other parameters such as simulated targets and propagation channels are identical for both emulated radar systems. Both radar systems cover the same bandwidth of 1 GHz during $N_P = 2^{10}$ sweeps. The range profile of the LFMCW radar system in Figure 5.17 d shows the limitation in range resolution depending on applied bandwidt in comparison to the noise modulated pulsed radar in Figures 5.17 a to 5.17 c, thus showing the advantage of pulsed radar systems regarding range resolution. For the range profile in Figure 5.17 a, 10 % of the whole set of correlation filters were used. Compared to Figure 5.17 c, where 50 % of correlations were used, the overall noise level is increased significantly, so that the range profile peak of the second more distant target drops below the noise level. Similar to the proof-of-concept simulation in Section 4.3, a sub-sampling rate of 30 % is already sufficient to obtain a sufficient PSNR for detecting both targets in range direction. Although the second more distant peak was lost in the overall noise level of the range profile using only 10 % of the correlation filters, in the corresponding range-Doppler evaluation in Figure 5.17 e it becomes visible again. The signal processing adds gain, which might be enough raising the peak level over the noise level. It is sufficient for raising the peak level over the noise level to perfom the FFT in Doppler direction. This signal processing step makes it possible to determine relative target velocities. But still, using 30 % of correlations provides a much more reliable result as shown in Figure 5.17 f. The reconstruction results for the noise radar emulation correspond to the proof-of-concept simulation regarding the effect of the choice of the sub-sampling rate, i.e. a limitation in reconstruction reliability depending on the sub-sampling rate. Similar to the findings in Section 4.3,

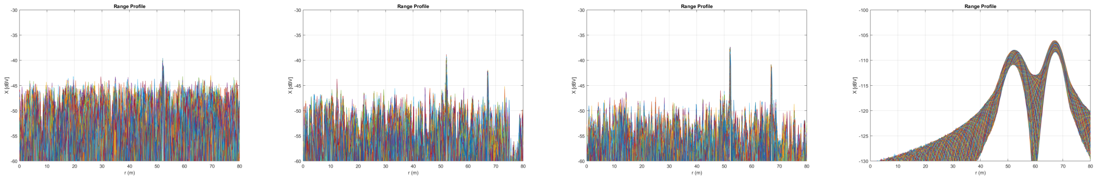

(a) RP $\frac{M}{N} = 0.1$ (b) RP $\frac{M}{N} = 0.3$ (c) RP $\frac{M}{N} = 0.5$ (d) RP LFMCW

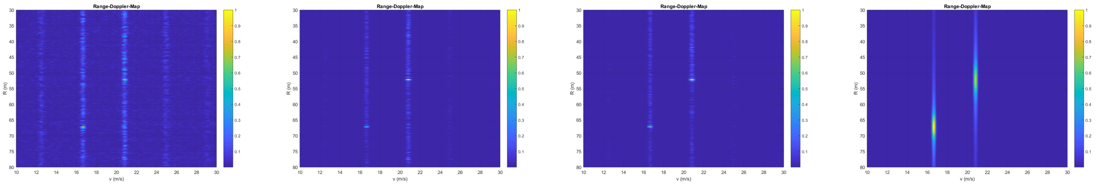

(e) RD $\frac{M}{N} = 0.1$ (f) RD $\frac{M}{N} = 0.3$ (g) RD $\frac{M}{N} = 0.5$ (h) RD LFMCW

Figure 5.17 – Range profile for different sub-sampling rates, i.e. Figure 5.17 a $\frac{M}{N} = 0.1$, Figure 5.17 b $\frac{M}{N} = 0.3$ and Figure 5.17 c $\frac{M}{N} = 0.5$ for the noise radar system and Figure 5.17 d of reference LFMCW system. Accordingly, range-Doppler maps for different sub-sampling rates, i.e. Figure 5.17 e $\frac{M}{N} = 0.1$, Figure 5.17 f $\frac{M}{N} = 0.3$ and Figure 5.17 g $\frac{M}{N} = 0.5$ for the noise radar system and Figure 5.17 h of reference LFMCW system.

a sub-sampling factor of 30 % proves to be sufficient to obtain a reliable and robust range reconstruction.

Taking the insights from the weather measurements in Section 5.1.2 into account, additional attenuation was applied to the receiver. The levels of attenuation represent radome impacting effects, that result from adverse weather conditions. Since additional radome attenuation affects the complete backscatter, channel noise is lowered in the same way as the target reflection. Accordingly, the signal level and the noise level are lowered corresponding to the applied radome attenuation. The range profile in Figure 5.18 a results from 10 dB attenuation and the range profile in Figure 5.18 b from 20 dB attenuation. However, the limitation lies in receiver noise and sensitivity. Therefore, while an additional radome attenuation of 50 dB as depicted in Figure 5.18 c still allows to detect the target peaks, an attenuation of 60 dB cannot be compensated anymore. The limit of tolerable radome attenuation needs to be determined for each receiver system individually and cannot be generalized.

Due to the mostly temporal characteristic of the phenomena resulting from adverse weather effects, using narrow pulses reduces the probability of coinciding temporal radome attenuation and receiving a reflected pulse. With longer lasting chirps such as in LFMCW radar systems a distortion due to e.g. splash water is more likely. If also the velocity dimension shall be resolved, instead of a single chirp a train of chirps is transmitted, which increases the chances of making the assumption regarding stionary weather conditions obsolete. However, in both systems target or object tracking mitigates the impact of adverse conditions. Supporting methods to handle temporal adverse conditions therefore consists in a mechanical design that helps to

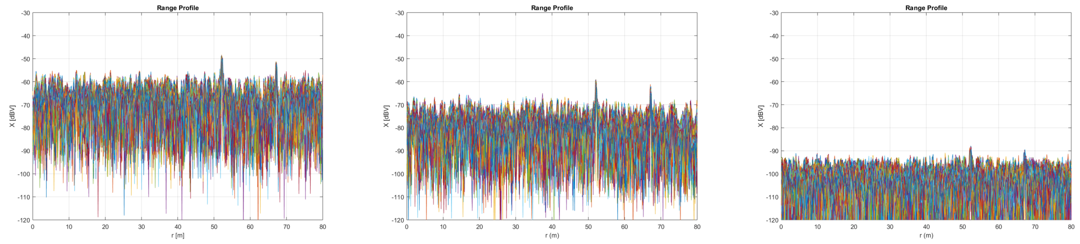

(a) 10 dB

(b) 20 dB

(c) 50 dB

Figure 5.18 – Range profile for different sub-sampling rates, i.e. Figure 5.18 a $\frac{M}{N} = 0.1$, Figure 5.18 a $\frac{M}{N} = 0.3$ and Figure 5.18 a

absorb water and prevent snow or ice layers, which is often taken into account by implementing a heating of the radome. In addition, the electrical parameters of the receiver stage need to be designed with sufficient safety margins to be capable of being sufficiently sensitive for the desired low backscatter power level, especially for LFMCW radar systems. Radar receivers using CCF, benefit from the signal processing gain.

5.2.3 Interference in automotive radar

Interference is another factor that motivates to find new approaches for radar signal acquisition and processing, that are feasible for future scenarios of automated cars, where the number of radar systems on the streets is expected to be even much higher than today. Interference from other transmitting systems operating on the same frequency bands sum up additional backscatter and therefore disturb each other. Hence, any receive signal $s_R(t)$ changes such as stated in a general way in (5.12) to the resulting receive signal $s_{R,I}(t)$, that is the result of the sum of the interference $s_I(t)$. Additional noise and attenuation from adverse weather conditions are neglected in favor of clarity within this section.

$$s_{R,I}(t) = s_R(t) + s_I(t) \tag{5.12}$$

Since interference mainly affects the spectral components, it can be understood and analyzed best in this domain. An additional issue of interference is given by the fact, that interference is received after one-way propagation instead of two-way propagation such as the desired radar backscatter. This can result in driving the receiver to saturation on transistor level, which comes along with additional spectral components as a result of clipping. In the spectral domain, the receiver side compares the transmit signal with the receive signal, see Section 3.3. Although radar systems as any other receiving systems can be interfered by any arbitrary systems that operate in the same frequency band, the focus remains here on interference by either a radar system of the same type or the opposite type as this can be assumed to be the most

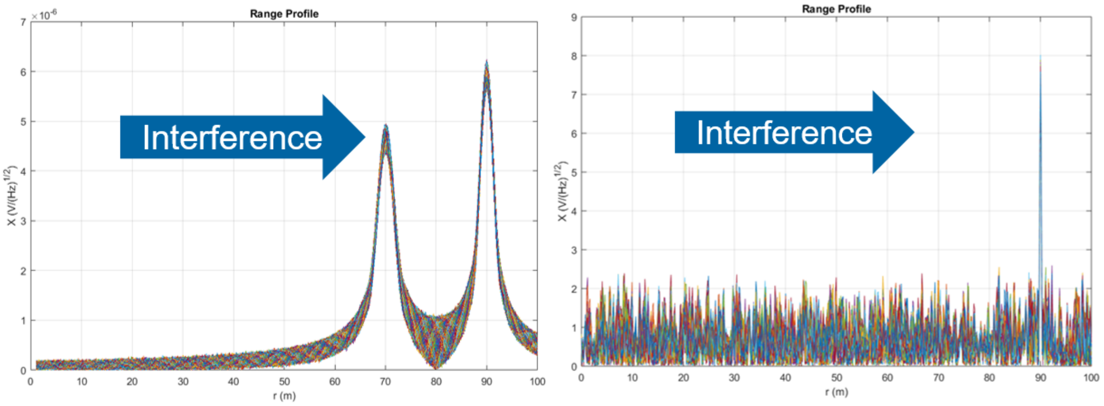

(a) RP of LFMCW

(b) RP of noise radar

Figure 5.19 – Range profiles after interference from second radar system of same architecture for Figure 5.19 a LFMCW radar receive and Figure 5.19 b noise modulated correlation receiver.

common scenario. Especially the case, where a pulsed radar system interferes with an LFMCW radar system requires consideration as it is predictable that current commercial radar systems will continue to play an important role within at least the next decades. To find acceptance for new types of radar, an analysis of the impact on common radar systems is required to ensure potential challenges as well as new possibilities regarding the co-existence of both systems are considered thoroughly.

Therefore, the same radar sensor emulation was applied to create the reference LFMCW as well as the suggested noise radar system. It is assumed that both radar systems are object of interference from another radar system of equal architecture. Figure 5.19 show resulting range profiles. Frequency shifts and delays of the regular radar backscatter cannot be distinguished from interference in an LFMCW radar system without additional information. Therefore, the interference appears as an additional peak in the range profile according to Figure 5.19 a. In contrast, the noise modulation of the pulse-based radar system, offers by design a high robustness towards interference. Besides the inherent robustness against interference of pulsed radar systems, the noise modulation acts as a unique fingerprint to each pulse, which leads to a stable interference suppression as long as the interfering radar system does not produce the same pseudo-random noise. Hence, the interference suppression works only for truly uncorrelated random or pseudo-random processes for all involved radar systems. With these assumptions, the resulting range profile in Figure 5.19 b shows only the peak from a target that was illuminated by the radar system and no peaks resulting from the interfering radar system.

To determine the impact of a noise pulse radar system on an LFMCW radar system, the computation of the beat frequency $f_b(t)$ is analyzed, which was elaborated in Section 2.1.2. The beat frequency is the frequency difference of the transmitted and received frequency ramp in an LFMCW radar system. However, in case of the existence of an interference source within the range of the receiving radar system, interfering frequency components denoted as $f_I(t)$ are added to the receive signal, see (5.13).

$$f_{b,I}(t) = f_T(t) - (f_R(t) + f_I(t)) = f_b(t) - f_I(t) \tag{5.13}$$

Assuming P pulses and L reflecting targets, the received frequency aggregation from the LFMCW radar system $f_{R,LFMCW}(t)$ corresponds to (5.14), where the transmitted frequency ramp is shifted by the round-trip time $\tau_{r,l}$ and the Doppler shift $f_{D,l}$. The window function $h(t)$ limits the signal to the chirp duration T_c.

$$f_{R,LFMCW}(t) = \sum_{p,l=0}^{P,L-1} \left[\alpha(t - 2\tau_{r,l} - pt_p) + f_{D,l}\right] h\left(t - T_c - 2\tau_{r,l} - pt_p\right) \ . \tag{5.14}$$

In an LFMCW radar system of bandwidth B with chirp rate $\alpha = \frac{B}{T_c}$, the frequency shift corresponding to the propagation time is computed by

$$f_{r,l,LFMCW} = \alpha\tau_{r,l} = \alpha \cdot \frac{2r_l}{c} \tag{5.15}$$

and the Doppler shift with

$$f_{D,l,LFMCW} = \alpha\tau_{D,l} = \alpha \cdot \frac{-2v_{r,l} \cdot p\tau_p}{c} \ . \tag{5.16}$$

For the noise radar system, the frequency definition of the receive signal $f_{R,NW}(t)$ is given according to (5.17) such as stated by the author in [85]. Assuming N spectral components f_n weighted with randomly generated factors w_n, the received frequency is the sum of L reflected targets and P reflected pulses. Compared to the LFMCW radar system, the window function is smaller, because the pulse length t_s is less than the chirp length T_c.

$$f_{R,NW}(t) = \sum_{p,l=0}^{P,L-1} \sum_{n=0}^{N-1} \left[w_n f_n + f_{D,l,pulse}\right] h\left(t - t_s - \tau_{r,l} - pt_p\right) \tag{5.17}$$

In contrast to the LFMCW system, the Doppler shift does not depend to the chirp rate α and also adheres only to one-way propagation instead of two-way propagation:

$$f_{D,l,Pulse} = \frac{-v_{r,l}}{c_0 \cdot pt_p} \ . \tag{5.18}$$

Considering (5.13), the resulting Doppler shift is the difference of the two-way propagation LFMCW Doppler and one-way propagation noise pulse Doppler shift. For the sake of simplification it is assumed, that a reflecting target l is a transmitting

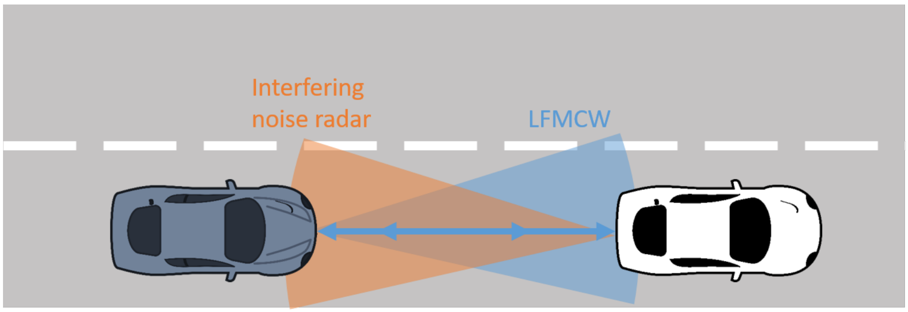

Figure 5.20 – Scenario of LFMCW radar system interfered by noise radar system

radar platform at the same time as depicted in Figure 5.20. Accordingly, the Doppler shift results into (5.19), where $f_{D,I}$ denotes the Doppler frequency shifted by interference Doppler.

$$f_{D,I} = f_{D,l,LFMCW} - f_{D,l,Pulse} = \frac{-v_{r,l}\left(2\alpha p^2 t_p^2 + 1\right)}{c_0 p t_p} \ . \tag{5.19}$$

The beat frequency of the LFMCW radar system is impacted by the pulsed noise radar system only during the pulse duration as stated with the window function in (5.20). After the parameters of the environment and target were assumed to be stationary during individual chirps, the pulsed interference therefore changes the beat into a time dependent variable.

$$f_{b,I}(t) = \sum_{p,l=0}^{P,L-1} \left(\alpha \tau_{r,l} - f_{D,I} - \sum_{n=0}^{N-1} w_n f_n \right) h\left(t - t_s - \tau_{r,l} - p t_p\right) \ . \tag{5.20}$$

Apparently, the suggested noise radar system is a distortion to LFMCW radar systems, which was to be expected. However, the duration of the interference distortion is short compared to another LFMCW radar system. This has been elaborated by the author in [87]. In a cognitive design it is possible to implement a timing for the pulsed radar system that transmits only during the down-chirps that are not acquired by the LFMCW radar system or during system inherent transmission breaks, e.g. for chirp configuration or signal processing, just as presented by the author in [90] and [61]. Compared to non-modulated pulsed radar systems, the noise modulation allows to apply lower power levels, which in addition prevents the interfered radar system to leave the linear operation point and go into saturation. Hence, a co-existence between the noise radar system and LFMCW radar systems is possible. Apart from that, noise modulation and the pulse architecture enable a radar perception that proves to be robust towards noise. Therefore, the suggested noise radar states a promising design that meets the challenges and requirements for future radar systems for automated driving.

6 Conclusion and Outlook

Autonomous driving is expected to reduce fatal accidents significantly, but also to lead to more efficient mobility concepts after removing human drivers from the steering wheel. However, automated driving has to be highly reliable to be trusted and accepted. So far, there are still many safety and security concerns that are rising whenever an automated vehicle is involved in an accident. Although human drivers are probably more failure prone, the expected higher safety standard for autonomous vehicles needs to be fulfilled in order to reach broad acceptance. Satisfying higher levels of safety requires the improvement and development of current sensor systems used for ADAS.

Radar sensors are a key component for realizing autonomous driving because their performance remains robust in adverse or difficult environmental conditions. Beyond fulfilling complementary sensor functions, additional information such as distance or velocity are obtained by the radar, too. For automotive radar systems there are two main aspects that are subject of research and development. These are on the one hand increasing efficiency and robustness for radar sensor signal acquisition and processing, and on the other hand accelerating validation and verification of systems with more and more increased complexity. While the first aspect requires the development of new signal acquisition and processing methods, the second aspect requires a paradigm change regarding test systems.

In this thesis, the question was addressed how to improve the architecture and how to reduce the effort in signal acquisition for advanced radar applications needed for highly automated and autonomous driving. A noise modulated pulsed radar waveform was suggested to improve robustness against interference. The signal acquisition effort was significantly reduced by applying CS methods for signal acquisition and reconstruction. A demonstrator based on a phenomenological sensor simulation was used to compare the performance of the suggested Compressive Sensing noise radar system with a typical LFMCW radar system. The phenomenological radar sensor simulation was developed according to a real radar system. Furthermore, the sensor simulation was validated against that radar system. The results showed, that the suggested noise radar system with its CS based correlation receiver is capable to perform in a very consistent and reliable way, while reducing the signal acquisition significantly compared to standard correlation receivers. It was able to outperform the baseline LFMCW radar system during low SNR and interference scenarios.

First, an insight was given to automotive radar systems and CS. Underlying principles and theory were introduced, while highlighting some particular aspects such as environmental conditions, different radar architectures and interference. In the state-of-the-art section an overview was given on CS approaches and implementations as well as automotive and noise related aspects. The main part presented and evaluated different ways of using CS for automotive radar systems in order to either improve or extend their functionality. The concept of a noise radar system using CS for automotive applications was analyzed in detail and tested in a proof-of-concept simulation. The successful simulation prototype was transferred to an emulation of a noise radar system with CS signal acquisition and processing. The sensor model applied in the emulation was developed according to a physical radar system. Besides testing the functionality of the suggested radar system, the robust performance during adverse weather conditions, which were derived from measurements, was evaluated as well as the robustness towards interference from another radar system.

With increasing computational power that is available in passenger cars, which enables automated driving, new possibilities arise for signal processing methods that are computationally intensive. Therefore, it was the intention of this work to contribute to the exploration of such method that support automated driving and sensing in particular by illuminating how CS can be used for automotive radar systems. It was the aim to present methods for future radar systems that apply CS in order to shift the analog signal acquisition effort into the digital domain where signal processing benefits from increased computational capabilities. Using a CS based method, it was the aim to show how the signal acquisition effort can be reduced, while even increasing the system robustness. With an virtual implementation of the suggested radar system, the feasibility of the approach was demonstrated. That included the goal of developing a radar sensor model and validate it against point-wise real world measurements. To be able of deriving strong and reliable statements about the radar system performance, it was aimed at introducing realistic adverse impacts such as adverse weather conditions compromising the radome. Finally, future testing purposes were intended to be realized by connecting the radar system simulation to an environment simulation. Hence, this thesis comprises a sum of individual goals serving different aspects but having the common purpose of paving the way for safe automated driving in the future by using innovative strategies for radar systems.

The analysis of possible CS applications to automotive radar systems revealed a variety of methods that allow to either to reduce the signal acquisition effort or augment radar functionality. For pulsed radar systems, CS can be applied to reduce the sampling rate significantly. However, the example of a SAR implementation or a phased array system demonstrate that CS can be also used to increase spatial resolution. Although especially RMPI comes along with a reduction of sampling effort by 80 % to 90 %, a reduced correlation receiver turned out to be a preferable implementation. Compared to usual correlation receivers the dimension of the correlation filter bank can be reduced by 70 % and the sampling frequency is reduced to the PRI. With only 30 % of correlations, i.e. measurements, range information about reflecting targets can be reconstructed even for an SNR below zero, which outperforms significantly SNR levels of 10 dB to 20 dB in automotive propagation channels. The robust performance and the reduced measurement and signal acquisition effort were confirmed in a radar system emulation that mimics spatial characteristics of a real radar sensor. This confirms the plausibility of the suggested radar system, since spatial sparsity is the key characteristic in the CS signal acquisition and reconstruction method.

The developed radar sensor model was validated against real radar measurements using the physical LFMCW radar system. The validation was performed using point-wise measurements with a corner reflector. In addition, the physical radar system was used to develop models that reflect the radar behavior in adverse weather conditions. The main factor, which impacts the radar performance, turned out to be water covering the radome. Therefore, the focus was to determine different static and dynamic realistic automotive scenarios. It was concluded from measurements that splash water not only attenuates the radar backscatter by approximately 20 dB, but that it also results in blurs due to the lens effect of water. Water sprinkles cause with up to 10 dB less attenuation due to the incomplete partial coverage by water of the radome. Depending on the surface structure the radome and therefore the radar perception recovers soon after the application of water sprinkles or a splash water incident, so that the impact can be mitigated by target tracking. The emulated noise-radar system proved to tolerate additional radome attenuation up to 60 dB. The limitation comes from electrical parameters of the receiver stage, i.e. sensitivity and noise figure.

Besides robustness, interference plays an important part in evaluating the performance of a radar system. It was demonstrated, that the noise radar system operates in an interference-proof way. Compared to an LFMCW radar system, where interference causes additional spikes, the noise radar system detects only peaks that result from reflecting targets. An interfering signal from another radar system is not reconstructed by the CS processing algorithm but only backscatter that originates from the own sensor system. On the one hand, pulsed radar systems are already proof towards interference, because of the correlation receiver. But only the noise modulation makes sure, that only pulses that were transmitted by a specific radar are reconstructed, while not spreading the pulse in time domain such as other modulation approaches. Furthermore, the co-existence of LFMCW radar systems with the suggested noise radar systems was analyzed. The acceptance of new radar concepts depends on a seamless introduction to market while current commercial radar systems are not impacted in their performance. Compared to a non-modulated pulsed radar system, the noise waveform with its low transmit power prevents LFMCW receiver most likely from clipping.

With the broad scope of automotive radar related aspects, that ranges from CS acquisition methods over radar architectures to virtual validation and verification methods the work provides many connecting factors for future research. In order to meet alternating requirements on the CS based receiver stage, adaptive signal acquisition methods can be analyzed in order to preserve the perception robustness during a changed spatial sparsity, for example. In addition, implementing a cognitive pulse transmission concept will improve the suggested radar system regarding its ready-to-market level. Although any pulsed radar system acts as a jammer to LFMCW radar systems, it was demonstrated in other projects by the author how the impact can be mitigated by a cognitive design that makes use of transmission pauses. Before implementing the noise radar system in silicone, tests with a realistic environment simulation will be beneficial to avoid overlooking pitfalls. Using a realistic environment simulation will allow to extend the suggested noise radar system to an imaging SAR, which will add significant value to the radar system for automated driving. These are only few examples for connecting points, but it shows that the field of CS in automotive radar systems remains an exiting research field.

Abbreviations

A2I	analog-to-information
ABF	adaptive beamforming
ACC	adaptive cruise control
ACF	autocorrelation function
ACPS	automated cyber-physical systems
ADAS	advanced driver assistance systems
AD	analog-to-digital
ADC	analog-to-digital-converter
AIC	analog-to-information converter
AF	array factor
AoA	angle-of-arrival
AWGN	additional white Gaussian noise
BP	basis pursuit
BPDN	basis pursuit denoising
BSD	blind spot detection
CCF	cross-correlation function
CFAR	constant false alarm rate
CIC	cascaded-integrator-comb-filter
CS	Compressive Sensing
CW	continuous-wave

DBF	digital beamforming
DCR	direct conversion receiver
DCT	discrete cosine transformation
DoA	direction of arrival
DSP	digital signal processor
DTC	digital-to-time converter
EAES	Entwurf und Architektur Eingebetteter Systeme
EBF	eletronic beam forming
EBS	electronic beam steering
EMR	electromagnetic radiation
ENABLE-S3	European Initiative to Enable Validation for Highly Automated Safe and Secure Systems
ESA	electronical steerable arrays
ESD	electro-static discharge
FAR	false alarm rate
FFT	fast fourier transformation
FHT	Fast Hadamard Transform
FM	frequency modulated
FMCW	frequency modulated continuous wave
FoV	field-of-view
FPGA	field programmable gate array
GPU	graphic processing unit
IEEE	Institute of Electrical and Electronics Engineers
IF	intermediate frequency
IFFT	inverse FFT
IC	integrated circuit

IP	interior-point
ISI	inter-symbol interference
ISM	industrial-scientific-medical
ITS	Intelligent Transport Systems
ITU	International Telecommunication Union
LabRadOr	laboratory radar system
LFMCW	Linear FMCW
LFSR	linear feedback shift registers
LO	local oscillator
LOS	line-of-sight
LPDC	low-density parity check
LPF	low-pass filter
LRR	long range radar
LS	least squares
LVDS	low-voltage differential signal
MF	matched filter
MIMO	multiple-input multiple-output
MLS	maximum length sequences
MLFSR	maximum length feedback shift register
MRI	magnetic resonance imaging
MRR	mid range radar
MWC	modulated wave converter
NATO	North Atlantic Treaty Organization
NLOS	non-line-of-sight
OFDM	orthogonal frequency division multiplexing

OMP	orthogonal matching pursuit
PBR	pseudo-binary random
PCB	printed circuit board
PCR	pulse compression rate
pp	percentage points
PRF	pulse repetition frequency
PRN	pseudo-random noise
PRI	pulse repetition interval
PSF	point-spread function
PSNR	peak signal-to-noise ratio
RCS	radar cross section
RF	radio frequency
RIP	random isometry property
RMPI	random modulated pre-integration
RNR	random noise radar
SAR	synthetic aperture radar
SDR	software-defined radio
SOTA	State-of-the-Art
SIR	signal-to-information
SNR	signal-to-noise-ratio
SPR	sidelobe-to-peak-ratio
SRR	short range radar
SuT	system under test
TCP/IP	Transmission Control Protocol/Internet Protocol
ToF	time-of-flight

TWD	through-wall-detection
UWB	ultra-wide band
V2V	vehicle to vehicle
V2I	vehicle to infrastructure
V2x	vehicle-to-x

References

[1] *Allgemeinzuteilung von Frequenzen für Funkanwendungen für intelligenteVerkehrssysteme („Intelligent Transport Systems“, ITS)*, Vfg. Nr. 69/2009, Bundesnetzagentur, Germany, 2009. [Online]. Available: `https://www.bundesnetzagentur.de/DE/Sachgebiete/Telekommunikation/Unternehmen_Institutionen/Frequenzen/Allgemeinzuteilungen/allgemeinzuteilungen-node.html`.

[2] *Allgemeinzuteilung von Frequenzen für Kraftfahrzeug-Kurzstreckenradare im Frequenzbereich 21,65- 26,65 GHz*, Vfg. Nr. 41/2012, Bundesnetzagentur, Germany, 2012. [Online]. Available: `https://www.bundesnetzagentur.de/DE/Sachgebiete/Telekommunikation/Unternehmen_Institutionen/Frequenzen/Allgemeinzuteilungen/allgemeinzuteilungen-node.html`.

[3] *Allgemeinzuteilung von Frequenzen für Kraftfahrzeug-Kurzstreckenradare im Frequenzbereich 77 - 81 GHz*, Vfg. Nr. 66/2014, Bundesnetzagentur, Germany, 2014. [Online]. Available: `https://www.bundesnetzagentur.de/DE/Sachgebiete/Telekommunikation/Unternehmen_Institutionen/Frequenzen/Allgemeinzuteilungen/allgemeinzuteilungen-node.html`.

[4] *Allgemeinzuteilung von Frequenzen für Verkehrstelematiksysteme*, Vfg. Nr. 125/2017, Bundesnetzagentur, Germany, 2017. [Online]. Available: `https://www.bundesnetzagentur.de/DE/Sachgebiete/Telekommunikation/Unternehmen_Institutionen/Frequenzen/Allgemeinzuteilungen/allgemeinzuteilungen-node.html`.

[5] L. Anitori, M. Otten, A. Maleki, and R. Baraniuk, “Compressive CFAR radar detection,” in *In Proc. IEEE Radar Conference (RADAR*, 2012, pp. 0320–0325.

[6] W. U. Bajwa, *Geometry of random Toeplitz-block sensing matrices: bounds and implications for sparse signal processing*, 2012. DOI: `10.1117/12.919475`.

[7] T. Björklund and E. Magli, “A Parallel Compressive Imaging Architecture for One-Shot Acquisition,” in *Proc. of 2013 Picture Coding Symposium*, IEEE - INST ELECTRICAL ELECTRONICS ENGINEERS INC, 2013, pp. 65–68. DOI: `10.1109/PCS.2013.6737684`. [Online]. Available: `http://porto.polito.it/2523696`.

[8] G. Brooker, *Sensors for ranging and imaging*, English. Raleigh, NC: SciTech Pub, 2009;2013; ISBN: 9781891121746;189112174X;.

[9] A. Caddemi and E. Cardillo, “A study on dynamic threshold for the crosstalk reduction in frequency-modulated radars,” in *2017 Computing and Electromagnetics International Workshop (CEM)*, Jun. 2017, pp. 29–30.

[10] E. J. Candès and J. Romberg, “Sparsity and Incoherence in Compressive Sampling,” *Inverse Problems*, vol. 23, no. 3, 2007.

[11] E. J. Candès and M. B. Wakin, “An Introduction To Compressive Sampling. A sensing/sampling paradigm that goes against the common knowledge in data aquisition,” *IEEE Signal Processing Magazine*, vol. 25, no. 21, 2008.

[12] E. Candès, J. Romberg, and T. Tao, “Robust uncertainity principles: Exact signal reconstruction from highly incomplete frequency information,” *IEEE Transactions on Information Theory*, vol. 52, no. 2, 2006.

[13] E. Candès, J. Romberg, and T. Tao, *Stable Signal Recovery from Incomplete and Inaccurate Measurements*, 2005.

[14] S. Chang, T.-S. Chu, J. Roderick, C. Du, T. Mercer, J. Burdick, and H. Hashemi, “UWB human detection radar system: A RF CMOS chip and algorithm integrated sensor,” in *Ultra-Wideband (ICUWB), 2011 IEEE International Conference on*, Sep. 2011, pp. 355–359. DOI: `10.1109/ICUWB.2011.6058863`.

[15] J. Chuang, M. W. DeMay, and R. M. Narayanan, “Design, Analysis, and Performance of a Noise Modulated Covert Communications System,” *EURASIP Journal on Wireless Communications and Networking*, vol. 2008, no. 1, p. 979 813, Aug. 2008, ISSN: 1687-1499. DOI: `10.1155/2008/979813`. [Online]. Available: `https://doi.org/10.1155/2008/979813`.

[16] M. A. Davenport, M. F. Duarte, Y. C. Eldar, and G. Kutyniok, “Introduction to compressed sensing,” in *Compressed Sensing. Theory and Application*, Y. C. Eldar and G. Kutyniok, Eds., New York: Cambridge University Press, 2012, pp. 1–64.

[17] M. Dawood and R. Narayanan, “Ambiguity function of an ultrawideband random noise radar,” *IEEE Antennas and Propagation Society International Symposium. Transmitting Waves of Progress to the Next Millennium. 2000 Digest. Held in conjunction with: USNC/URSI National Radio Science Meeting (C*, vol. 4, 2142–2145 vol.4, 2000.

[18] D. L. Donoho and X. Huo, “Uncertainty Principles and Ideal Atomic Decomposition,” *IEEE Transactions on Information Theory*, vol. 47, no. 7, 2001.

[19] C. Du and H. Hashemi, “An UWB CMOS impulse radar,” in *Radio Frequency Integrated Circuits Symposium (RFIC), 2013 IEEE*, Jun. 2013, pp. 423–426. DOI: `10.1109/RFIC.2013.6569621`.

[20] M. Duarte, M. Davenport, D. Takhar, J. Laska, T. Sun, K. Kelly, and R. Baraniuk, “Single-Pixel Imaging via Compressive Sampling,” *Signal Processing Magazine, IEEE*, vol. 25, no. 2, pp. 83–91, Mar. 2008, ISSN: 1053-5888. DOI: `10.1109/MSP.2007.914730`.

[21] M. F. Duarte and Y. C. Eldar, “Structured Compressed Sensing: From Theory to Applications,” *IEEE Transactions on Signal Processing*, vol. 59, no. 9, 2011.

[22] ENABLE-S3. (Sep. 2018). European Initiative to Enable Validation for Highly Automated Safe and Secure Systems. accessed on 2018-09-14, [Online]. Available: `https://www.enable-s3.eu`.

[23] J. Ender, “A brief review of compressive sensing applied to radar,” in *Radar Symposium (IRS), 2013 14th International*, vol. 1, Jun. 2013, pp. 3–16.

[24] S. Foucart, *A Mathematical Introduction to Compressive Sensing*, H. Rauhut, Ed., New York, NY, 2013. DOI: `10.1007/978-0-8176-4948-7`.

[25] N. Friedman, *The Naval Institute Guide to World Naval Weapon Systems*, ser. NAVAL INSTITUTE GUIDE TO WORLD NAVAL WEAPONS SYSTEMS. Naval Institute Press, 2006, ISBN: 9781557502629. [Online]. Available: `https://books.google.de/books?id=4S3h8j%5C_NEmkC`.

[26] G. Fung and O. L. Mangasarian, “Equivalence of Minimal ℓ_0- and ℓ_p-Norm Solutions of Linear Equalities, Inequalities and Linear Programs for Sufficiently Small p.,” *J. Optimization Theory and Applications*, vol. 151, no. 1, pp. 1–10, 2011. DOI: `10.1007/s10957-011-9871-x`. [Online]. Available: `http://dblp.uni-trier.de/db/journals/jota/jota151.html%5C#FungM11`.

[27] D. Genschow and J. Kloas, “Evaluation of a UWB radar interface for low power radar sensors,” in *Radar Conference (EuRAD), 2015 European*, Sep. 2015, pp. 321–324. DOI: `10.1109/EuRAD.2015.7346302`.

[28] P. R. Gill, A. Wang, and A. Molnar, “The In-Crowd Algorithm for Fast Basis Pursuit Denoising,” *IEEE Transactions on Signal Processing*, vol. 59, no. 10, pp. 4595–4605, Oct. 2011, ISSN: 1053-587X. DOI: `10.1109/TSP.2011.2161292`.

[29] N. A. Goodman and L. C. Potter, “Pitfalls and possibilities of radar compressive sensing,” *Appl. Opt.*, vol. 54, no. 8, pp. C1–C13, Mar. 2015. DOI: `10.1364/AO.54.0000C1`. [Online]. Available: `http://ao.osa.org/abstract.cfm?URI=ao-54-8-C1`.

[30] M. Goppelt, H. Bloecher, and W. Menzel, "Automotive radar–investigation of mutual interference mechanisms," *Advances in Radio Science*, vol. 8, pp. 55–60, Sep. 2010.

[31] J. Haupt, W. U. Bajwa, M. Rabbat, and R. Nowak, "Compressed Sensing for Networked Data," *IEEE Signal Processing Magazine*, vol. 25, no. 2, pp. 92–101, Mar. 2008, ISSN: 1053-5888. DOI: `10.1109/MSP.2007.914732`.

[32] M. F. Holder, V. P. Makkapati, P. Rosenberger, T. D'hondt, Z. Slavik, F. M. Maier, H. Schreiber, Z. Magosi, H. Winner, O. Bringmann, and W. Rosenstiel, "Measurements Revealing Challenges in Radar Sensor Modeling for Virtual Validation of Autonomous Driving," *21st IEEE International Conference on Intelligent Transportation Systems*, 2018.

[33] M. Holder, Z. Slavik, and T. D'hondt, "Radar Signal Processing Chain for Sensor Model Development," in *Validation and Verification of Automated Systems: Results of the ENABLE-S3 Project*, A. Leitner, D. Watzenig, and J. Ibanez-Guzman, Eds. Cham: Springer International Publishing, 2020, pp. 119–133, ISBN: 978-3-030-14628-3. DOI: `10.1007/978-3-030-14628-3_11`. [Online]. Available: `https://doi.org/10.1007/978-3-030-14628-3_11`.

[34] D. Hospach, S. Mueller, J. Gerlach, O. Bringmann, and W. Rosenstiel, "Simulation and evaluation of the influence of sensor characteristics on vision based Advanced Driver Assistance Systems," in *IEEE International Conference on Intelligent Transportation Systems*, Oct. 2014.

[35] *IEEE 521-2002*, IEEE, Aug. 2003. [Online]. Available: `http://standards.ieee.org/findstds/standard/521-2002.html`.

[36] Y.-T. Im, J.-H. Lee, and S.-O. Park, "A pulse-Doppler and FMCW radar signal processor for surveillance," in *Synthetic Aperture Radar (APSAR), 2011 3rd International Asia-Pacific Conference on*, Sep. 2011, pp. 1–4.

[37] S.-H. Jeong, H.-Y. Yu, J.-E. Lee, J.-N. Oh, and K.-H. Lee, "A multi-beam and multi-range radar with FMCW and digital beam forming for automotive applications," *Progress In Electromagnetics Research*, vol. 124, pp. 285–299, 2012. DOI: `10.2528/PIER11110805`. [Online]. Available: `http://www.jpier.org/pier/pier.php?paper=11110805`.

[38] H. Jiang, B. Zhang, Y. Lin, W. Hong, Y. Wu, and J. Zhan, "Random noise SAR based on compressed sensing," in *2010 IEEE International Geoscience and Remote Sensing Symposium*, Jul. 2010, pp. 4624–4627. DOI: `10.1109/IGARSS.2010.5651241`.

[39] S. Kalisvaart, Z. Slavik, and O. Op den Camp, "Using Scenarios in Safety Validation of Automated Systems," in *Validation and Verification of Automated Systems: Results of the ENABLE-S3 Project*, A. Leitner,

D. Watzenig, and J. Ibanez-Guzman, Eds. Cham: Springer International Publishing, 2020, pp. 27–44, ISBN: 978-3-030-14628-3. DOI: `10.1007/978-3-030-14628-3_5`. [Online]. Available: `https://doi.org/10.1007/978-3-030-14628-3_5`.

[40] K. D. Kammeyer, *Nachrichtenübertragung*, 2nd ed., N. Fliege, Ed. Stuttgart: B.G. Teubner Stuttgart, 1996, ISBN: 3-519-16142-7.

[41] Y.-H. Kao and T.-S. Chu, "A Direct-Sampling Pulsed Time-of-Flight Radar With Frequency-Defined Vernier Digital-to-Time Converter in 65 nm CMOS," *IEEE Journal of Solid-State Circuits*, vol. 50, no. 11, pp. 2665–2677, Nov. 2015, ISSN: 0018-9200. DOI: `10.1109/JSSC.2015.2472599`.

[42] S. Kim, D. Oh, and J. Lee, "Joint DFT-ESPRIT Estimation for TOA and DOA in Vehicle FMCW Radars," *IEEE Antennas and Wireless Propagation Letters*, vol. 14, pp. 1710–1713, 2015, ISSN: 1536-1225. DOI: `10.1109/LAWP.2015.2420579`.

[43] D. Kissinger, "Radar Fundamentals," in *Millimeter-Wave Receiver Concepts for 77 GHz Automotive Radar in Silicon-Germanium Technology.* Boston, MA: Springer US, 2012, pp. 9–19.

[44] K. Kulpa, *Signal Processing in Noise Waveform Radar*, ser. Radar. Artech House, 2013.

[45] K. Kulpa, K. Lukin, W. Miceli, and T. Thayaparan, "Signal Processing in Noise Radar Technology," *IEE Proceedings, Radar, Sonar and Navigation*, vol. 4, pp. 229–232, Jan. 2008.

[46] S. Lee, C. Du, H. Hashemi, and A. Ortega, "Hardware-driven compressive sampling for fast target localization using single-chip UWB radar sensor," in *Acoustics, Speech and Signal Processing (ICASSP), 2013 IEEE International Conference on*, May 2013, pp. 2601–2605. DOI: `10.1109/ICASSP.2013.6638126`.

[47] J. R. Lievsay and G. A. Akers, "Moving target detection via digital time domain correlation of random noise radar signals," in *2011 IEEE RadarCon (RADAR)*, May 2011, pp. 784–788. DOI: `10.1109/RADAR.2011.5960644`.

[48] T. H. Liu, M. L. Hsu, and Z. M. Tsai, "Mutual interference of pseudorandom noise radar in automotive collision avoidance application at 24 GHz," in *2016 IEEE 5th Global Conference on Consumer Electronics*, Oct. 2016, pp. 1–2. DOI: `10.1109/GCCE.2016.7800400`.

[49] K. Lukin, O. Zemlyaniy, P. Vyplavin, S. Lukin, and V. Palamarchuk, "High resolution and high dynamic range noise radar," in *Microwaves, Radar and Remote Sensing Symposium (MRRS), 2011*, Aug. 2011, pp. 247–250. DOI: `10.1109/MRRS.2011.6053646`.

[50] S. Lutz, C. Erhart, T. Walter, and R. Weigel, "8 channel MIMO long range radar concept for angular estimation in multi target scenarios," in *Microwaves for Intelligent Mobility (ICMIM), 2015 IEEE MTT-S International Conference on*, Apr. 2015, pp. 1–4. DOI: `10.1109/ICMIM.2015.7117955`.

[51] P. Mächler, "VLSI architectures for compressive sensing and sparse signal recovery," PhD thesis, Integrated Systems Laboratory, ETH Zurich, 2013, p. 160.

[52] R. J. Mailloux, *Phased Array Antenna Handbook*, 2nd. Norwood, MA 02062: Artech House, Inc., 2005, ISBN: 1-58053-689-1.

[53] J. S. Marshall, R. C. Langille, and W. M. K. Palmer, "MEASUREMENT OF RAINFALL BY RADAR," *Journal of Meteorology*, vol. 4, no. 6, pp. 186–192, 1947. DOI: `10.1175/1520-0469(1947)004<0186:MORBR>2.0.CO;2`.

[54] J. Martinez Lorenzo, J. Juesas, and W. Blackwell, "Single-transceiver compressive antenna for high-capacity sensing and imaging applications," in *Antennas and Propagation (EuCAP), 2015 9th European Conference on*, Apr. 2015, pp. 1–3.

[55] H. H. Meinel, "Evolving automotive radar — From the very beginnings into the future," in *The 8th European Conference on Antennas and Propagation (EuCAP 2014)*, Apr. 2014, pp. 3107–3114. DOI: `10.1109/EuCAP.2014.6902486`.

[56] H. H. Meinke and F.-W. Gundlach, *Taschenbuch der Hochfrequenztechnik. Grundlagen – Komponenenten – Systeme.* Berlin Heidelberg: Springer, 1992.

[57] M. A. S. Miacci and M. C. Rezende, "Basics on Radar Cross Section Reduction Measurements of Simple and Complex Targets Using Microwave Absorbers," in *Applied Measurement Systems*, M. Z. Haq, Ed., Rijeka: IntechOpen, 2012, ch. 16. DOI: `10.5772/37195`.

[58] L. Michael, D. David, and P. J. M., "Sparse MRI: The application of compressed sensing for rapid MR imaging," *Magnetic Resonance in Medicine*, vol. 58, no. 6, pp. 1182–1195, 2007. DOI: `10.1002/mrm.21391`. eprint: `https://onlinelibrary.wiley.com/doi/pdf/10.1002/mrm.21391`.

[59] M. Mishali and Y. C. Eldar, "From Theory to Practice: Sub-Nyquist Sampling of Sparse Wideband Analog Signals," *CoRR*, vol. abs/0902.4291, 2009. [Online]. Available: `http://arxiv.org/abs/0902.4291;%20http://dblp.uni-trier.de/rec/bib/journals/corr/abs-0902-4291`.

[60] M. Mishali, Y. C. Eldar, O. Dounaevsky, and E. Shoshan, "Xampling: Analog to digital at sub-Nyquist rates," *IET Circuits, Devices & Systems*, vol. 5, no. 1, pp. 8–20, 2011. DOI: `10.1049/iet-cds.2010.0147`.

[61] K. V. Mishra, Z. Slavik, and O. Bringmann, “ReMCW: Reduced Bandwidth FMCW Radar for Autonomous Driving,” in *2019 53rd Asilomar Conference on Signals, Systems, and Computers*, Nov. 2019, pp. 1427–1431. DOI: `10.1109/IEEECONF44664.2019.9048773`.

[62] B. Mullarkey, “The Differences Between Pulse Radars and FMCW Ones,” dB research limited, Tech. Rep., Dec. 2008.

[63] M. Shinriki, R. Sato, and H. Takase, “Multi-range resolution radar using sideband spectrum energy,” in *Radar, 2001 CIE International Conference on, Proceedings*, 2001, pp. 231–235. DOI: `10.1109/ICR.2001.984662`.

[64] U. C. Doyuran and Y. Tanik, “Multi-range and multi-pulse radar detection in correlated non-Gaussian clutter,” in *Radar Conference, 2007. EuRAD 2007. European*, Oct. 2007, pp. 190–193. DOI: `10.1109/EURAD.2007.4404969`.

[65] R. M. Narayanan and C. Kumru, “Implementation of fully polarimetric random noise radar,” *IEEE Antennas and Wireless Propagation Letters*, vol. 4, pp. 125–128, 2005, ISSN: 1536-1225. DOI: `10.1109/LAWP.2005.844653`.

[66] H. J. Ng, R. Feger, and A. Stelzer, “A Fully-Integrated 77-GHz UWB Pseudo-Random Noise Radar Transceiver With a Programmable Sequence Generator in SiGe Technology,” *IEEE Transactions on Circuits and Systems I: Regular Papers*, vol. 61, no. 8, pp. 2444–2455, Aug. 2014, ISSN: 1549-8328. DOI: `10.1109/TCSI.2014.2309774`.

[67] *Nomenclature of the frequency and wavelengh bands used in telecommunications*, EN, Recommendation ITU-R, International Telecommunication Union, Aug. 2015. [Online]. Available: `http://www.itu.int/publ/R-REC/en`.

[68] E. T. Northardt, I. Bilik, and Y. I. Abramovich, “Spatial Compressive Sensing for Direction-of-Arrival Estimation With Bias Mitigation Via Expected Likelihood,” *IEEE Transactions on Signal Processing*, vol. 61, no. 5, pp. 1183–1195, Mar. 2013, ISSN: 1053-587X. DOI: `10.1109/TSP.2012.2232654`.

[69] B. Nuss, L. Sit, and T. Zwick, “A novel technique for interference mitigation in OFDM radar using compressed sensing,” in *2017 IEEE MTT-S International Conference on Microwaves for Intelligent Mobility (ICMIM)*, Mar. 2017, pp. 143–146.

[70] A. Papoulis, *The Fourier Integral and its Applications*, N. York, Ed. McGraw-Hill, 1962.

[71] *Propagation data required for the design of terrestrial free-space optical links*, RECOMMENDATION ITU-R P.1817-1, P Series Radiowave propagation, ITU-R, Geneve, Feb. 2012.

[72] V. Rabinovich and N. Alexandrov, *Antenna Arrays and Automotive Applications*, ser. SpringerLink : Bücher. Springer New York, 2013, ISBN: 9781461410744. [Online]. Available: `https://books.google.de/books?id=6ZpxQ0LKajMC`.

[73] R. Raj and A. Bovik, “A hierarchical Bayesian-map approach to computational imaging,” in *Image Processing (ICIP), 2014 IEEE International Conference on*, Oct. 2014, pp. 1337–1341. DOI: `10.1109/ICIP.2014.7025267`.

[74] F. Ren, R. Dorrance, W. Xu, and D. Markovic, “A single-precision compressive sensing signal reconstruction engine on FPGAs,” in *23rd International Conference on Field programmable Logic and Applications, FPL 2013, Porto, Portugal, September 2-4, 2013*, 2013, pp. 1–4.

[75] J. Romberg, “Compressive Sampling via Random Convolution,” *PAMM*, vol. 7, no. 1, pp. 2 010 011–2 010 012, 2007, ISSN: 1617-7061. DOI: `10.1002/pamm.200700036`.

[76] J. Romberg, “Imaging via Compressive Sampling,” *IEEE Signal Processing Magazine*, vol. 25, no. 21, 2008.

[77] M. Rooker, J. F. López, P. Horstrand, M. Pusenius, T. Leppälampi, R. Lattarulo, J. Pérez, Z. Slavik, S. Sáez, L. Andreu, A. Ruiz, D. Pereira, and L. Zhao, “Validation of Automated Farming,” in *Validation and Verification of Automated Systems: Results of the ENABLE-S3 Project*, A. Leitner, D. Watzenig, and J. Ibanez-Guzman, Eds. Cham: Springer International Publishing, 2020, pp. 271–295, ISBN: 978-3-030-14628-3. DOI: `10.1007/978-3-030-14628-3_20`.

[78] M. Rooker, P. Horstrand, A. S. Rodriguez, S. Lopez, R. Sarmiento, J. Lopez, R. A. Lattarulo, J. M. P. Rastelli, J. Matute, Z. Slavik, D. Pereira, M. Pusenius, and T. Leppälampi, “Towards improved Validation of Autonomous Systems for Smart Farming,” *Workshop on Smart Farming at CPS Week 2018*, 2018.

[79] L. Sakkila, Y. Elhillali, A. Rivenq, C. Tatkeu, and J.-M. Rouvaen, “Short range automotive radar based on UWB pseudo-random coding,” in *Telecommunications, 2007. ITST ’07. 7th International Conference on ITS*, Jun. 2007, pp. 1–6. DOI: `10.1109/ITST.2007.4295848`.

[80] L. Sakkila, A. Rivenq, F. Boukour, C. Tatkeu, Y. E. Hillali, and J. M. Rouvaen, “Collision avoidance radar system using UWB waveforms signature for road applications,” in *Intelligent Transport Systems Telecommunications,(ITST),2009 9th International Conference on*, Oct. 2009, pp. 223–226. DOI: `10.1109/ITST.2009.5399353`.

[81] S. Salemian, H. Keivani, and O. Mahdiyar, “Comparison of radar pulse compression techniques,” in *Microwave, Antenna, Propagation and EMC Technologies for Wireless Communications, 2005. MAPE 2005. IEEE International Symposium on*, vol. 2, Aug. 2005, 1076–1079 Vol. 2. DOI: `10.1109/MAPE.2005.1618106`.

[82] M. Shastry, R. Narayanan, and M. Rangaswamy, “Sparsity-based signal processing for noise radar imaging,” *Aerospace and Electronic Systems, IEEE Transactions on*, vol. 51, no. 1, pp. 314–325, Jan. 2015, ISSN: 0018-9251. DOI: `10.1109/TAES.2014.130733`.

[83] M. Shinriki and K. Hamada, “Multi-range-resolution radar using inverse filters,” *IET Radar, Sonar Navigation*, vol. 2, no. 6, pp. 410–418, Dec. 2008, ISSN: 1751-8784. DOI: `10.1049/iet-rsn:20070186`.

[84] M. Skolnik, *Radar handbook*. McGraw-Hill Education, 1970.

[85] Z. Slavik, O. Bringmann, W. Rosenstiel, and Y. Eldar, “Implications and methods for co-existing automotive radar and communication systems,” in *2018 52nd Asilomar Conference on Signals, Systems, and Computers (to be published)*, invited, Oct. 2018.

[86] Z. Slavik, A. Viehl, T. Greiner, O. Bringmann, and W. Rosenstiel, “Compressive sensing-based noise radar for automotive applications,” in *2016 12th IEEE International Symposium on Electronics and Telecommunications (ISETC)*, Oct. 2016, pp. 17–20. DOI: `10.1109/ISETC.2016.7781046`.

[87] Z. Slavik, O. Bringmann, and W. Rosenstiel, “Approaches for Interference-proof Future Radar Systems,” *Asia Pacific Radio Science Conference*, 2019, invited.

[88] Z. Slavik and M. Ihle, “Compressive Sensing Hardware for Analog to Information Conversion,” *Proceedings of the 8th Karlsruhe Workshop on Software Radios*, pp. 136–144, 2014, Karlsruhe: Communications Engineering Lab.

[89] Z. Slavik and M. Ihle, “Time-of-Flight Messung mittels Compressive Sensing,” in *MPC Workshopband*, Multi Projekt Chip Gruppe Baden Württemberg, vol. 50, Hochschule Ulm, Jul. 2013.

[90] Z. Slavik and K. V. Mishra, “Cognitive interference mitigation strategies for automotive radars,” *Radar Conference*, 2019.

[91] Z. Slavik and K. V. Mishra, “Phenomenological modeling of millimeter-wave automotive radar,” *Asia Pacific Radio Science Conference*, 2019.

[92] I. Slomian, P. Kaminski, J. Sorocki, I. Piekarz, K. Wincza, and S. Gruszczynski, “Multi-beam and multi-range antenna array for 24 GHz radar applications,” in *Microwaves, Radar, and Wireless Communication*

(MIKON), 2014 20th International Conference on, Jun. 2014, pp. 1–4. DOI: `10.1109/MIKON.2014.6899867`.

[93] *Specific attenuation model for rain for use in prediction methods*, RECOMMENDATION ITU-R P.838-3, ITU-R, Geneve, 2005.

[94] W. L. Stutzman and G. A. Thiele, *Antenna theory and design*. John Wiley & Sons, 2013.

[95] W. Susek and B. Stec, "Through-the-wall detection of human activities using a noise radar with microwave quadrature correlator," *Aerospace and Electronic Systems, IEEE Transactions on*, vol. 51, no. 1, pp. 759–764, Jan. 2015, ISSN: 0018-9251. DOI: `10.1109/TAES.2014.130003`.

[96] H. Takase and M. Shinriki, "Search of binary pulse compression codes for multi-range-resolution radar," in *2015 16th International Radar Symposium (IRS)*, Jun. 2015, pp. 1088–1093. DOI: `10.1109/IRS.2015.7226258`.

[97] T. J. Thorson and G. A. Akers, "Near real-time simultaneous range and velocity processing in a random noise radar," in *2012 IEEE Radar Conference*, May 2012, pp. 0585–0590. DOI: `10.1109/RADAR.2012.6212208`.

[98] J. Tropp and A. Gilbert, "Signal Recovery From Random Measurements Via Orthogonal Matching Pursuit," *Information Theory, IEEE Transactions on*, vol. 53, no. 12, pp. 4655–4666, Dec. 2007, ISSN: 0018-9448. DOI: `10.1109/TIT.2007.909108`.

[99] J. A. Tropp, "Greed is good: algorithmic results for sparse approximation," *IEEE Transactions on Information Theory*, vol. 50, no. 10, pp. 2231–2242, 2004. DOI: `10.1109/TIT.2004.834793`.

[100] M. Weiss, "Low-cost, low-power nanosecond pulse radar for industrial applications with mm accuracy," in *Electron Devices for Microwave and Optoelectronic Applications, 2001 International Symposium on*, 2001, pp. 199–204. DOI: `10.1109/EDMO.2001.974307`.

[101] Z. Yang, L. Xie, and C. Zhang, "Off-grid Direction of Arrival Estimation Using Sparse Bayesian Inference," *ArXiv e-prints*, Aug. 2011. arXiv: `1108.5838 [stat.AP]`.

[102] J. Yoo, S. Becker, M. Monge, M. Loh, E. Candès, and A. Emami-Neyestanak, "Design and implementation of a fully integrated compressed-sensing signal acquisition system," in *Acoustics, Speech and Signal Processing (ICASSP), 2012 IEEE International Conference on*, Mar. 2012, pp. 5325–5328. DOI: `10.1109/ICASSP.2012.6289123`.

List of Tables

2.1 ITU Recommendation ITU-R V.431-8 10
2.2 Radar letter designations 11
2.3 Frequency allocation for automotive applications in Germany. ASPD: average spectral power density; P_p: Peak power 12
2.4 Parameter variations in different automotive scenarios 13
2.5 CS Denotations 25
2.6 International Visibility Code and 77 GHz Attenuation 27

3.1 Comparison to the State of the art 47

4.1 Measurement matrix and waveform combinations for proof-of-concept simulation 85
4.2 Proof-of-concept error metrics 91

List of Figures

1.1 Overview objectives and interdependencies 6

2.1 Friis formula for two-way radar signal propagation 14
2.2 Principle of pulsed radar 16
2.3 CCF output of pulsed radar 17
2.4 Principle of FMCW radar 19
2.5 Beat frequency at FMCW receiver 20
2.6 Simplified CS principle of signal acquisition and reconstruction. Left hand side: Measurement of x and projection into observation b. Right hand side: Reconstruction $\hat{x}$ is determined by finding the only measurement vector in A that explains the observation b 24
2.7 Rain attenuation vs pathlength 29
2.8 Rain attenuation vs rain rate 29

4.1 Radar function blocks for CS applications 52
4.2 Block diagram of RMPI radar hardware architecture 56
4.3 Reconstruction accuracy for RMPI receiver over subsampling rate and SNR 57
4.4 RMPI based radar: time error 58
4.5 RMPI based radar: amplitude error 59
4.6 Reconstruction dependency in RMPI receiver systems on sparsity-dependent number of measurements 60
4.7 Original raw SAR data 61
4.8 Reconstructed raw SAR data 62
4.9 SAR images 63
4.10 Linear phased array antenna with three elements in Cartesian coordinates 65
4.11 Effect on antenna pattern for different carrier frequencies at a fixed antenna spacing according to $\lambda/2$, $f_c = 78$ GHz 66
4.12 Principle of CS based signal acquisition of a linear antenna array . . . 69
4.13 In contrast to CCF receivers, the correlation output is integrated over maximum pulse roundtrip time. 72
4.14 Transmit waveforms in time and frequency domain with Figure 4.14 a white noise and Figure 4.14 b random noise. 74
4.15 Analysis of Gram matrices 81

4.16 Gram of full correlation matrix 82
4.17 Gram of reduced correlation matrix 83
4.18 Relative error in range depending on sub-sampling rate in percent and SNR level for bandlimited white noise transmit waveform. Short range performance is represented with a target located at 30 m for Figure 4.18 a M1 (reduced correlation measurement matrix) and Figure 4.18 b M2 (random measurement matrix). Long range performance is tested with a target at 270 m for Figure 4.18 c M1 and Figure 4.18 d M2. 87
4.19 Boxplots to evaluate the relative mid-range error for M1 regarding Figure 4.19 a SNR and Figure 4.19 b sub-sampling. Same for M2 with Figure 4.19 c SNR and Figure 4.19 d sub-sampling. 88
4.20 Relative error in range depending on sub-sampling rate in percent and SNR level. Short range performance is represented with a target located at 30 m for Figure 4.20 a M3 and Figure 4.20 b M4. Long range performance is tested with a target at 270 m for Figure 4.20 c M3 and Figure 4.18 d M4. 89
4.21 Boxplots to evaluate the relative mid-range error for M3 regarding Figure 4.21 a SNR and Figure 4.21 b sub-sampling. Same for M4 with Figure 4.21 c SNR and Figure 4.21 d sub-sampling. 90
4.22 Boxplots to evaluate the relative error for M1 regarding Figure 4.22 a SNR at short range and Figure 4.22 b sub-sampling at long range. Same for M3 with Figure 4.22 c SNR for short range and Figure 4.22 d sub-sampling for long range. 92

5.1 Demonstration work flow: Real world radar sensor and measurements (orange) are used to generate virtual models and systems (blue). The real and virtual radar are validated with point-wise measurements in LFMCW mode (green). 95
5.2 INRAS' Radarbook with mounted 77 GHz RF frontend 96
5.3 Configurable chirp parameters on radar development board 97
5.4 Corner reflector measurements: Figure 5.4 a shows the Radarbook and the host PC and Figure 5.4 b depicts the measurement setting with a corner reflector placed 3 min front of the radar. The range profile is displayed in Figure 5.4 c for 1 GHz bandwidth and in Figure 5.4 d for 4 GHz bandwidth. 100
5.5 Begin of far field region for different TX antenna postions. 101
5.6 Experiment setup for static measurement of rain effects: Figure 5.6 a radar mounted on railing, Figure 5.6 b geometry of targets and radar 102
5.7 Different constant attenuation due to radome water coverage 104
5.8 Different constant attenuation due to radome water coverage 106
5.9 Peak level attenuation during various levels of water coverage. 107

5.10 Schematic of radar system simulation domains. 109
5.11 Microstrip patch element. In Figure 5.11 a the modeled parameters are visualized and in Figure 5.11 b the directivity of a single patch element is given. 111
5.12 Receive and transmit antennas: (1) is a single patch element, (2) a single receive antenna and (3) a single transmit antenna. 111
5.13 Directivity of Figure 5.13 a single RX array, Figure 5.13 b superposed RX arrays and Figure 5.13 c a single TX array. Directivity cut of Figure 5.13 a single RX array, Figure 5.13 b superposed RX arrays and Figure 5.13 c a single TX array. 112
5.14 Measurement results for a corner reflector placed at a distance of 3 m: Figure 5.14 a resulting range profile with peak at 3 m and additional peaks obtained by the environment, Figure 5.14 b measured range-azimuth map and Figure 5.14 c normalized measured range-azimuth-map. Simulation results for single point-scattering target at 3 m: Figure 5.14 d simulated range profile with no additional scatterers, Figure 5.14 e according simulated range-azimuth map and Figure 5.14 f normalized simulated range-azimuth map. 113
5.15 Co-Simulation with agricultural environment simulation. Figure 5.15 a The radar is mounted on the harvester. The trailer is modeled as point target with adequate RCS. Figure 5.15 b shows the resulting radar output that indicates the trailer as a peak. 114
5.16 Noise radar system simulation 117
5.17 Range profile for different sub-sampling rates, i.e. Figure 5.17 a $\frac{M}{N} = 0.1$, Figure 5.17 b $\frac{M}{N} = 0.3$ and Figure 5.17 c $\frac{M}{N} = 0.5$ for the noise radar system and Figure 5.17 d of reference LFMCW system. Accordingly, range-Doppler maps for different sub-sampling rates, i.e. Figure 5.17 e $\frac{M}{N} = 0.1$, Figure 5.17 f $\frac{M}{N} = 0.3$ and Figure 5.17 g $\frac{M}{N} = 0.5$ for the noise radar system and Figure 5.17 h of reference LFMCW system. . . 118
5.18 Range profile for different sub-sampling rates, i.e. Figure 5.18 a $\frac{M}{N} = 0.1$, Figure 5.18 a $\frac{M}{N} = 0.3$ and Figure 5.18 a 119
5.19 Range profiles after interference from second radar system of same architecture for Figure 5.19 a LFMCW radar receive and Figure 5.19 b noise modulated correlation receiver. 120
5.20 Scenario of LFMCW radar system interfered by noise radar system . . 122

MIMO-77GHz RF-Frontend

MIMO-77-TX4RX8 Frontend

(Preliminary User Manual)

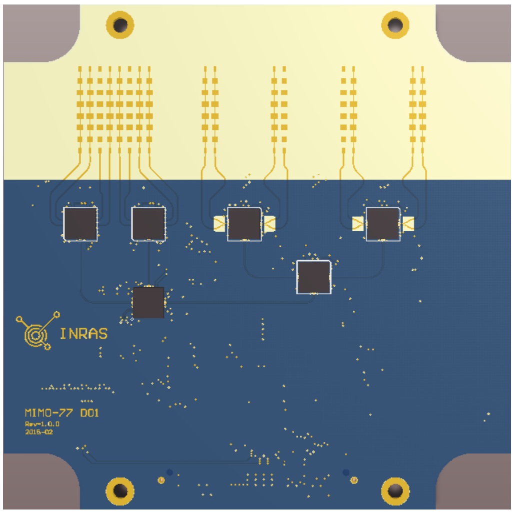

Inras GmbH
Altenbergerstraße 69
4040 Linz, Austria
Email: office@inras.at
Phone: +43 732 2468 6384

Linz, 19.12.2014

Contents

1 Document Version 2

2 Hardware Version 2

3 77-GHz MIMO Frontend 3
  3.1 Features of the FMCW Radar System . . . 4

4 Technical Data of the MIMO Frontend 5
  4.1 Mechanical Data . . . 5
  4.2 Antenna Configuration . . . 6
  4.3 Electrical Parameters . . . 7
  4.4 Frontend Connector . . . 8

5 Frontend Configuration with Radarbook 10
  5.1 RF Device Configuration with SPI Interface . . . 11
  5.2 IFTX Digital Power Control with SEQTRIG MMP . . . 12

6 List of Abbreviations 13

1 Document Version

Version	Description	Date	Author
1.0.0	Initial Version	2015-02-18	Andreas Haderer (AnHa)
1.0.1	Rename device drivers	2015-06	Andreas Haderer (AnHa)

2 Hardware Version

Board Name	Revision	Date
MIMO-77-TX4RX8	1.0.0	2015-05

3 77-GHz MIMO Frontend

In Fig. 1 the block diagram of the 77-GHz frontend with four transmit (TX) and eight receive (RX) antennas is shown. The frontend is designed to enable MIMO radar processing for FMCW waveforms with multiple transmit antennas. The TX antennas can be activated by means of digital signals in an arbitrary manner in order to implement a virtual array with improved angular resolution capabilities. According to the block diagram, a RTN7735 in conjunction with the RCC1010 is used to generate the FMCW transmit signal. The four transmit antennas (TX1 - TX4) are fed from RPN7720 dual power amplifiers and can therefore be activated in an arbitrary sequence by means of digital control signals. The activation sequence can be programmed with the trigger and timing unit implemented in the FPGA of the Radarbook. In addition, the general purpose output signals of the RCC1010 can be used to control the activation of the TX antennas. The receive path on the left side of the frontend is realized with two RRN7745 receivers. The LO signal for the receiver chips is provided by the first two RF outputs of the RTN7735. The remaining RF output is used to drive the transmit circuitry of the frontend. The naming convention for the RPN7720 (IFTX1 - IFTX3) and the receive chips (IFRX1 and IFRX2), depicted in the block diagram, is used in the software framework of the Radarbook to access the different devices. This is required to program defined activation sequences for the transmit antennas. For example the first RF output of IFTX1 is used to activate the transmit antenna TX1 and the second output is used for antenna TX2. In the following section the main features of the evaluation plattform consisting of the MIMO frontend

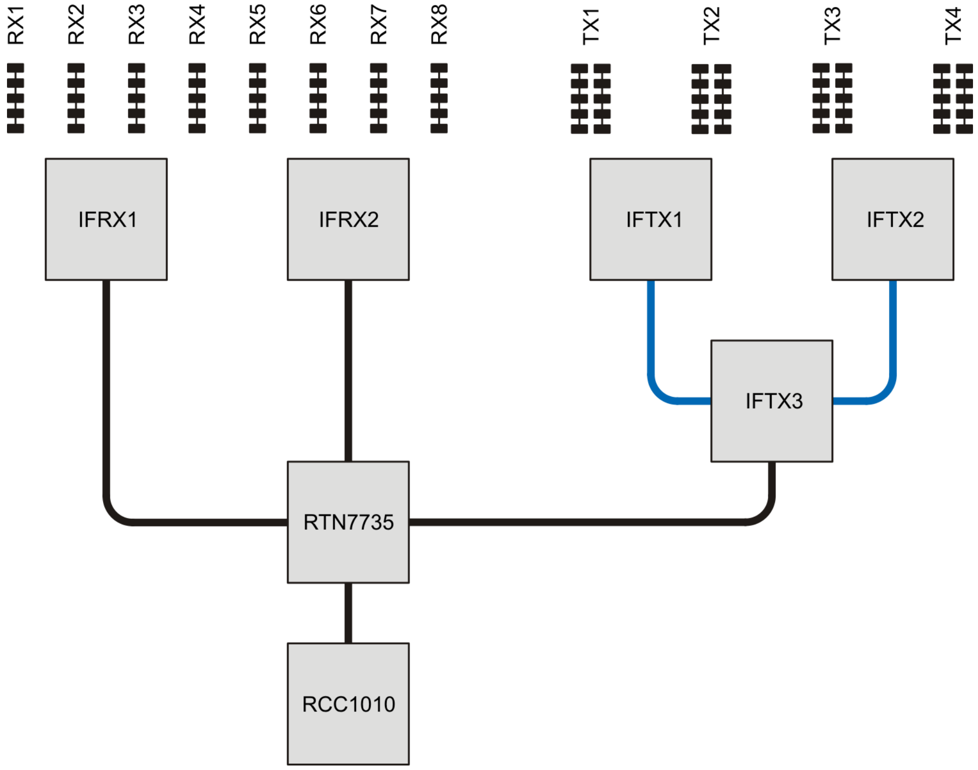

Figure 1: Antenna configuration and naming convention for MIMO frontend.

in conjunction with the Radarbook are summarized.

3.1 Features of the FMCW Radar System

The frontend is designed to operate with the Radarbook and can be configured freely to the needs of the application at hand. The main features of the frontend include

- Four TX channels,
- Eight RX channels (RRN7745) with differential IF outputs,
- Amplitude power control for all four transmit channels,
- Analog signals for power and temperature monitoring,
- Differential signals for clock synchronization (input and output of RF clock), and
- Frontend identification and storage of calibration data by means of an integrated EEPROM.

The frontend can be operated with the Radarbook. The Radarbook offers a TCP/IP or a USB 3.0 interface, which can be used to configure the modes of operation for the FMCW radar system. The timing of the FMCW waveform as well as the FMCW ramp parameters can be programmed and the IF signals can be recorded in real-time. The main features provided by the Radarbook include

- Sampling rates up to 20 MSPS per IF channel,
- Ramp synchronous sampling,
- Arbitrarily programmable FMCW timing,
- MIMO processing with arbitrary antenna activation,
- Configurable signalprocessing, and
- 100 MBit TCP/IP or USB 3.0 interface.

4 Technical Data of the MIMO Frontend

In the following sections the mechanical and the electrical parameters of the frontend are summarized.

4.1 Mechanical Data

The frontend is built to interface with the Radarbook. In Fig. 2 the dimensions of the board as well as the position of the mounting holes are depicted. In Tab. 1 the dimensions of the frontend and its weight are summarized. In the current version the frontend is very lightweight as now additional heat sink is integrated on the frontend.

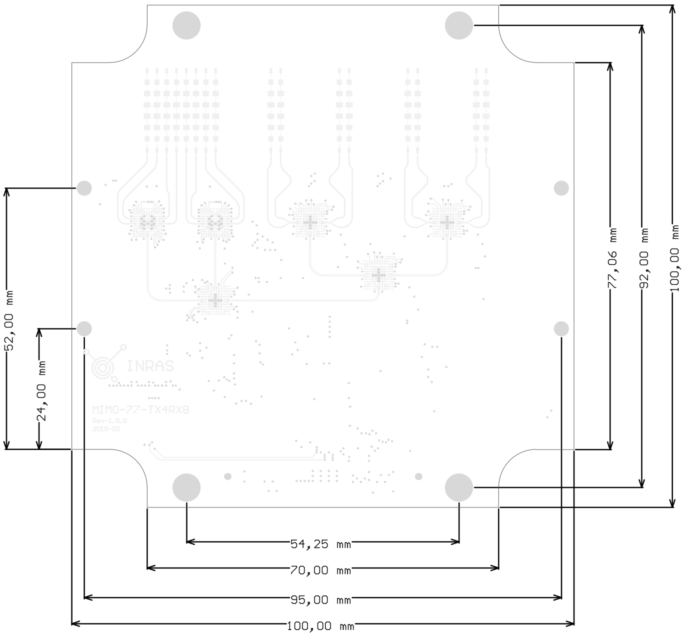

Figure 2: Dimensions of the MIMO frontend including the position of the mounting holes.

Parameter	Value
Substrate	RO-3003
Dimension x-direction	100 mm
Dimension y-direction	100 mm
Weight frontend	40 g
Weight (frontend and Radarbook)	177 g
Weigth (frontend, Radarbook, and housing)	410 g

Table 1: Mechanical parameters of the MIMO frontend.

An Altium template containing the contour and position of the frontend connector is available on request.

4.2 Antenna Configuration

The positions of the transmit and receive antennas are shown in Fig. 3. The origin of the Cartesian coordinate system is located at the receive antenna RX_1. In Tab. 2 the x-coordinates of the antennas are summarized. All mentioned positions are in mm.

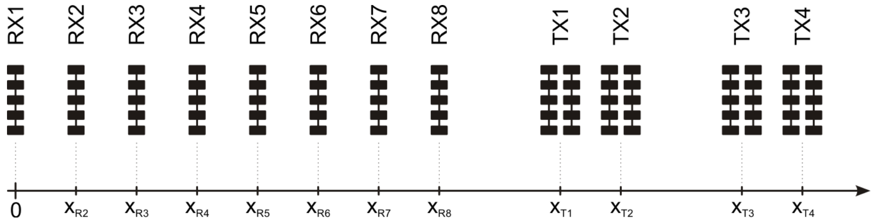

Figure 3: Antenna positions of the MIMO RF frontend.

TX Antenna	x-Position (mm)	RX Antenna	x-Position (mm)
TX1	25.614	RX1	0.000
TX2	39.250	RX2	1.948
TX3	52.887	RX3	3.896
TX4	66.523	RX4	5.844
		RX5	7.792
		RX6	9.740
		RX7	11.690
		RX8	13.640

Table 2: Positions of transmit and receive antennas.

The receive antennas are buílt with serial fed patch antennas with eight elements. The transmit elements use two serial fed patch antennas which are fed from the differential output signal of the power amplifier.

	Parameter	Value	Unit
G_{RX}	Realized Gain (RX)	15.8	dBi
ΔS_{RX}	Sidelobe suppression (RX)	-18	dB
Θ_{H}	Horizontal 3 dB beamwidth (RX)	76.5	°
Θ_{V}	Vertical 3 dB beamwidth (RX)	12.8	°
G_{TX}	Realized Gain (TX)	17.2	dBi
ΔS_{TX}	Sidelobe suppression (TX)	-14	dB
Θ_{H}	Horizontal 3 dB beamwidth (TX)	51	°
Θ_{V}	Vertical 3 dB beamwidth (TX)	13.2	°

Table 3: Antenna parameters.

4.3 Electrical Parameters

In Tab. 4 the electrical parameters of the frontend are specified.

	Parameter	Condition	Min	Typ	Max	Unit
V_{C1}	Supply voltage C1	-	3.2	3.3	3.4	V
V_{C2}	Supply voltage C2	-	4.9	5.0	5.1	V
V_{C3}	Supply voltage C3	-	3.2	3.3	3.4	V
I_{C1}	Supply current C1	@ 3.3 V / all TX enabled	-	-	2100	mA
I_{C2}	Supply current C2	@ 5.0 V	-	-	200	mA
I_{C3}	Supply current C3	@ 3.3 V	-	-	860	mA
P_t	Max RF output power	-		10		dBm
-	TX/TX isolation		22			dB
f_t	Transmit frequency		76	-	77	GHz

Table 4: Electrical parameters of the frontend.

For a more detailed description of the electrical parameters refer to the data sheet of the transceivers (RPN7720 and RRN7745).

4.4 Frontend Connector

The frontend connector is used to interface the frontend with the Radarbook. The connector supports three programmable supply voltages, 24 digital control signals for the configuration of the frontend, 12 differential IF signals, and four analog signals for status monitoring. In Fig. 4 the schematic of the connector is shown.

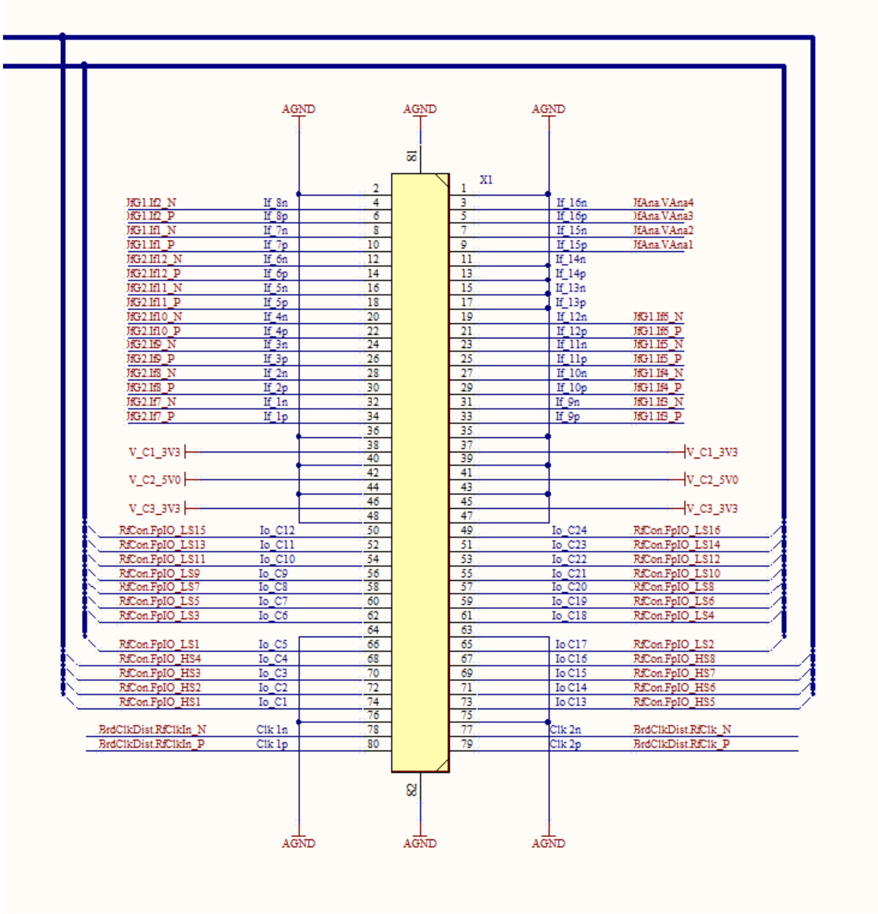

Figure 4: Schematic of the frontend connector.

The digital control signals are used for operating and testing the FMCW frontend. The digital signals require a 3.3 V CMOS standard. The configuration of the receivers and the power amplifier is done with an SPI interface. The reveivers and the power amplifier in the transmit path share a common SPI interface named (Cfg). The RCC1010 uses a separate SPI interface in order to enable a fast reconfiguration of the waveform generateion.

PIN	Signal Radarbook	Signal Frontend	Description
74	FpIO_HS1	SpiCfg.Ena_IFTX2	SPI enabale for IFTX2 (Cfg)
72	FpIO_HS2	SpiCfg.Ena_IFTX3	SPI enabale for IFTX3 (Cfg)
70	FpIO_HS3	SpiCfg.Ena_IFTX1	SPI enabale for IFTX1 (Cfg)
68	FpIO_HS4	SpiCfg.So	SPI slave data output (Cfg)
73	FpIO_HS5	IFTXPaCon.IFTX2_2	Power control PACON2 for IFTX 2
71	FpIO_HS6	IFTXPaCon.IFTX2_1	Power control PACON1 for IFTX 2
69	FpIO_HS7	IFTXPaCon.IFTX1_2	Power control PACON2 for IFTX 1
67	FpIO_HS8	IFTXPaCon.IFTX1_1	Power control PACON1 for IFTX 1

Table 5: Digital control signals for operating the FMCW frontend.

PIN	Signal Radarbook	Signal Frontend	Description
66	FpIO_LS1	SpiCfg.Ena_IFRX2	SPI enabale for IFRX2 (Cfg)
65	FpIO_LS2	IFTXPaCon.IFTX3_1	Power control PACON1 for IFTX 3
62	FpIO_LS3	SpiCfg.Ena_IFRX1	SPI enabale for IFRX1 (Cfg)
61	FpIO_LS4	SpiCfg.Si	SPI slave data input (Cfg)
60	FpIO_LS5	Rx_DigTst	Digital test input (RX1 and RX2)
59	FpIO_LS6	SpiCfg.Clk	SPI clock (Cfg)
58	FpIO_LS7	Rcc.Demux1	RCC1010 Demux 1 signal
57	FpIO_LS8	Rcc.Demux2	RCC1010 Demux 2 signal
56	FpIO_LS9	Rcc.Rst	RCC1010 Reset signal
55	FpIO_LS10	Rcc.SpiClk	RCC1010 SPI clock signal
54	FpIO_LS11	Rcc.SpiSi	RCC1010 SPI slave data input
52	FpIO_LS13	Rcc.SpiSo	RCC1010 SPI slave data output
50	FpIO_LS15	Rcc.SpiEna	RCC1010 SPI enable

Table 6: Digital control signals for operating the FMCW frontend.

PIN	Signal Radarbook	Signal Frontend	Description
8,10	IFG1.IF1_P_N	IF.4_P_N	IF signal IFRX1
4,6	IFG1.IF2_P_N	IF.3_P_N	IF signal IFRX2
31,33	IFG1.IF3_P_N	IF.6_P_N	IF signal IFRX7
27,29	IFG1.IF4_P_N	IF.5_P_N	IF signal IFRX8
32,34	IFG2.IF7_P_N	IF.8_P_N	IF signal IFRX5
28,30	IFG2.IF8_P_N	IF.7_P_N	IF signal IFRX6
24,26	IFG2.IF9_P_N	IF.2_P_N	IF signal IFRX3
20,22	IFG2.IF10_P_N	IF.1_P_N	IF signal IFRX4

Table 7: Analog IF signals for the receive channels.

5 Frontend Configuration with Radarbook

The RF frontend can be operated in connection with the Radarbook. The frontend connector is used to supply and configure the 77-GHz frontends by means of the FPGA. In the following sections the implemented device drivers and the commands for accessing the drivers are explained in more detail. The logical mapping of the transceivers is required to configure and operate the frontend.

The FPGA software of the Radarbook provides device drivers for the different RF chips. In Fig. 5 the software components being used for configuring and operation the frontend are shown. The drivers for configuring the sampling chain and for the power supply are not included in the block diagram. The command interface accepts standardized commands from different interfaces (ARM, RS232) and forwards the commands to the implemented device drivers. The command header is used to select the device driver and if multiple devices of the same type are present (e.g. three IFTX devices, or two receive chips) then a bitmask is used to address the desired component. The use of a bitmask allows to access multiple devices with a single command. The RF chips assembled to the frontend are accessed by means of SPI compatible interfaces. Therefore, the device drivers for IFTX, RCC, and IFRX use SPI interfaces (USPIF and USPI8) to access the chips of the frontend. The USPIF features four SPI interfaces sharing a common clock and data signal whereas the USPI8 MMP features up to 8 SPI interfaces.

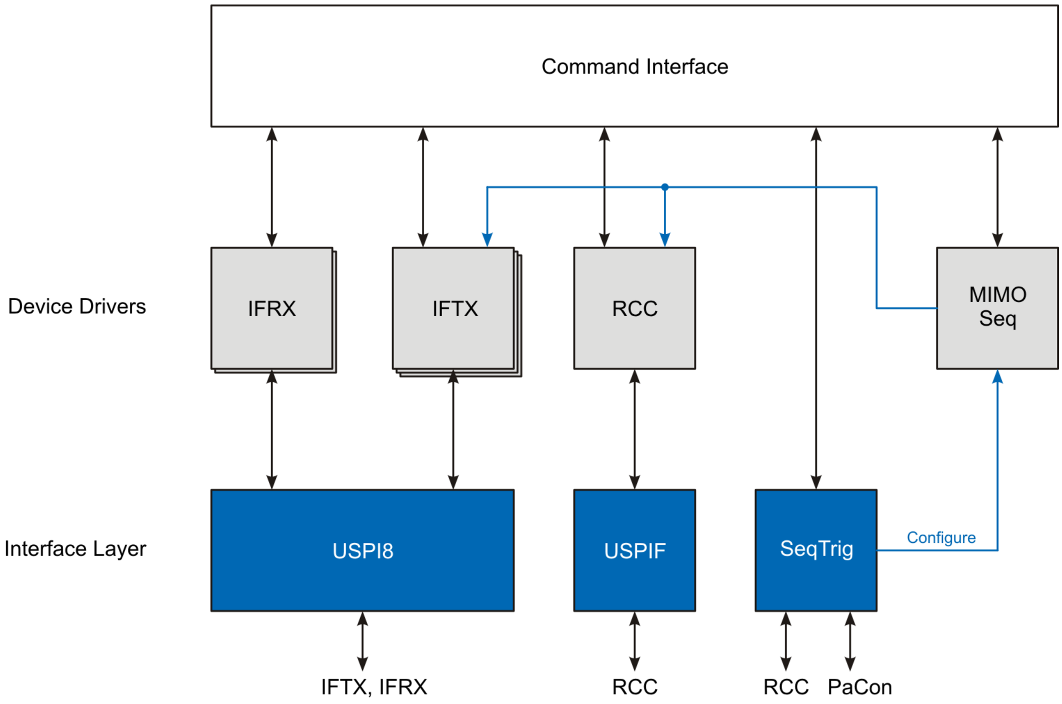

Figure 5: Software architecture and device drivers for frontend configuration.

In addition, the Radarbook drives the PACON inputs of the RPN7720 devices of the RF frontend. The PACON signals are connected to the digital configuration Chn0Cfg of the SEQTRIG

MMP. This enables the activation of different transmit antennas for subsequent measurement cycles. The mapping of the PACON signals is described in Sec. 5.2.

5.1 RF Device Configuration with SPI Interface

To configure the frontends, SPI compatible interfaces (USPIF and USPI8) are used. The USPIF is used to interface the RCC1010. The USPIF MMP provides a fully configurable SPI interface for four distinct SPI channels with a common clock and common MOSI and MISO data signals. In addition, the MMP includes a transmit and receive FIFO to enable fast block transfers without interaction from the softcore controller. In the implemented FPGA framework the RCC1010 does not share its MOSI and MISO signals with other devices in order to ensure a fast configuration of the FMCW radar system. The channel mapping of the implemented USPIF interface is listed in Tab. 8. The RCC1010 is connected to channel 0 of the USPIF MMP.

MMP	Chn	RF Device
USPIF	0	RCC1010
USPIF	1	Not connected
USPIF	2	Not connected
USPIF	3	Not connected

Table 8: Channel mapping of the USPIF MMP.

The USPI8 is compatible to the USPIF interface but offers eight distinct chip enable signals. Hence, eight devices with a common MOSI and MISO signal can be accessed from a single MMP. Each channel has its own set of configuration registers. The USP8 is used to access the IFTX devices as well as the four receiver chips. In Tab. 9 the channel mapping of the USPI8 interface is summarized.

MMP	Chn	RF Device
USPI8	0	IFTX1
USPI8	1	IFTX2
USPI8	2	IFTX3
USPI8	4	IFRX1
USPI8	5	IFRX2

Table 9: Channel mapping of the USPI8 MMP.

The different transceiver chips can be accessed by the SPI interfaces. In order to simplify the configuration, the software implements device drivers for the different RF chips. In the following section the device drivers for the transmit IFTX and the receive devices IFRX are described in more detail.

5.2 IFTX Digital Power Control with SEQTRIG MMP

The SEQTRIG MMP is used to program the timing of the transmit waveform and in addition it enables the control of the PACON signals of the IFTX devices. These signals can be used to control the output power of all IFTX devices, if the power control is activated in the IFTX power control registers. Therefore, the signals can be used to digitally control the activation of the four transmit antennas. In Fig. 6 the output signals of the SEQTRIG MMP are shown. The Chn0Cfg configuration word is used to control the PACON signals of the transmit power distribution. A single bit of the configuration word is used to set the signal during a phase. Hence, the configuration words can be used to select the desired transmit antenna. In Tab. 10 the routing of the PACON signals is summarized.

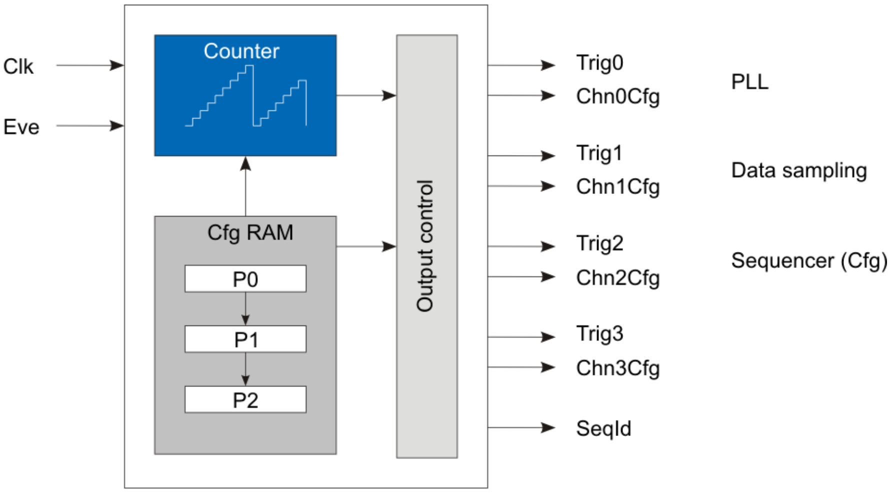

Figure 6: Output signals of the SEQTRIG MMP.

In Tab. 10 the signal name D1_PC1 refers to the PACON1 signal of IFTX1 and D1_PC2 to the PACON2 signal of IFTX1.

D07	D06	D05	D04	D03	D02	D01	D00
-	-	-	D3_PC1	D2_PC2	D2_PC1	D1_PC2	D1_PC1

Table 10: Byte 0 of configuration word Cfg0 of SEQTRIG MMP.

6 List of Abbreviations

CAN	...	Controller Area Network
FIFO	...	First In First Out
FMCW	...	Frequency-Modulated Continuous Wave
FPGA	...	Field Programmable Gate Array
MMP	...	Memory Mapped Peripheral
MIMO	...	Multiple Input Multiple Output
MISO	...	Master In Slave Out
MOSI	...	Master Out Slave In
RF	...	Radio Frequency
RX	...	Receive
SEQTRIG	...	Sequence Trigger Unit
SPI	...	Serial Peripheral Interface
TX	...	Transmit
USPIF	...	Universal Serial Peripheral Interface with FIFO

Background to related methods

1 Mathematics

1.1 Fourier Transformation

The duality of the Fourier transformation comprises the following properties.

$$\mathrm{e}^{j\omega_0 t}x(t) \multimap X(\omega - \omega_0) \tag{1}$$

$$x(t - t_0) \multimap \mathrm{e}^{-j\omega t_0}X(\omega) \tag{2}$$

$$ax(t) + by(t) \multimap aX(\omega) + bY(\omega) \tag{3}$$

$$x(at) \multimap \frac{1}{|a|}X(\frac{\omega}{a}) \tag{4}$$

$$\frac{\partial}{\partial t}x(t) \multimap j\omega X(\omega) \tag{5}$$

$$x(t) * y(t) \multimap X(\omega) \cdot Y(\omega) = \int_{-\infty}^{\infty} x(\tau)h(t - \tau)\,\mathrm{d}\,\tau \tag{6}$$

$$x(t) \cdot y(t) \multimap \frac{1}{2\pi}\int_{-\infty}^{\infty} X(\gamma)Y(\omega - \gamma)\,\mathrm{d}\,\gamma \tag{7}$$

1.2 Information and signal theory

Cauchy-Schwarz inequality with real $x_1(t), x_2(t)$

$$\left[\int_{-b}^{b} x_1(t) \cdot x_2(t)\,\mathrm{d}\,t\right]^2 \leqslant \int_{-b}^{b} x_1(t)^2\,\mathrm{d}\,t \int_{-b}^{b} x_2(t)^2\,\mathrm{d}\,t \tag{8}$$

2 CS Algorithms

2.1 OMP

```
%% Orthogonal Matching Pursuit
%----------------------------------------------------------------------------%
% [Tropp2007]: Signal Recovery From Random Measurement Via Orthogonal
% Matching Pursuit
%----------------------------------------------------------------------------%
% Input:
%          Phi        Nxd measurement matrix
%          v          Nx1 observation vector (data vector)
%          m:         level of sparsity (ideal vector)
%
% Output:
%          s_hat      dx1 estimate of ideal signal
%          Lm         mx1 Index vector, containing m elements from
%                     {1,..,d}
%          am         Nx1 approximation of observation
%          rm         Nx1 residual rm=v-am
%
% Revision
%   Version | Date          | Author         |
%   V1.0    | 30.09.2015    | Zora Slavik    |  init version
%   V1.1    | 09.02.2016    | Zora Slavik    |  subst. ls_solver
%%%%%%%%%%%%%%%%%%%%%%%%%%%%%%%%%%%%%%%%%%%%%%%%%%%%%%%%%%%%%%%%%%%%%%%%%%%%


%function [s_hat,Lm,am,rm]=omp2(Phi,v,m)

% Init
s_hat=zeros(length(Phi),1);
Lm=zeros(m,1);
rm=v;

eps=1e-6;

for t=1:1:m

   % index for maximal spatial product
   [val,Lm(t,1)]=max(Phi'*rm);
   % update subspace of measurement matrix Phi_t
```

```
   Phi_t(:,t)=Phi(:,Lm(t,1));

   % LS: min||v-Phi_t*xt||_2
   xt=general_inverse(Phi_t)*v;
   %xt=ls_solver(Phi_t,v);

   % update data approximation
   am=Phi_t*xt;
   %update residual
   rm=v-am;

   if(norm(rm,2)<eps)
        s_hat(Lm(Lm~=0))=xt;
        return;
   end

end

s_hat(Lm(Lm~=0))=xt;
```

2.2 CAMP

```
%% Complex Approximate Messsage Passing (CAMP)
%----------------------------------------------------------------------------%
% [Anitori2012]: Compressive CFAR radar detection
%----------------------------------------------------------------------------%
% input:
%           b           observation
%           A           reconstruction matrix
%           thr         user defined threshold
%           dthr        threshold step, only for adaptive approach
%           delta       sets residual step
% output:
%           x_hat       resulting x estimate
%           x_est       residual estimate
%           sigma_hat   estimated standard deviation of the total noise
%
% Revision
%   Version | Date          | Author        |
%   V1.0    | 23.09.2015    | Zora Slavik   |
%%%%%%%%%%%%%%%%%%%%%%%%%%%%%%%%%%%%%%%%%%%%%%%%%%%%%%%%%%%%%%%%%%%%%%%%%%%%%%%%
```

```
function [x_hat,x_est,sigma_hat]=camp(A,b,thr,dthr,delta)

% Init
if isempty(dthr)
    tthr=thr;
else
    tthr=thr:-dthr:0;
end

X_hat=zeros(length(A),length(tthr));
X_est=zeros(length(A),length(tthr));
Sigma_hat=zeros(1,length(tthr));
x_hat=zeros(length(A),1);
z=b;
maxiter=100;

for l=1:length(tthr)

    for t=1:maxiter

       x_est=A.'*z+x_hat;

       sigma_hat=median(abs(x_hat))*sqrt(2/log(4));
       x_hat=zeros(size(x_hat));

       u=real(x_est);
       v=imag(x_est);
       lambda=tthr(l)*sigma_hat;

       ii=find((u.^2+v.^2>lambda^2));
       dnr=1+lambda*(sqrt(u(ii).^2+v(ii).^2)-u(ii).^2./...
       ... sqrt(u(ii).^2+v(ii).^2))./(u(ii).^2+v(ii).^2);
       dni=1-lambda*(sqrt(u(ii).^2+v(ii).^2)-v(ii).^2./...
       ... sqrt(u(ii).^2+v(ii).^2))./(u(ii).^2+v(ii).^2);

       mdn=mean(dnr)+mean(dni);

       if isnan(mdn)
           mdn=0;
       end

       zn=b-A*x_hat+z/(2*delta).*(mdn);
```

```
        z=zn;

        x_hat(ii)=u(ii)+i*v(ii)-(lambda*(u(ii)+i*v(ii)))./...
        ... (sqrt(u(ii).^2+v(ii).^2));

    end

    X_hat(:,l)=x_hat;
    X_est(:,l)=x_est;
    Sigma_hat(:,l)=sigma_hat;

end

[sigma_hat,ind]=min(Sigma_hat);
x_hat=X_hat(:,ind);
x_est=X_est(:,ind);
```

2.3 ROMP

```
%% Regularized Orthogonal Matching Pursuit
%-----------------------------------------------------------------------%
% [Needell2007]: Signal Recovery From Incomplete and Inaccurate
% Measurements via Regularized Orthogonal Matching Pursuit
%-----------------------------------------------------------------------%
% Input:
%      v           observation vector (data)
%      Phi         measurement matrix
%      k           sparsity
% Output:
%      x_hat       reconstruction of ideal original signal
%      Lm          index set
%      am          data approximation
%      rm          residuals
%
% V1.1: Reimplement subset selection according to "The stability of
% regularized orthogonal matching pursuit algorithm". Nguyen, Nam H.
% and Tran, Trac D. .
% http://dsp.rice.edu/sites/dsp.rice.edu/files/cs/Stability_of_ROMP.pdf
%
% Revision
%   Version | Date          | Author         |
%   V1.0    | 30.09.2015    | Zora Slavik    |
```

```
%   V1.1    | 23.10.2015    | Zora Slavik    |
%%%%%%%%%%%%%%%%%%%%%%%%%%%%%%%%%%%%%%%%%%%%%%%%%%%%%%%%%%%%%%%%%%%%%%%%%%%

function [x_hat,Lm,am,rm]=romp(Phi,v,k)

% Init
x_hat=zeros(length(Phi),1);
Lm=0;
rm=v;
[m,n]=size(Phi);
Phi_t=zeros(m,k);
Lm=zeros(1,k);

for t=1:1:k

   %1. Identify:
   % spatial products u
   u=Phi'*rm;
   % find k biggest spatial products
   [u,ind]=sort(abs(u),'descend');
   % excluding entries equal to zero
   Lm_set=ind(u(1:k)~=0);
   uj=u(Lm_set);

   %regularize subsets
   diff=2*abs(circshift(uj,[1,-2]))-abs(uj);
   kk=ind(diff>=0);

   % find the subset with biggest value energy ||uj||_2
   %[val,kk]=max(norm(uj(diff>=0),2));
   Lm(t)=kk(1);
   % update subspace of measurement matrix Phi_t
   Phi_t(:,t)=Phi(:,Lm(t));
   % LS: min||v-Phi_t*xt||_2
   xt=general_inverse(Phi_t(:,1:t))*v;
   % update data approximation
   am=Phi_t(:,1:t)*xt;
   %update residual
   rm=v-am;
end

x_hat(Lm)=xt;
```

2.4 BPDN

```
%% Basis Pursuit - Primal-Dual IP
%-----------------------------------------------------------------------------%
% []: Primal-Dual Interior Point algorithms for Linear Programming
% George Tzallas-Regas
%-----------------------------------------------------------------------------%
% Input:
%           A           Nxd measurement matrix
%           b           Nx1 observation vector (data vector)
%           kk          level of sparsity (ideal vector)
%
% Output:
%           s_hat       dx1 estimate of ideal signal
%           Lm          mx1 Index vector, containing m elements from
%                       {1,..,d}
%           am          Nx1 approximation of observation
%           rm          Nx1 residual rm=v-am
%
% Revision
%   Version | Date          | Author          |
%   V1.0    | 23.10.2015    | Zora Slavik     |
%   V1.1    | 11.02.2016    | Zora Slavik     |  fixed issues with matrix
%           |               |                 |  inversion, added
%           |               |                 |  termination criterion
%%%%%%%%%%%%%%%%%%%%%%%%%%%%%%%%%%%%%%%%%%%%%%%%%%%%%%%%%%%%%%%%%%%%%%%%%%%%%

%function x_hat=bppdip(A,b,kk)

% Init
x=A'*b;
s=x;
s(s<0)=0;
y=A*(1-s);

[m,n]=size(A);

epsilon=1e-3;
gamma=(x.'*s)/n;

alpha=1;
count=200;
```

```
cc=1;

while abs(gamma)>epsilon && cc<=count

    if ~(any(s==0))
        invs=1./s;
        invS=diag(invs);
    else
        invS=general_inverse(diag(s));
    end

    dy=general_inverse(A*diag(x)*invS*A.')*(b-A*invS*gamma*ones(n,1));

    ds=-A.'*dy;
    dx=invS*gamma*ones(n,1)-diag(x)*ones(n,1)-diag(x)*invS*ds;

    x=x+alpha*dx;
    s=s+alpha*ds;
    y=y+alpha*dy;

    gamma_n1=(x.'*s)/n;

    if abs(gamma_n1)>10*abs(gamma)
        alpha=5e-2;
    else
        alpha=1;
    end

    cc=cc+1;
    gamma=gamma_n1;

end

x_hat=x;
```

3 AgSim Co-Simulation

```
[VisibleObjects]
UseVisibilityView = 1
SensorName = CH-ObjectSensor
; Camera params for identification view
```

```
Fov = 50.0
AspectRatio = 3.542 ; w/h
VisibilityTextureWidth = 100
NearClipDistance = 1.0
FarClipDistance = 500.0
; Visibility sensor configurations
PixelModeOn = 0
PixelBufferCount = 1
MountingPart = CombineHarvester
MountingOffset = 4.25 0.0 1.576
; (zRot, yRot, xRot) = (heading, pitch, roll) in Mounting part coordinate system
MountingAngles = 0.0 10.0 0.0
ShowSensorPose = 1

Object list:
\begin{verbatim}
% (1)  Object ID
% (2)  Object Group: LC: left corner, RC: right corner
% (3)  Object bounding box LC x coordinate in the visibility view (min x)
% (4)  Object bounding box RC x coordinate in the visibility view (max x)
% (5)  Object bounding box LC y coordinate in the visibility view (min y)
% (6)  Object bounding box RC y coordinate in the visibility view (max y)
% (7)  Object pixel area center of mass x coordinate in the visibility view
% (8)  Object pixel area center of mass y coordinate in the visibility view
% (9)  Number of pixels
% (10)  distance from sensor to target point
% (11)  Heading of object
% (12)  Pitch of object
% (13)  Speed of object
% (14)  Velocity in x-direction
% (15)  Velocity in y-direction
% (16)  Velocity in z-direction
```

Sensor attributes (antenna platform):

```
% (1)  x position in world coordinates
% (2)  y position in world coordinates
% (3)  z position in world coordinates
% (4)  yaw/heading of sensor
% (5)  pitch of sensor
% (6)  roll of sensor
% (7)  number of objects
```